

UNIVERSITY OF CALIFORNIA

Santa Barbara

**Room Temperature Terahertz Detection with Gallium Arsenide Field Effect
Transistors via Plasmon-Assisted Self-Mixing**

A Dissertation submitted in partial satisfaction of the

requirements for the degree of

Doctor of Philosophy

in

Physics

by

Sangwoo Kim

Committee in charge:

Professor Mark S. Sherwin, Chair

Professor Andrew Cleland

Professor Phillip Lubin

Professor Arthur C. Gossard

September 2009

The dissertation of Sangwoo Kim is approved:

Professor Andrew Cleland

Professor Phillip Lubin

Professor Arthur C. Gossard

Professor Mark S. Sherwin, Chair

September 2009

Room Temperature Terahertz Detection with Gallium Arsenide Field Effect
Transistors via Plasmon-Assisted Self-Mixing

Copyright © 2009

by

Sangwoo Kim

“The eternal mystery of the world is its comprehensibility.”

- Albert Einstein -

ACKNOWLEDGEMENTS

First of all, I would like to thank my advisor, Professor Mark S. Sherwin, for his patience and great mentorship. For a long time I thought that doing science would inevitably remove all of good moments with my family. Mark showed me how to balance work and private life – and do each well. And I will follow his example, although it seems to demand super-extraordinary ability. Thanks to my co-workers: Dan Allen for his hyper-activeness, which always brought stimulus, excitement, much fun, and good scientific results; Ben Zaks for his patience and for helping me fabricate last few samples; Dr. Paolo Focardi (Jet Propulsion Laboratory, NASA) for the antenna design; Professor Arthur C. Gossard and his two graduate students, Jeremy Zimmerman and Trevor Buehl (UCSB Materials), for MBE samples with exceptional quality. Thanks to funding agencies which paid my research, living expenses, tuitions and fees: NSF, Dr. Dong Ho Wu (Naval Research Laboratory), and Dr. Ravi Verma (Tanner Research, through Air Force STTR). Thanks to many helping hands from unexpected places: Jaehyuk Shin (Dagli Group, UCSB Materials), whom I met in the cleanroom while he was doing the spray-etch, for transferring spray-etch technique and various cleanroom skills; Vishwanath Venkataraman (now with Apple), my roommate of three years, for helping me better understand the concept of impedance; Professor S. James Allen (UCSB Physics) for HFSS, 140 GHz Gunn oscillator source, and insightful advice on conductivity, dielectric constant, and index of refraction; Professor Elisabeth Gwinn for discussions on 2D and 3D plasmons; Professor Elliot Brown and his student, Adam Young (UCSB ECE), for 600 GHz source; Uttam Singiseti (Rodwell Group, UCSB ECE) for discussions on ultra-high-speed transistor operation; Donghun Shin (UCSB ECE) and Munkyo Seo (Rodwell group) for tutorials and great help with HFSS. Thanks to labmates for discussions and for keep bringing great science into our group meetings: Matt Doty, Kohl Gill, Sam

Carter, Nathan Jukam, Dan Allen, Cristo Yee, Christopher Morris, Ben Zaks, Dr. Brandon Serapiglia, Dr. Dominik Stehr, and Dr. Susumu Takahashi. Thanks to Physics Department's machine shop staff for making precision mechanical parts, essential to much of the research done at UCSB: Mike Deal, Mike Wrocklage, Jeff Dutter, and Doug Rehn. Thanks to cleanroom staff for processing related help and for not kicking me out when I made mistakes: Jack Whaley and Brian Thibeault. Thanks to David Enyeart and Gerry Ramian for operation of the UCSB Free Electron Laser and their humorous jokes. Thanks to the ITST computer and administration staff: Jose, Elizabeth, Marlene, Kate, Rita, and Rob. Thanks to Jeongwoo Lee (at Samsung Electronics Semiconductor R&D Center) and Professor Il-woo Park (formerly at the Korea Basic Science Institute) for supporting my decision to pursue a Ph.D. degree. Thanks to my Korean friends for sharing numerous rides to LA Koreatown: Sungwoo Hong, Hyochul Kim, Byungchae Kim, Ukjin Jung, Hoon Ryu, and Jaehyeong Bahk. Thanks to Harry Potter for the sleepless nights. Thanks to Taejoon Yi, Jaehyuk Shin, and Ben Zaks for proof reading. Thanks to my grandparents and parents who always emphasized the importance of education. I thank them for naming me "Sang"- "woo" which means "each other"- "help," so I can work with many people. Thanks to my two sisters and brother for sharing childhood together. Last, but not least, thanks to my fiancée, Sunhee Lee, for her love and support.

VITA OF SANGWOO KIM

SEPTEMBER 2009

EDUCATION

March 1994 – June 1997, September 1999 – February 2000

Bachelor of Sciences in Physics

Korea University, Seoul, Korea

September 2003 – March 2005

Master of Sciences in Physics

University California, Santa Barbara

March 2005 – September 2009

Doctor of Philosophy in Physics

University of California, Santa Barbara

PROFESSIONAL EMPLOYMENT

Feb 2000 – Nov 2001

Assistant Engineer

Process Development Team, Semiconductor R&D Center, Samsung Electronics,
Kiheung, Korea

Sep 2002 – Aug 2003

Research Scientist

Structure Analysis Team, Korea Basic Science Institute, Seoul, Korea

September 2003 – March 2004

Teaching Assistant

Department of Physics, University of California, Santa Barbara

March 2004 – June 2009

Graduate Student Researcher

Terahertz Dynamics and Quantum Information in Semiconductors Lab.,
Department of Physics and Institute for Terahertz Science and Technology,
University of California, Santa Barbara

OTHER OCCUPATIONS

June 1997 – August 1999

Sergeant,

Korean Augmentation Troops to the United States Army (KATUSA)

1/15 Field Artillery, 2nd infantry Division, US Army, Camp Casey, Korea

PUBLICATIONS

Sangwoo Kim, Jeramy D. Zimmerman, Paolo Focardi, Arthur C. Gossard, Dong Ho Wu, and Mark S. Sherwin, "*Room temperature terahertz detection based on bulk plasmons in antenna-coupled GaAs field effect transistors*", *Applied Physics Letters* **92**, 253508 (2008)

D. G. Allen, Sangwoo Kim, C. R. Stanley, and M. S. Sherwin, "*High fidelity optical readout of excited-state lifetimes and ionization of hydrogenic donors in GaAs*", *Applied Physics Letters* **93**, 181903 (2008)

D. G. Allen, Sangwoo Kim, C. R. Stanley, and M. S. Sherwin, "*Rydberg atom physics in the solid state: resonance fluorescence detection of interactions in terahertz-excited hydrogenic impurity ensembles*", manuscript in preparation

PATENT

UC Provisional Patent, Case No. 2008-723 - FASTER RESPONSE, ROOM TEMPERATURE TERAHERTZ DETECTORS

CONFERENCE PRESENTATIONS

American Physical Society (APS) March meeting, Denver, CO (talk, 2007)

American Physical Society (APS) March meeting, New Orleans, LA (talk, 2008)

Conference on Lasers and Electro-Optics (CLEO), San Jose, CA (talk, 2008)

33rd International Conference on Infrared, Millimeter, and Terahertz Waves (IRMMW-THz), Caltech, Pasadena, CA (talk, 2008)

International Workshop on Optical Terahertz Science and Technology (OTST), Santa Barbara, CA (talk, 2009)

Materials Research Society (MRS) Spring meeting, San Francisco, CA (talk, 2009)

HONORS

Korea LIONS Club Scholarships, Fall 1995 to Fall 1999

Korea University Honors Scholarships, Spring 1994 and Fall 1994

ABSTRACT

Room Temperature Terahertz Detection with Gallium Arsenide Field Effect Transistors via Plasmon-Assisted Self-Mixing

by

Sangwoo Kim

Previously, members of the Sherwin Group made a sensitive narrowband, tunable terahertz (THz) detector based on intersubband transitions of quantum wells. However, due to the nature of its excitation mechanism, it required costly liquid nitrogen cooling. With a device structure similar to that of the previous detector, but by introducing bulk electron plasmon as an absorber, a sensitive broadband, room temperature terahertz detector is realized. In this work, the plasmons in GaAs metal-semiconductor-field-effect-transistors (MESFETs) have been electrically tuned and detected for frequencies of 0.14, 0.24, 0.6 and 1 THz. The first generation of these detectors exhibits sensitivity and speed characteristics better than those of commercial pyroelectric detectors (measured responsivity of 80 $\mu\text{A/W}$, a NEP of about 50 $\text{nW/Hz}^{1/2}$, and speed < 10 ns). Although the detector works well, numerous unexpected behaviors were observed, such as strong photovoltaic response and dual resonances. These observations are explained with the assumption of two space-charge regions where plasmons are locally excited and a terahertz self-rectification process occurs. The new analytical model of “plasmon-

assisted self-mixing” can explain the experimental observations both qualitatively and quantitatively. Also, the model suggests three important factors for improving the detector sensitivity: power coupling efficiency, self-mixing efficiency, and the plasma resonance. If carefully optimized, the performance of this new detection scheme could rival that of the commercial state-of-the-art Schottky diode detectors. The new detection scheme also conceptually permits scaling to higher frequencies without the significant loss of sensitivity exhibited by Schottky diodes. Therefore, it would be interesting to navigate the possibility of terahertz to mid-infrared (MIR) operation or waveguide coupling where the technology could be integrated with various quantum cascade lasers (QCLs). Successful detectors may be employed to characterize THz-QCLs, or could become compact receiver parts for a terahertz communication system or pixels for a focal plane array terahertz imager.

TABLE OF CONTENTS

Chapter 1 Introduction	1
1.1 What Is Terahertz (THz) and Why Is It Interesting?.....	1
1.2 Lack of Sensitive, Affordable, and Fast Room Temperature THz Detector	3
1.3 Concept of Optical Photon Detection	4
1.4 Concept of Electronic THz Rectification (Schottky Detectors).....	5
1.5 Other Detector Technologies	7
1.6 Two Detection Modes of This Work: Photoconductive and Photovoltaic	8
1.6.1 Non-Saturating Plasmon and Channel Center Approximation	9
1.6.2 Separation of Readout and Coupling Channels	16
1.6.3 High-efficiency, Tunable THz Antenna System	17
1.7 Impact of This Work	19
Chapter 2 Photoconductive Detection Mode	20
2.1 Overview	20
2.2 Physical Properties and Symbols	25
2.3 Coupling Channel Impedance of GaAs FET, Z_{FET}	29
2.4 Power Coupling Efficiency, α	33
2.5 Heat Dissipation for Robustness and High Dynamic Range.....	36
2.6 Readout Channel	40
2.6.1 Electron Mobility, $\mu(T)$	41
2.6.2 Electron Number Density, $n(T)$	43
2.6.3 Read-Out Resistance, $R(T)$	44
2.6.4 Rate of Change of the Readout Resistance, γ	45
2.6.5 Experimental Verification of γ	46
2.7 Responsivity, \mathcal{R} , and Noise Equivalent Power, NEP.....	48
2.8 Design Tool Software	50
Chapter 3 Samples	52
3.1 MBE Grown Wafers	52

3.2 Cleanroom Processing Overview	53
3.3 Silicon Lens Mount	55
Chapter 4 Experiment	58
4.1 Detector Measurement Setup	58
4.2 Weak Response with X-polarization.....	61
4.3 High Power Measurement.....	63
4.4 Strong Photovoltaic Response with Y-Polarization.....	64
4.5 Measured Figures of Merit with Y-Polarization	67
Chapter 5 Photovoltaic Detection Mode	73
5.1 Theory of Plasmon-Assisted Self-Mixing.....	74
5.1.1 Enhanced E-fields due to the Metal-Insulator-Metal (MIM) Structure	74
5.1.2 Qualitative, Simplified Model.....	78
5.1.3 Experimental Data Support the Qualitative Model.....	83
5.1.4 Frequency Dependence of the Plasma Resonance	86
5.1.5 Analytic, Simplified Model.....	89
5.1.6 Model without the Channel Center Approximation.....	97
5.1.7 Circuit Simulation (Off-Resonant Self-Mixing)	101
5.2 Noise, SNR, and NEP	108
5.3 Low Temperature Measurements.....	114
5.4 Suggestions for Improvement	116
Chapter 6 Conclusions.....	119
Appendix A Cleanroom Processings	121
A.a Overall Processing Steps	121
A.b Processing Steps Details.....	122
A.c Processing Tips.....	129
A.c.1 Dehydration Bake	129
A.c.2 Step 0: Alignment Marks Photo	129
A.c.3 GCA6300.....	129
A.c.4 Surface Treatment with NH ₄ OH:DI = 1:10 Solution.....	130
A.c.5 LOL 2000 and CEM	130
A.c.6 E-beam #4 vs. E-beam #3.....	130

A.c.7 Making Ohmic Contacts to N-type GaAs.....	131
A.c.8 EPO-TEK 353ND (G-1) Epoxy	131
A.c.9 Spray Etch.....	131
A.c.10 DI Rinse Cleaning	132
A.c.11 Solvent Cleaning	133
A.c.12 Ultrasonic Cleaning	133
A.d Processing Cartoons	134
Appendix B Imaginary Number: i or j ?.....	139
Appendix C Impedance Matching.....	145
Appendix D Mathematica Code.....	148
Appendix E 1D-Poisson Code	150
Appendix F Matlab Code	151
Appendix G HFSS.....	157
G.a Example: 240 GHz EPR Cavity	158

Chapter 1 Introduction

1.1 What Is Terahertz (THz) and Why Is It Interesting?

The terahertz (THz) frequency band refers to electromagnetic radiation of frequency $0.1 \sim 10 \times 10^{12}$ Hertz. In the electromagnetic spectrum, the terahertz band is located between microwave and infrared (see Fig. 1.1) [1].



Figure 1.1 Electromagnetic Spectrum. Figure obtained from SURA, Ref. [1].

Thanks to various unique properties, terahertz radiation enables applications that other types of electromagnetic radiation cannot. For example, terahertz radiation can penetrate many commonly used materials to identify hidden explosives by time-domain spectroscopy [2] or to identify the physical shape of weapons by 2D imaging [3]. Terahertz radiation can detect corrosion under the

insulating tiles of NASA's space shuttles [4]. It is believed that our universe has been cooling down since the Big Bang. Due to the cooling, the cosmic microwave background (CMB) radiation from the early universe is now abundant in the terahertz band and is being measured in order to study the structure of the early universe. The Plank Satellite launched in May 2009 by European Space Agency will image the sky at six frequencies between 0.1 THz and 0.857 THz [5]. Terahertz radiation is sensitive to vibrational- and rotational-modes of biological molecules, such as water, methane [6], and proteins [7, 8]. Therefore, terahertz radiation can be employed for studying planetary atmospheres, interstellar materials [9], biological processes [10, 11], or for serving particular medical reasons [12].¹ Since the photon energy of terahertz radiation is low (1 THz photon energy = 4 meV), terahertz applications are non-destructive and probably safe for human body (In comparison, X-ray photon energy = $10^2 \sim 10^5$ eV). There also have been reports of using terahertz technique in pharmaceutical industry [13] and paper-producing industry [14]. As of June 2009, commercial central processor units (CPUs) by Intel have clock speed as fast as 3.33 GHz [15]. CPUs operating in terahertz frequencies will enable several orders of magnitude faster information processing than the current state-of-the-art [16]. Overall, terahertz electromagnetic radiation provides

¹ For example, cancerous cells have more water contents than normal cells. THz technique could provide a quantitative method for determining any suspected cells to be cancerous or normal.

numerous unique opportunities in military, security, space, Earth and planetary sciences, biology, medical, manufacturing industries, and information technology. There should be even more applications yet to be discovered. It is in this context that the development of affordable, compact, yet sensitive and fast enough terahertz detector is essential.

1.2 Lack of Sensitive, Affordable, and Fast Room Temperature THz Detector

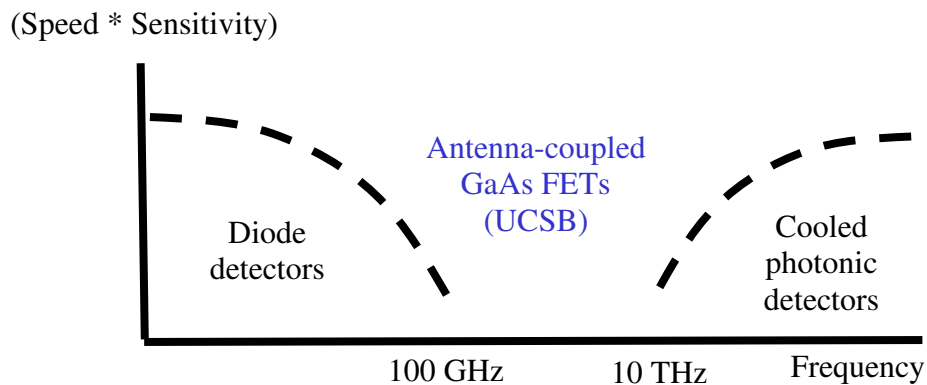


Figure 1.2 “Terahertz gap” diagram for terahertz detector technology. Detector performance (= speed times sensitivity) is drawn schematically vs. frequency. Achieving both high speed and high sensitivity is difficult. UCSB antenna-coupled GaAs FETs were developed in order to fill this technological gap.

Although terahertz technology has great implications for many, the lack of affordable, sensitive, and fast room temperature detectors for the terahertz band hinders the development of terahertz applications. For terahertz detection

technology at room temperature, there exists a trade-off between the speed and sensitivity, creating the so called “terahertz gap” (see Fig. 1.2). There are two main approaches to make terahertz sensors: optical photon detection and electronic rectification.

1.3 Concept of Optical Photon Detection

Detectors based on the concept of optical photon detection approach the terahertz band from higher frequencies. Quantum transitions that are resonant with terahertz photons can induce detectable changes in the system (see Fig. 1.3), and therefore can be used for terahertz photon detection. The terahertz antenna-coupled intersubband terahertz (TACIT) detector [17-19] and terahertz quantum well infrared photodetector (QWIP) [20] employ such a concept.

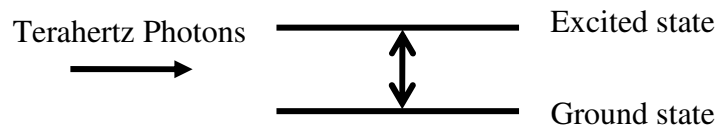


Figure 1.3 Quantum two-level system that is resonant with terahertz photons. Energy difference between the ground and excited states should be 4.14 meV for resonance with 1 THz photons.

The limitation of this approach originates from the ample amount of blackbody radiation at terahertz band from any objects sitting at room temperature [21].² This background radiation causes saturation of any quantum two-level transitions. Due to this limitation, optical photon detection schemes require expensive cryogenic cooling. For an example, the TACIT detector works only up to 100 K [19].

1.4 Concept of Electronic THz Rectification (Schottky Detectors)

Detectors based on the concept of electronic rectification approach the terahertz band from lower frequencies, usually by making use of the nonlinear IV characteristic of a Schottky junction. Normally, the electronic circuit has to be made small, with short junction distance, in order to be able to respond to the rapid terahertz oscillations. However, such design strategy tends to increase unwanted capacitances (of the junction and the parasitic) and degrade the sensitivity (see Fig. 1.4). This is the RC time constant problem of electronic circuits at high frequency.

² Blackbody radiation of 290 K peaks at 17.1 THz (17.6 μm). For the exact quantitative form of the radiation fluence, see p.105 of the reference.

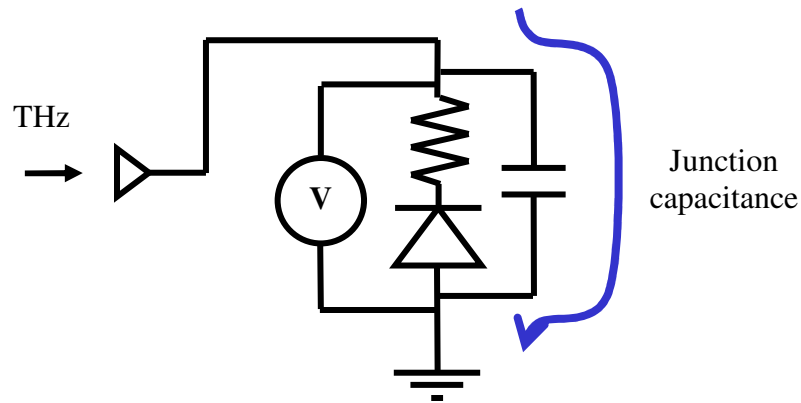


Figure 1.4 Schematic diagram of Schottky diodes. Junction capacitance shorts out the readout channel (RC time constant problem).

In spite of the limitation, there have been successful efforts that push the technology to the limit by careful engineering. As far as room-temperature terahertz detection is concerned, Schottky diode technology has been the most successful one. Zero-bias Schottky diode detectors by Virginia Diodes (see Fig. 1.5 for a SEM image) nowadays have a voltage sensitivity of around 100 V/W for up to 2 THz, and a *NEP* as low as $20 \text{ pW/Hz}^{1/2}$ at 0.8 THz [22]. This is an extremely mature technology, integrating $\sim 100 \text{ nm}$ size Schottky diodes with precision-machined solid metallic waveguides. The performance of the 2nd generation device of this work would have to improve by factors of about 100 \sim 1000, if it wants to directly compete with Schottky diodes (current 1st generation device exhibits measured responsivity of $80 \text{ }\mu\text{A/W}$, a *NEP* of about $50 \text{ nW/Hz}^{1/2}$, and speed $< 10 \text{ ns}$).

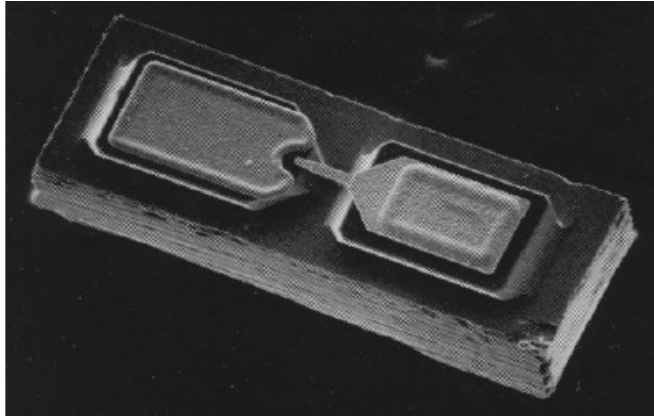


Figure 1.5 SEM image of a VDI Schottky diode from Ref. [22]. Chip dimensions are approximately $180 \times 80 \times 40 \mu\text{m}$. The detection frequency of the device shown in this photograph is undisclosed.

1.5 Other Detector Technologies

Field-effect-transistors (FETs) have been known to have some response to terahertz radiation. While there have been one or two suggestions for the detection mechanism, these claims were not so clear. Tauk *et al.* reported NEP of $\geq 10^{-10} \text{ W/Hz}^{1/2}$ with silicon FETs at 0.7 THz, and suggested the theory of two-dimensional (2D) plasma waves for the detection mechanism [23]. U.R. Pfeiffer *et al.* also reported similar figures, about $4 \times 10^{-10} \text{ W/Hz}^{1/2}$ with silicon FETs at 0.6 THz, and suggested self-mixing of terahertz radiation with off-resonant 2D plasma waves (i.e., the theory of 2D plasma wave detection at off-resonant regime) for the detection mechanism [24-26]. Hartmut Roskos reported slightly worse NEP of about $3 \times 10^{-8} \text{ W/Hz}^{1/2}$ with GaAs FETs at 0.6 THz [27]. For examples of the

terahertz detector technologies other than FETs, the golay cell typically has a *NEP* of 1.2×10^{-10} W/Hz^{1/2} and a chopping frequency of 15 Hz. The pyroelectric detector has a *NEP* of 4.0×10^{-10} W/Hz^{1/2} and an optimum chopping frequency of 5 to 10 Hz [28]. Photon drag detectors are fast, but not as sensitive [29]. By comparison, this work reports a *NEP* of about 5×10^{-8} W/Hz^{1/2} with GaAs FETs at 1 THz [30], and suggests on-resonance three-dimensional (3D) electron plasmon-assisted terahertz self-mixing for the detection mechanism.

1.6 Two Detection Modes of This Work:

Photoconductive and Photovoltaic

Detectors in this work were originally designed to operate in a *photoconductive* mode. The theory of the proposed concept is based on the previous works by Mark Sherwin *et al.* on TACIT detector [17], and Boris Karasik *et al.* on bolometers [31]. Upon absorption of terahertz photons, the conductivity of the readout channel is altered. The bulk electron plasmon is employed, in order to avoid the saturation problem which was discussed in Section 1.3. The readout and coupling channels are separated, in order to avoid the time constant problem in Section 1.4. As will be discussed later, the proposed *photoconductive* detection scheme did not work, and consequently led to the discovery of another new detection model (*photovoltaic*

detection scheme). Both the proposed and the newly found detection model will be discussed in Chapters 1 ~ 2 and 4 ~ 5, respectively.

1.6.1 Non-Saturating Plasmon and Channel Center

Approximation

The device structure of this work is similar to the structure of the TACIT detector. By replacing the quantum transitions of the TACIT detectors (i.e., the intersubband transitions of the double quantum wells) with classical harmonic oscillators (i.e., bulk electron plasmons in n-type doped GaAs), a room-temperature terahertz detector can be realized. The plasmon is the quantum of collective excitations of “free” electrons in the conduction band of a solid. Ideally, if the confinement of the electrons is of a parabolic potential well, the well provides equally spaced energy levels. Therefore, the excitation mechanism (i.e., the plasmon) is non-saturating (see Fig. 1.6).

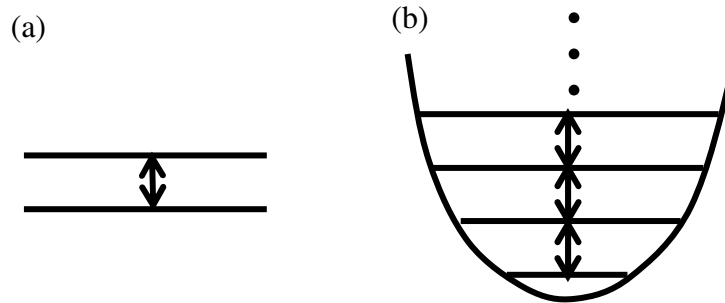


Figure 1.6 Energy level diagrams of (a) a quantum two-level system which saturates, (b) ideal parabolic potential well which does not saturate with thermal background blackbody radiations from objects at room temperature.

In fact, the physics of electrons in a parabolic potential well is quite complex and is explained with the generalized Kohn theorem [32-38]. In a uniformly doped n-type semiconductor, positively charged donor ions provide ideal parabolic (or “bare harmonic”) potential wells in all (x , y and z) direction. Let’s consider, for example, z -direction terahertz E-field coupling. If all donors are ionized, and all electrons are depleted, the remaining potential is the bare harmonic confining potential $V_C(z)$ originating from the background ionized donors. With only one electron in this potential (e.g., with an almost depleting negative gate voltage), the electron can absorb terahertz photons resonating with the intersubband transition energy of the well. The frequency of this transition is given by the curvature of $V_C(z)$:

$$\omega_0 = \sqrt{\frac{8\Delta_1}{W^2 m^*}} = \sqrt{\frac{n_+ e^2}{m^* \epsilon}} \quad (1.6.1.1)$$

, where Δ_1 , W , m^* , e , n_+ , and ϵ are respectively the depth, width of the bare harmonic oscillator potential, the effective mass, the electric charge of electrons, the background ionized donor density, and the permittivity of GaAs.

As more electrons are added to the potential well, electrons repel each other and distribute themselves in order to minimize the total internal energy. The resulting electron distribution (see Fig. 1.7) and the modified potential (see, for example, Fig. 1 of Ref. [35]) can be obtained from a self-consistent Poisson

simulation. In other words, one has to calculate self-consistent eigenvalues and eigenfunctions of the Hamiltonian [38]:

$$H = \frac{P^2}{2m^*} + V_C(z) + V_H(z) + V_{XC}(z) \quad (1.6.1.2)$$

, where P , m^* , V_C , V_H , and V_{XC} are respectively the electron momentum, effective mass, bare harmonic potential, Hartree potential, and local exchange-correlation potential.

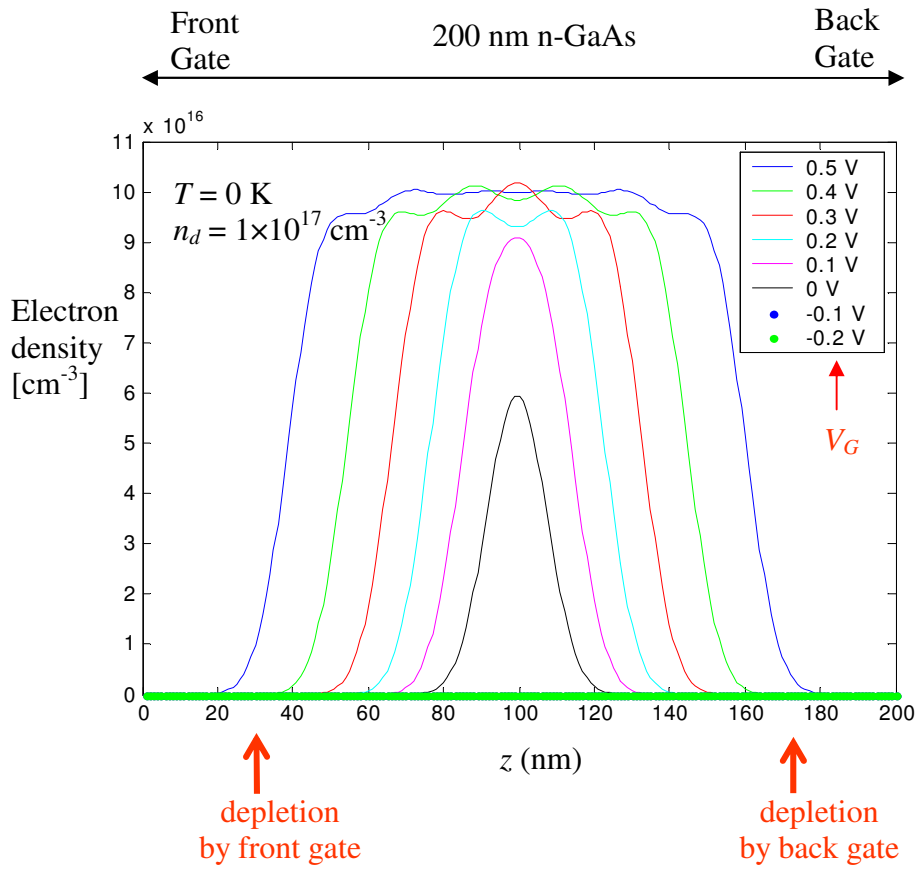


Figure 1.7 Electron distributions from self-consistent 1DPoisson calculations with different well filling conditions with different gate bias voltages (V_G). Simulation temperature $T = 0$ K, n-type dopant density $n_d = 10^{17} \text{ cm}^{-3}$, background ionized donor density $n_+ = 10^{17} \text{ cm}^{-3}$, donors were forced to ionize 100 %.

The resulting electron distribution is a sheet of uniform electron gas with a density n_{3D} and a thickness t ($< W$) at the center of the well. The uniform negative charge of the electron gas exactly cancels out the background positive charge of the ionized donors ($n_{3D} = n_+$) over the region where the electrons are sitting. Therefore, the resulting self-consistent potential has a flat bottom over t at the center and harmonic potential walls for the remaining parts. This has effects of widening the width of the well (W) and therefore shrinking the intersubband transition energy in eq. (1.6.1.1). The modified intersubband transition is then shifted by a strong depolarization effect [34, 36, 38] and eventually approaches the 3D limit [34]. In the 3D limit, the absorption frequency is given by the bulk plasmon frequency:

$$\omega_p = \sqrt{\frac{n_{3D} e^2}{m^* \epsilon}} \quad (1.6.1.3)$$

, where n_{3D} , e , and m^* are respectively the 3D number density, charge, and effective mass of electrons in GaAs [39].

In a sufficiently wide ideal parabolic potential well, n_{3D} equals n_+ , so ω_p coincides with ω_0 “by construction” [35]. Note that a uniform terahertz E-field excites oscillation of the center of mass of the electron gas, or the “sloshing” motion of the electron gas [40]. In this case (coupling mode of Chapter 2), the excitation frequency is the bare harmonic potential frequency ω_0 and is independent of the electron-electron interaction (independent of n_{3D}).

However, if terahertz E-field is not uniform, or electrons are not uniformly distributed, collective modes involving internal compression can be excited [40]. In

such cases (coupling mode of Chapters 4 ~ 5), electron-electron interaction becomes responsible for the resonant oscillations and ω_p becomes the relevant absorption frequency.

As shown in Fig. 1.7, symmetric bias voltages to the both ends of the well would change the thickness (t) of the electron gas, but would not change the density (n_{3D}) of the electron gas. Asymmetric bias would only shift the position of the sheet of the electron gas in the direction of the bias voltages.

In contrast, the electron density in this work is tunable with a wide range of gate bias voltages as shown in Fig. 1.8.

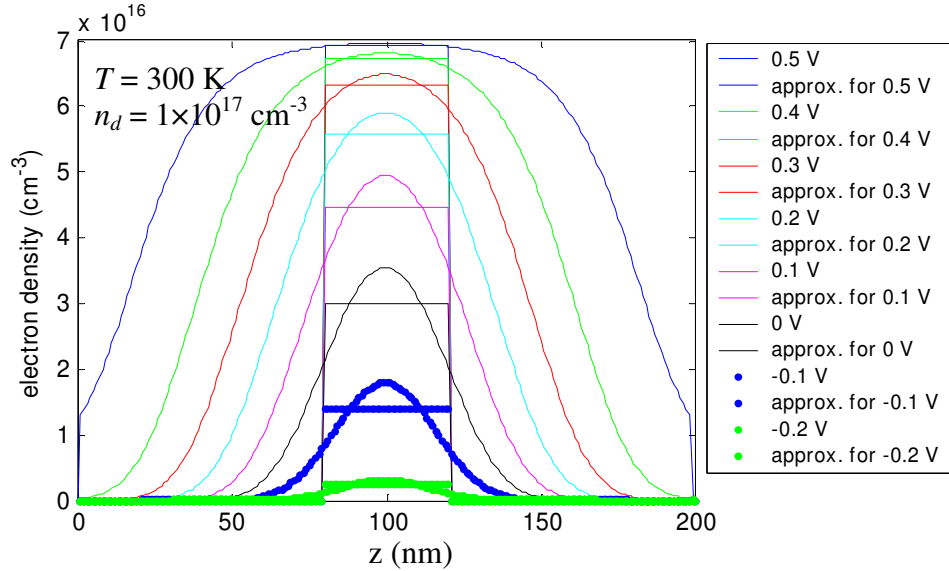


Figure 1.8 The Electron density is tunable with a bias voltage across the gate (V_G). Channel center approximation is taking the average over the 40 nm ($= \delta$) region. Simulation temperature $T = 300$ K, n-type dopant density $n_d = 10^{17}$ cm $^{-3}$, and donors were *not forced to ionize*. The saturated value of the electron density suggests the background ionized donor density $n_+ = 7 \times 10^{16}$ cm $^{-3}$.

The ability to tune the electron density turns out to be essential for identifying the detection mechanism as the “plasmon-assisted self-mixing” in Chapters 4 ~ 5.

Terahertz detectors in this work were designed for 1 THz radiation. According to eq. (1.6.1.3), a resonance at 1 THz can be obtained with electron plasma of a density $\sim 10^{16} \text{ cm}^{-3}$. Since the thickness of the n-type doped layer is only 200 nm ($= d$), the depletions from the two gates overlap with each other, and results in a low electron density of $1 \times 10^{16} \text{ cm}^{-3}$ with a nominal dopant density of $8 \times 10^{16} \text{ cm}^{-3}$. Depletion length is about 140 nm with a Schottky barrier height of 1.25 eV and a dopant density of $8 \times 10^{16} \text{ cm}^{-3}$ [41].

The electron densities in Fig. 1.8 are not constant over the entire cross-section. However, the plasmons have a short lifetime of about 0.36 ps ($= \tau_e$) at room-temperature due to the polar optical phonon scattering processes [42], and hence has a broad absorption bandwidth (~ 0.5 THz). Therefore, the electron density can be safely approximated to a constant density over a reasonable area. In this work, constant electron density over $\delta = 40$ nm along the MBE growth direction at the channel center is assumed (the channel center approximation). Fig. 1.8 shows the approximated electron densities and Fig. 1.9 (a) shows the plot of the approximated electron density vs. the gate bias voltages (V_G). Fig. 1.9 (b) shows corresponding plasmon frequencies vs. V_G . The proposed model in Chapters 1 ~ 2 and the simplified analytical model in Section 5.1.5 use this channel center approximation. A one-dimensional quantitative model without the channel center approximation in

Section 5.1.6 uses the full one-dimensional Poisson data, and provides both qualitative and quantitative explanations of the experimental observations.

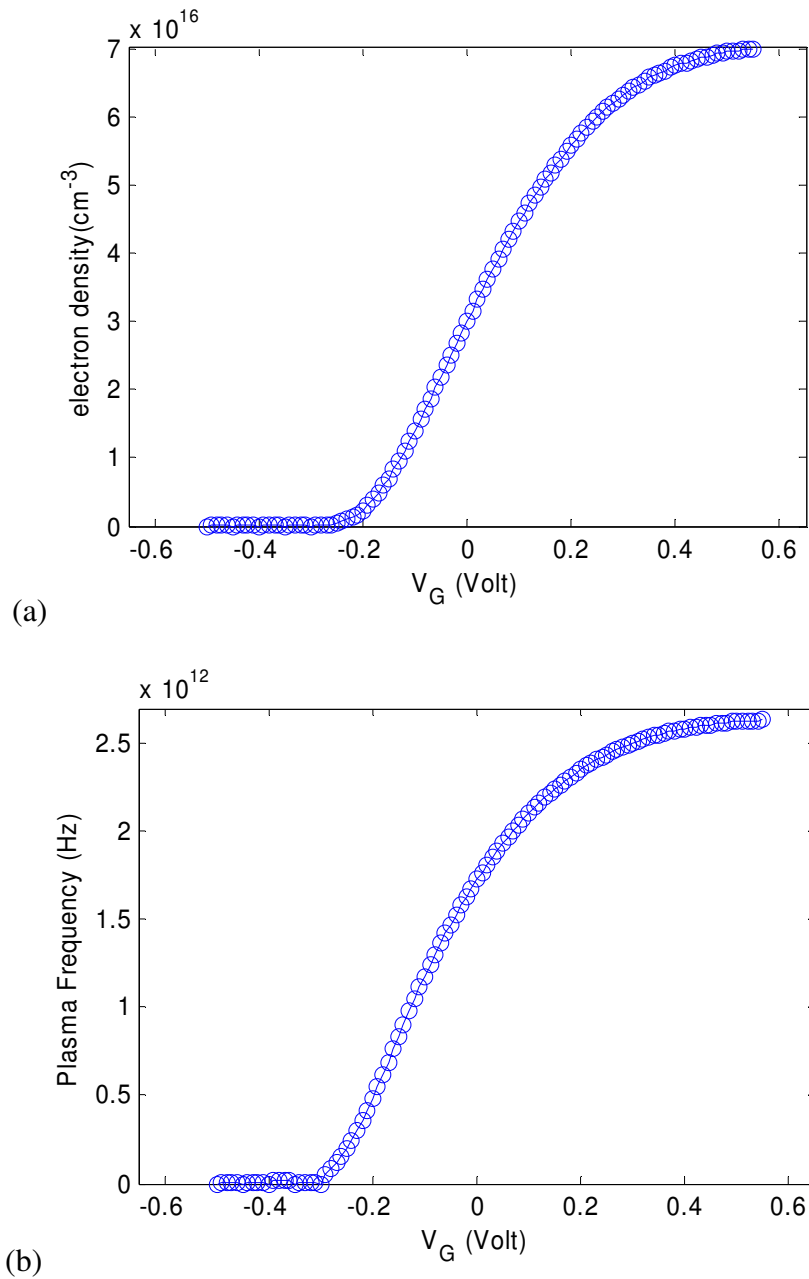


Figure 1.9 (a) The average electron density vs. V_G . (b) The corresponding plasma frequency with the channel center approximation vs. V_G , using eq. (1.6.1.3).

1.6.2 Separation of Readout and Coupling Channels

As discussed earlier in Section 1.4, the limitation of Schottky diodes originates from the junction capacitance which shorts out the readout channel and the fact that they utilize the same channel for the coupling and readout of the terahertz radiation. Therefore, optimizing the performance of one channel degrades the performance of the other channel, and vice versa. In contrast, the four-terminal design of this work separates the coupling and readout channels (see Fig. 1.10 for a schematic diagram). Therefore, the coupling efficiency and the readout efficiency can be optimized without adversely affecting each other.

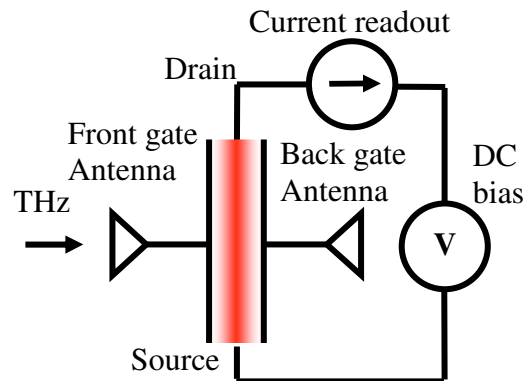


Figure 1.10 Schematic diagram of four-terminal UCSB terahertz detectors. Coupling channel (front gate - back gate) is separated from the readout channel (source - drain).

1.6.3 High-efficiency, Tunable THz Antenna System

The high-efficiency terahertz antenna system with tunable input impedance was provided by Dr. Paolo Focardi in NASA JPL [43]. See Fig. 1.11 (a) and (b) for the antenna design of the superconducting hot electron bolometers.

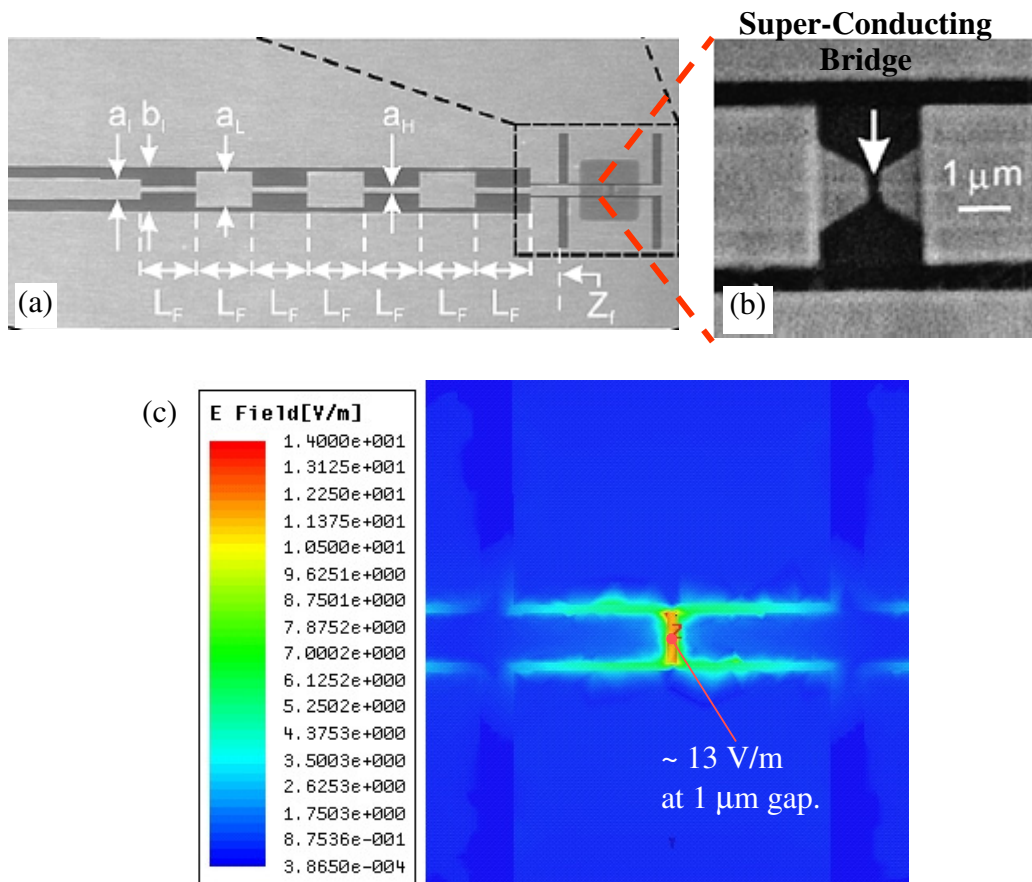


Figure 1.11 (a), (b) Terahertz antenna for superconducting hot electron bolometers. Picture taken from Paolo Focardi *et al.*, Ref. [43], (c) Electric field is enhanced by a factor of 13, according to the finite element method 3D electromagnetic simulation. A Gaussian input beam with $E_0 = 1 \text{ V/m}$, beam waist radius = $50 \mu\text{m}$ (incident cone half angle = 30° implied) was used.

As shown in Fig. 1.11 (c), the electric field is enhanced by the antenna system by a factor of 13, according to the finite element method 3D electromagnetic simulation of the structure. A commercial software HFSS by Ansoft Corp. has been used for the simulation. The design of this antenna system was modified in order to feed the absorbed terahertz radiation into the two gates of a GaAs field-effect-transistor.³ Due to the large gate area, the impedance of the GaAs FET (Z_{FET}) is remarkably small, on the order of 10Ω . This small impedance can be matched very well to the input impedance of the planar slot dipolar antenna system (Z_{ANT}). Z_{ANT} is tunable to a limited degree by adjusting dimensions of the coplanar waveguides (CPWs) and transmission lines.

By iteratively modifying the dimensions (i.e., gate length, width, thickness, CPWs, and transmission lines), the overall coupling efficiency (α) was optimized up to 27 % (calculated), which is remarkably high for free-space terahertz coupling. The coupling efficiency could be further improved if parylene anti-reflection coating is applied on the silicon lens (Professor E. R. Brown's Lab. has this capability.). A scanning electron microscopy image of the resulting detector can be seen in Fig. 1.12. Unfortunately, there was a mistake in the calculation of the

³ What was overlooked at this modification stage was the Y-polarization. The antenna system is designed to be used with X-polarization only. However in this work, by modifying the structure, and by making use of non-directional absorption mechanism (plasmon), the detector unexpectedly couples with Y-polarization. This will be discussed later in chapter 4 ~ 5.

impedance of the GaAs FET at the beginning stage of this work. After correction, the coupling efficiency is estimated to be about 10 % (calculated). The correction is discussed in Section 2.2 in more detail.

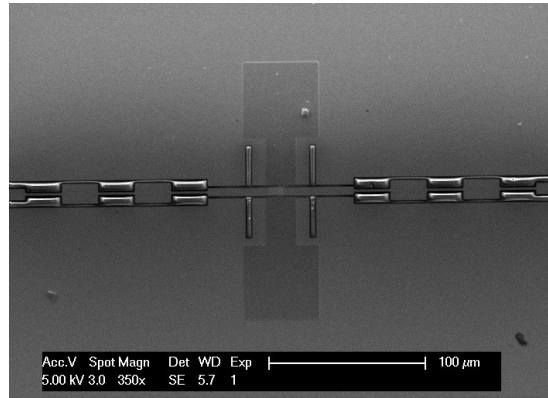


Figure 1.12 Scanning electron microscopy image of a UCSB terahertz detector. The size of the minimum feature is 1 μm .

1.7 Impact of This Work

This work fills the “terahertz technological gap” with the new concept of plasmon detection and also contributes to the understanding of the electron plasma at high frequencies in solid-state systems. Successful detectors may be employed to characterize various terahertz sources such as THz – quantum cascade lasers (QCLs) and free electron lasers (FELs). They could also become affordable, compact receiver parts for a terahertz imaging or communication system. It would also be interesting to navigate the possibility of mid-infrared (MIR) operation or waveguide coupling where the technology may be integrated with various QCLs.

Chapter 2 Photoconductive Detection Mode

As mentioned earlier in Section 1.6, our 1st generation detectors did not follow the prediction of the proposed *photoconductive* detection model. Instead, they led us to the discovery of another new detection model. In this chapter, the details of the proposed detection scheme are described. The other, the newly discovered detection model, will be discussed in Chapters 4 - 5. As it will become clear later, the proposed model could also become a detection principle for the next generation devices whose oscillator strength shall be in the MBE growth direction only. Readers who are not interested in a model that does not apply to devices discussed in this thesis may jump to Chapter 3 or 4 to learn about the newly discovered model that works.

2.1 Overview

The proposed detection scheme follows this flow: Absorbing terahertz radiation with twin-slot dipolar antennas → transferring the energy into the “sloshing” motion of the electrons in the active area of the transistor → resonantly exciting 3D

(bulk) electron plasmons at bare harmonic potential frequency $\omega_0 \rightarrow$ measuring the change of the source-to-drain resistance (R_{SD}). The antenna was designed to receive X-polarized (X-pol.) terahertz radiation. See Fig. 2.1 and Fig. 2.2 for the layout of the detector and polarization directions.

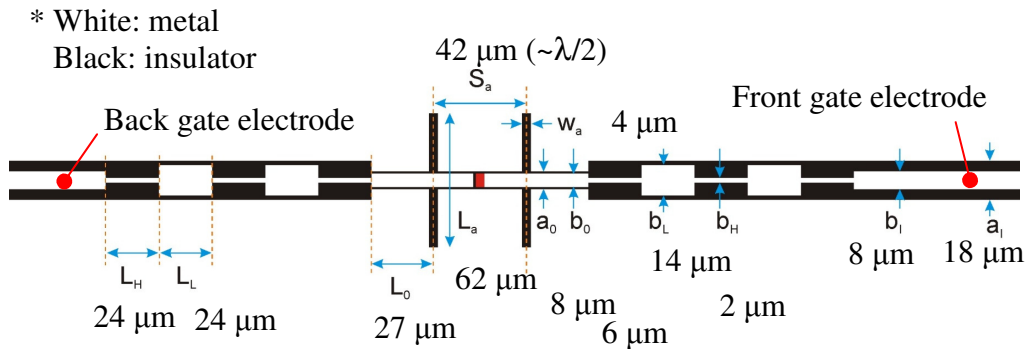
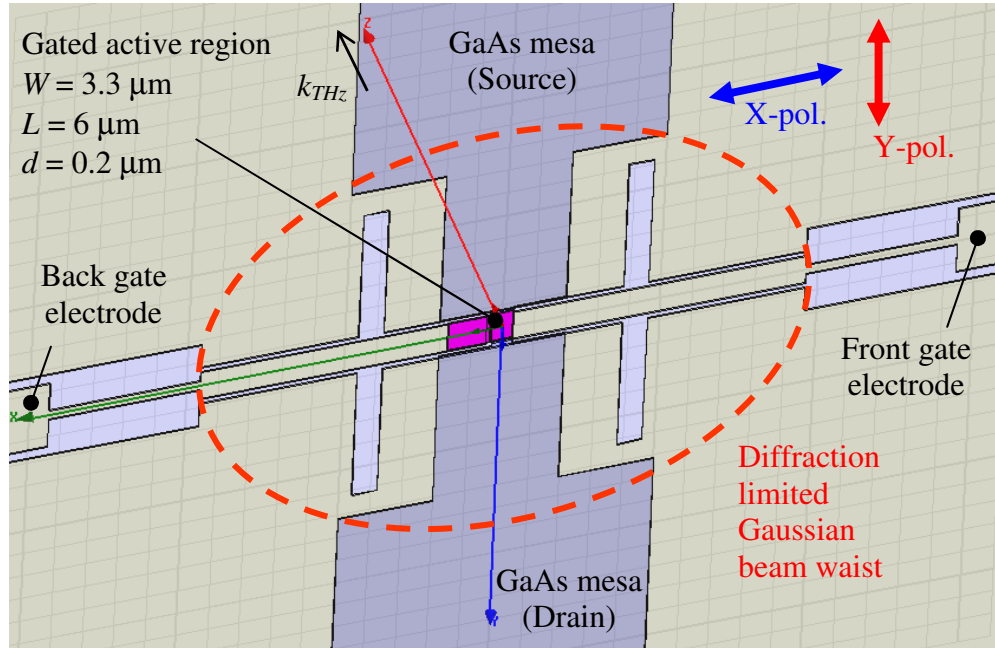


Figure 2.1 Layout of the device showing dual slot dipolar antennas, coplanar waveguides (CPWs), transmission lines, GaAs mesa, and gates. Electric fields of the X-polarized and Y-polarized terahertz radiation are indicated as blue and red arrows, respectively. k_{THz} and a black arrow denote the propagation vector of the incident terahertz Gaussian beam. Layout from Paolo Focardi, JPL, NASA.

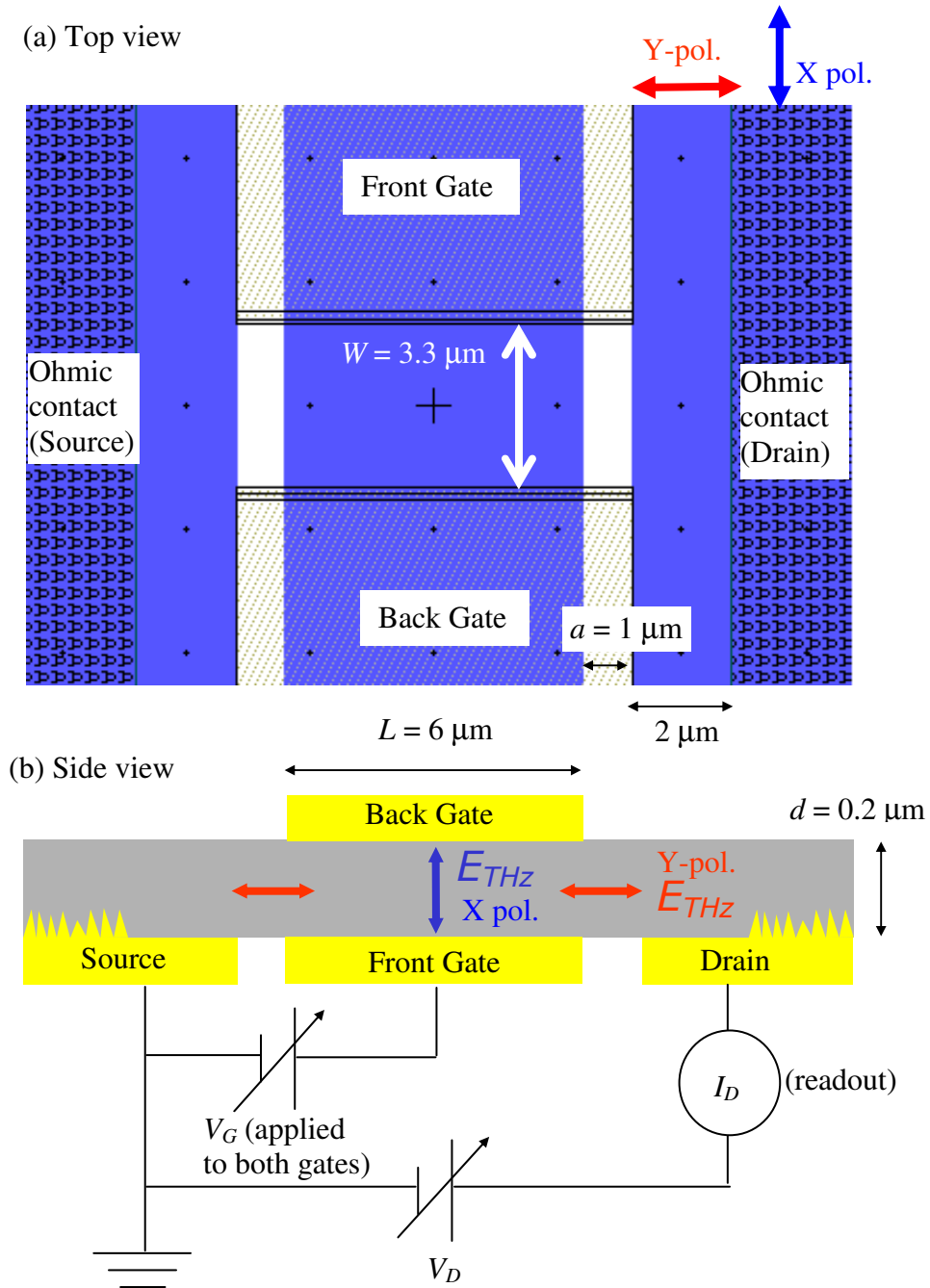


Figure 2.2 (a) Top view and (b) side view of the transistor part of the detector. Dimensions are drawn to scale, except for the vertical dimension of (b).

Since this detection mode reads the change of R_{SD} , it requires a DC, source-to-drain bias voltage (V_D) to be applied for readout. This bolometer-like detection mode should generate a photoconductive current signal with a square-law responsivity (signal is proportional to the power of incident terahertz radiation).

Theoretical estimation of the figures of merits (e.g., responsivity, noise equivalent power) follows the very flow of the detection scheme, and is based on the previous works by Mark Sherwin *et al.* on TACIT detector [17], and Boris Karasik *et al.* on bolometers [31]. First, the impedance of the GaAs field-effect-transistor (FET) is calculated. Then the overall power coupling efficiency is obtained from electromagnetic simulations by Dr. Paolo Focardi. Next, with the known incident power absorbed by the electron gas from the previous step, the rate of change of resistance is calculated. Finally, responsivity (in Amperes/Watt or in Volts/Watt) and NEP (in Watt/Hz^{1/2}) is calculated following the bolometer theory of Boris Karasik *et al.* [31].

Fig. 2.3 shows the distribution of the electric field magnitudes obtained from HFSS simulations for the X-polarized (X-pol.) and Y-polarized (Y-pol.) terahertz radiation. The proposed detection scheme in this chapter considers X-pol. (Fig. 2.3 (a)) only. The unexpected detection mode with Y-pol. (Fig. 2.3 (b)) will be discussed in Chapter 4.

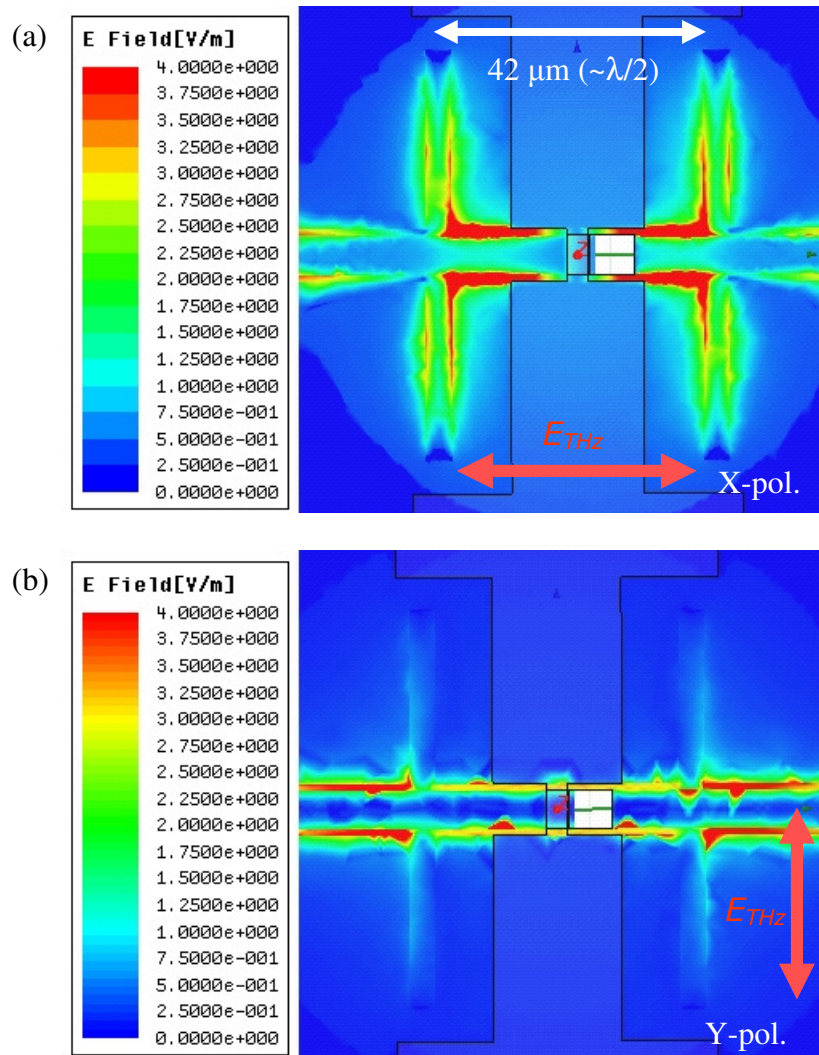


Figure 2.3 (a) HFSS simulation results with X-polarization (X-pol.). The field enhancement is not as great as in Fig. 1.10 (c), mainly due to the increased area of the excitation area. This may be a part of the reasons for the small responsivity to X-pol. in Chapter 4. See Section 4.2 for more discussions. (b) HFSS simulation results with Y-polarization (Y-pol.). A Gaussian input beam with $E_0 = 1 \text{ V/m}$ and beam waist radius = $50 \mu\text{m}$ (incident cone half angle = 30° implied) was used.

2.2 Physical Properties and Symbols

Here are definitions of relevant physical constants and various properties.

$$k_B = 1.38 \times 10^{-23} \text{ J/K} : \text{ Boltzmann constant,} \quad (2.2.1)$$

$$m^* = 0.067 \times 9.1 \times 10^{-31} \text{ kg} : \text{ effective mass of conduction band electrons in GaAs}$$

$$\text{with low electric field } (\Gamma \text{ valley}), \quad (2.2.2)$$

$$\varepsilon = 12.9 \times 8.85 \times 10^{-12} \text{ F/m} : \text{ permittivity (or dielectric constant) of GaAs (valid for} \\ < 8 \text{ THz),} \quad (2.2.3)$$

$$\varepsilon_0 = 8.85 \times 10^{-12} \text{ F/m} : \text{ vacuum permittivity (dielectric constant of vacuum),} \\ (2.2.4)$$

$$\mu : \text{ electron mobility of GaAs, } = 0.65 \text{ m}^2/\text{Vs} \text{ at 300 K, with low electric field } (\Gamma \\ \text{valley}), \quad (2.2.5)$$

$$\sigma_{th, GaAs} = 55 \text{ W/m}\cdot\text{K} : \text{ thermal conductivity of GaAs lattice atoms,} \quad (2.2.6)$$

$$n : \text{ electron density,} \quad (2.2.7)$$

$$W = 3.3 \text{ } \mu\text{m} : \text{ width of the gated active region,} \quad (2.2.8)$$

$$L = 6 \text{ } \mu\text{m} : \text{ length of the gated active region,} \quad (2.2.9)$$

$$A = W \cdot L = 20 \text{ } \mu\text{m}^2 : \text{ area of the gated active region,} \quad (2.2.10)$$

$$d = 0.2 \text{ } \mu\text{m} : \text{ distance between the front gate and back gate = thickness of the} \\ \text{MBE grown n-type doped layer,} \quad (2.2.11)$$

$$C_1 = \varepsilon \frac{A}{d} = 0.0113 \text{ pF} : \text{ capacitance formed by the double gates and the} \\ \text{dielectric (GaAs),} \quad (2.2.12)$$

$\delta \sim 0.04 \mu\text{m}$: effective thickness of the sheet of the electron gas in GaAs FET
(< d, due to the Schottky depletion from the gates), (2.2.13)

$N_S = n^* \delta$: electron sheet density, (2.2.14)

$\omega_0 = 2\pi f_0 = \sqrt{\frac{n_+ e^2}{\epsilon m^*}}$: Bare harmonic oscillator frequency (rad/s) (2.2.15)

For plasma resonance at 1 THz, $n_+ = 1.08 \times 10^{16} \text{ cm}^{-3}$ is required.

$\Gamma = \frac{1}{\tau} \left(= \frac{1}{\tau_\epsilon} \right)$: decay rate (rad/s) (2.2.16)

, or the full width at half maximum (FWHM) of the electron plasma resonance
, where $\tau (= \tau_\epsilon)$ is the energy relaxation time due to polar optical phonon scattering process [17].⁴ A quantitative form of $\tau (= \tau_\epsilon)$ as a function of temperature can be found from p.209 of K. Seeger, Ref. [42] (see Fig. 2.4 for a plot):

$$\tau_\epsilon(T) = \frac{0.47}{\alpha \omega_0} \frac{\sinh(\Theta/2T)}{(\Theta/2T)^{5/2} K_0(\Theta/2T)} \quad (2.2.17)$$

⁴ Jan 2007 correction: near eq.(4) of the Reference, $2\pi\Gamma$ was incorrectly stated as HWHM in rad/s (This is a typo, plus probably a misnomer). Mark's Γ was correctly defined as $1/2\tau$ elsewhere in the paper: **HWHM = Mark's $\Gamma = 1/2\tau$** . In addition, Mark's Γ was confused by me with $\text{FWHM} = 1/\tau$, since Γ usually denotes FWHM and γ denotes HWHM in the textbooks I have. This misled me to define **incorrect $\Gamma = 1/2\pi\tau$** , which **underestimates Γ by a factor of π** . The **real part of the impedance Z_{FET}** in eq.(2.3.7) is inversely proportional to Γ , and therefore **was overestimated by the same factor π** . The textbook convention ($\text{FWHM} = \Gamma = 1/\tau$) is used in eq.(2.2.16) and throughout this work.

, where $\Theta = 417$ K is the Debye temperature of GaAs, $\alpha = 0.067$ is the dimensionless polar constant of GaAs, $\omega_0 = \frac{k_B \Theta}{\hbar}$, and K_0 is the modified Bessel function of the second kind. The temperature dependence originates from the change of distribution of phonon states with temperature that is available for the scattering events.

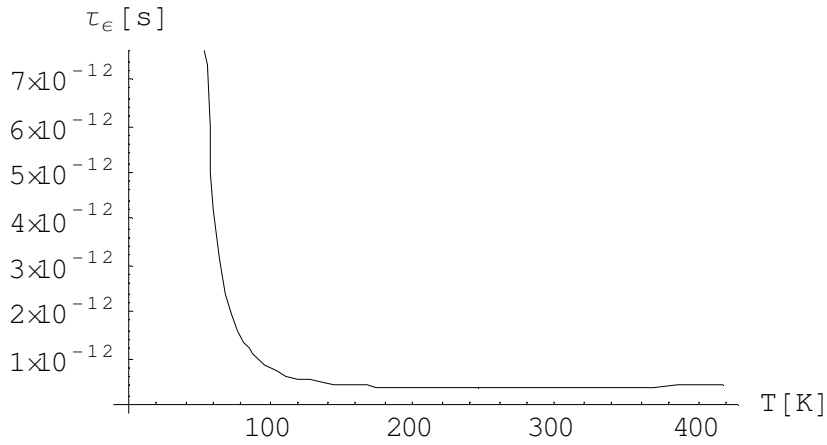


Figure 2.4 Energy relaxation time (τ_ϵ) as a function of GaAs lattice temperature. The relaxation is due to the polar optical phonon scattering process. $\tau_\epsilon \sim 0.36$ ps at 300 K. See Seeger, Ref. [42].

Energy relaxation always accompanies a momentum relaxation. However, a momentum can relax before τ_ϵ (i.e., without energy relaxation). A quantitative form of the energy-conserved momentum relaxation time $\tau_{m,\epsilon}$ as a function of temperature can be obtained from $1/\tau_{m,\epsilon}$ in p.210 of K. Seeger, Ref. [42] (see Fig. 2.5 for a plot):

$$\tau_{m,\epsilon}(T) = \frac{3\pi^{1/2}}{2^{5/2}} \frac{1}{\alpha\omega_0} \frac{\sinh(\Theta/2T)}{(\Theta/2T)^{3/2} K_1(\Theta/2T)} \quad (2.2.18)$$

, where K_1 is the modified Bessel function of the second kind.

The momentum relaxation time is smaller of the two (τ_ε and $\tau_{m,\varepsilon}$):

$$\tau_m(T) = \min(\tau_\varepsilon(T), \tau_{m,\varepsilon}(T)). \quad (2.2.19)$$

Near room temperature, $\tau_{m,\varepsilon}$ is smaller than τ_ε . Therefore, $\tau_m = \tau_{m,\varepsilon}$ may be used.

The electron mobility is given by:

$$\mu(T) = \frac{e\tau_m(T)}{m^*}. \quad (2.2.20)$$

However, this formula was not actually used, since it overestimates the electron mobility compared to what was found in literature. Instead, an empirical formula (2.6.1.1) has been extracted from the literature and used.

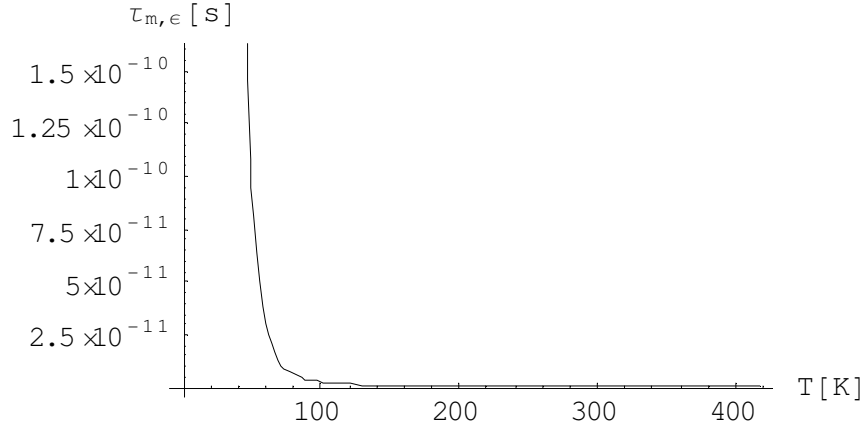


Figure 2.5 Energy-conserved momentum relaxation time ($\tau_{m,\varepsilon}$) as a function of GaAs lattice temperature. The relaxation is due to the polar optical phonon scattering process. See Seeger, Ref. [42].

2.3 Coupling Channel Impedance of GaAs

FET, Z_{FET}

The electron gas follows the damped, driven, simple harmonic oscillator equation of motion⁵:

$$\ddot{x} + \Gamma\dot{x} + \omega_0^2 x = -\frac{e}{m^*} E_{THz} e^{j\alpha} \quad (2.3.1)$$

, where $E_{THz} e^{j\alpha}$ is the terahertz electric field formed between the double gates.

Solving this equation, the displacement of electron gas, $x(t)$ is obtained.

$$x(t) = \frac{-e/m^*}{\omega_0^2 - \omega^2 + j\omega\Gamma} E_{THz} e^{j\alpha} \quad (2.3.2)$$

An electric polarization caused by the displacement is:

$$P(t) = -enx(t) = \frac{e^2 n / m^*}{\omega_0^2 - \omega^2 + j\omega\Gamma} E_{THz} e^{j\alpha}. \quad (2.3.3)$$

Electric polarization causes voltage drop across the double gates.

$$V(t) = E_{THz} e^{j\alpha} \cdot d - \frac{P(t)\mathcal{D}}{\epsilon} = \left(d - \frac{e^2 N_S}{\epsilon m^*} \frac{1}{\omega_0^2 - \omega^2 + j\omega\Gamma} \right) E_{THz} e^{j\alpha} \quad (2.3.4)$$

Current through this system can be obtained as follows:

$$Q(t) = C_1 E_{THz}(t) d = \epsilon \frac{A}{d} E_{THz} e^{j\alpha} d = \epsilon A E_{THz} e^{j\alpha} \quad (2.3.5)$$

⁵ See Appendix for the choice of j instead of i for the imaginary number.

$$I(t) = \dot{Q}(t) = j\omega\epsilon A E_{THz} e^{j\omega t} \quad (2.3.6)$$

Impedance can be calculated from the ratio of voltage and current.

$$\begin{aligned} Z_{FET} &= \frac{V(t)}{I(t)} \\ &= \frac{d}{j\omega\epsilon A} + \frac{1}{\frac{(\omega\epsilon)^2 A m^* \Gamma}{e^2 N_s} + j\omega \frac{(\omega\epsilon)^2 A m^*}{e^2 N_s} - j\omega \frac{(\omega_0\epsilon)^2 A m^*}{e^2 N_s}} \\ &= \frac{1}{j\omega C_1} + \frac{1}{\frac{1}{R_2} + \frac{1}{1/j\omega C_2} + \frac{1}{j\omega L_2}} \end{aligned} \quad (2.3.7)$$

, where

$$\begin{aligned} C_1 &= \epsilon \frac{A}{d} = 0.0113 \text{ pF} \\ R_2 &= \frac{e^2 N_s}{(\omega\epsilon)^2 A m^* \Gamma} \\ C_2 &= \frac{(\omega\epsilon)^2 A m^*}{e^2 N_s} \\ L_2 &= \frac{e^2 N_s}{(\omega\omega_0\epsilon)^2 A m^*} \end{aligned} \quad (2.3.8)$$

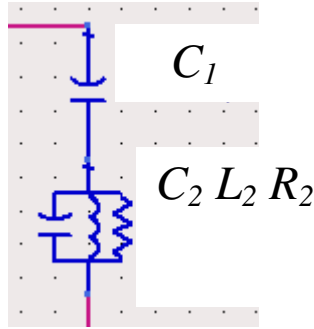


Figure 2.6 Lumped model equivalent circuit diagram of the GaAs field-effect-transistor. C_1 is the capacitance formed by the double gates and the dielectric (GaAs). The effect of plasmons appears as a parallel $R_2 L_2 C_2$ circuit.

As a result, we obtain a lumped model equivalent circuit as shown in Fig. 2.6. The circuit consists of a series connection of a capacitor C_1 and a parallel $R_2C_2L_2$ circuit. C_1 (same as eq. (2.2.12)) is the capacitance formed by the double gates and the dielectric (GaAs). The parallel $R_2C_2L_2$ sub-circuit is the effect of plasmons. At 1 THz, R_2C_1 time is

$$R_2C_1 = 0.073 \text{ ps.} \quad (2.3.9)$$

One may also find it interesting that R_2C_2 time is simply τ

$$R_2C_2 = 1 / \Gamma = \tau \quad (2.3.10)$$

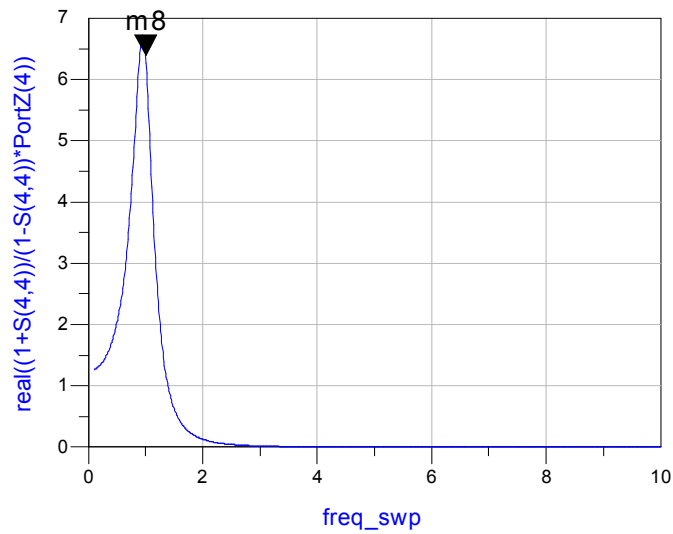
The frequency dependence of the impedance of the field-effect-transistor can be obtained analytically using the above formulas eq. (2.3.7) and eq. (2.3.8). At 1 THz, the impedance is $6.4 - j 14 \Omega$. Fig. 2.7 shows the results obtained from equivalent circuit simulations with advanced design system (ADS), where the R_2 , C_2 , and L_2 of eq.(2.3.8) were entered as frequency dependent lumped circuit elements in Fig. 2.6. In ADS, the impedance was derived from the available S parameter output. S_{11} parameter is defined as

$$S_{11} = \frac{Z_{FET} - Z_0}{Z_{FET} + Z_0} \quad (2.3.11)$$

, where $Z_0 = 50 \Omega$.

Therefore,

$$Z_{FET} = \frac{1 + S_{11}}{1 - S_{11}} Z_0 \quad (2.3.12)$$

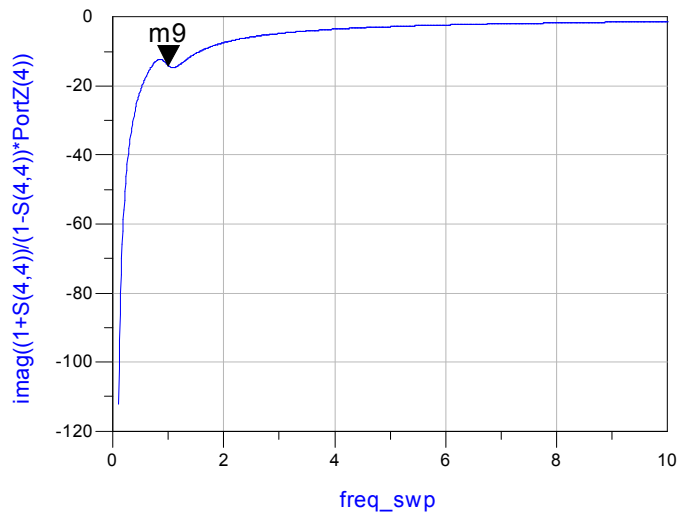


```

m8
freq_swp=1.000
real((1+S(4,4))/(1-S(4,4))*PortZ(4))=6.396

```

(a)



```

m9
freq_swp=1.000
imag((1+S(4,4))/(1-S(4,4))*PortZ(4))=-14.072

```

(b)

Figure 2.7 (a) real and (b) imaginary part of the coupling channel impedance of the GaAs FET (Z_{FET}) obtained from lumped model equivalent circuit simulation with advanced design system (ADS). $Z_{FET} = 6.4 - j14 \Omega$ at 1 THz.

2.4 Power Coupling Efficiency, α

All of the relevant loss mechanisms – mismatch of impedances, re-radiation, ohmic heating, reflections, and the mode-mismatch between the free-space terahertz radiation with the radiation pattern of the antennas – are taken into account (see Fig. 2.8).

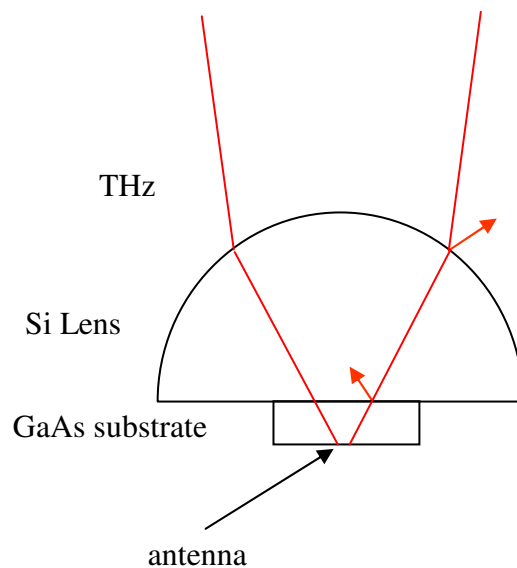


Figure 2.8 Coupling of free-space terahertz radiation into the detector chip. The reflections at the air-silicon lens interface can be reduced if coated with parylene.

According to Paolo's simulation, 28% is already lost at the air-silicon lens coupling, so 72% gets coupled into the silicon lens. Note this loss can be reduced if the silicon lens was coated with parylene anti-reflection coating [44]. Professor E. R. Brown's Lab. has this coating equipment. Or, it can be done through a company elsewhere.

By iteratively modifying the designs of gate length, width, thickness, CPW, and transmission lines, the impedance of GaAs FET was tuned to

$$Z_{FET} = 20 - j14 \Omega \quad (2.4.1)$$

, and the input impedance of the antenna system “seen by the GaAs FET” was tuned to

$$Z_{ANT} = 23 - j29 \Omega. \quad (2.4.2)$$

If only the mismatch of impedances from the antenna system to the GaAs FET is considered, the power coupling efficiency is given by

$$1 - \left| \frac{Z_{FET} - Z_{ANT}}{Z_{FET} + Z_{ANT}} \right|^2 = 93\%. \quad (2.4.3)$$

Eq. (2.4.3) becomes 100% when $Z_{FET} = Z_{ANT}$. However, multiple reflections and multiple impedance mismatching points throughout the entire system must be considered. With such considerations, complex conjugate matching ($Z_{FET} = Z_{ANT}^*$) results in the most power transfer into the GaAs FET (see Appendix C and Ref. [45]). However, complex conjugate matching implies equal amount of power dissipated by Z_{FET} and Z_{ANT} (see Appendix C and Ref. [45]). Therefore, of all the 72% that made into the silicon lens, 36% would be the theoretical upper bound for the power delivered to the GaAs FET.

Paolo’s simulation with the imperfect impedance matching (with eq. (2.4.1) and eq. (2.4.2)) resulted in the overall coupling efficiency of

$$\alpha(Z_{FET} = 20 - j14 \Omega) = 27 \% \quad (2.4.4)$$

, which is still remarkable for free-space terahertz coupling (also note $\alpha < 36\%$).

As mentioned earlier in Section 2.2, the real part of Z_{FET} (eq. (2.4.1)) was overestimated by a factor of π . As a lower bound, 7 % overall coupling efficiency was obtained from Paolo's simulation with $Z_{FET} = 3.2 - j14$:

$$\alpha(Z_{FET} = 3.2 - j14) = 7 \% \quad (2.4.5)$$

The impedance of the GaAs FET after the correction is given by

$$Z_{FET} = 6.4 - j14 \quad (2.4.6)$$

The corresponding overall coupling efficiency for this value of Z_{FET} should be between 7% and 27%, and could be roughly interpolated to 10% (see Fig. 2.9).

$$\alpha(Z_{FET} = 6.4 - j14) \sim 10 \% \quad (2.4.7)$$

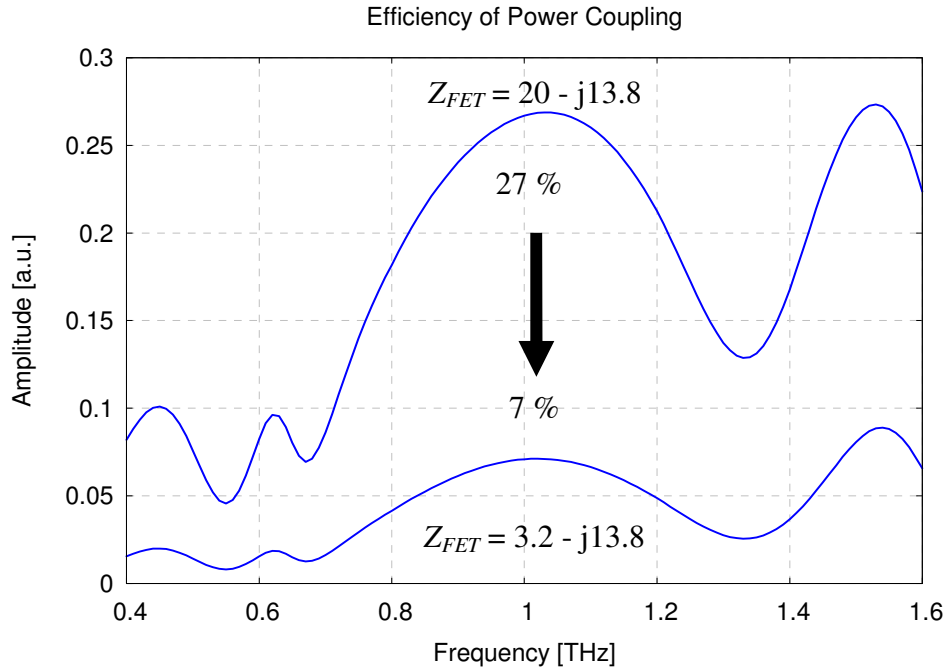


Figure 2.9 Overall power coupling efficiency includes all loss mechanisms. The coupling efficiency for $Z_{FET} = 6.4 - j14$ may be roughly interpolated to 10%. Figure provided by Paolo Focardi, JPL, NASA.

Thanks to the good thermodynamic properties of the GaAs metal-semiconductor-field-effect-transistor (MESFET) and the sensitivity of the detection mechanism, a dynamic range of 70 dB is achieved for the detectable terahertz power ($0.1 \mu\text{W} \sim 1 \text{ Watt}$).

Thermal conductance (or heat flow rate) from the electrons to the active region GaAs lattice (G_{el}) can be obtained by multiplying the heat capacity of an ideal gas by the energy relaxation rate:

$$G_{el} = \frac{3}{2} (n \times WL \delta) \cdot k_B \times \Gamma \sim 4.6 \times 10^{-7} \text{ W/K.} \quad (2.5.2)$$

The heat can flow out of the active region of the GaAs FET through metal gates and GaAs mesa, then eventually to the heat bath. The lower bound of the thermal conductance from the active region GaAs lattice atoms to the heat bath ($G_{lattice}$) can be roughly estimated by considering only a few of all the possible heat flow channels. If the heat flow through the cross-sections of the GaAs mesa (area = $W \times L = 3.3 \mu\text{m} \times 6 \mu\text{m}$) is considered,

$$G_{lattice} > \sigma_{th, GaAs} \frac{W \cdot L}{d/2} \times 2 \sim 2.18 \times 10^{-2} \text{ W/K.} \quad (2.5.3)$$

As $G_{lattice}$ is greater than G_{el} by five orders of magnitude, the GaAs mesa alone can pull enough of the absorbed energy out of the electron as quickly as needed. The figure would get even better if other channels of heat dissipation are considered. For the completeness of the argument, here are those considerations: The thickness of the gate metals is $0.24 \mu\text{m}$ (Ti / Pt / Au = 200 / 200 / 2000 Å). The

front gate is making contact with air, so most of the heat flow must occur through the cross-section area = $6 \mu\text{m} \times 0.24 \mu\text{m}$. Having similar cross-sectional area and thermal conductivities as the GaAs mesa (thermal conductivity of GaAs = 55 W/m·K, Ti = 21.9 W/m·K, Pt = 71.6 W/m·K, Au = 318 W/m·K), the heat flow through the front gate would be more or less the same magnitude as the heat flow through the GaAs mesa. The back gate is making contact with epoxy layer with unknown thermal conductivity [46]. Nevertheless, it would be safe to assume that the thermal conductance of the epoxy is low. As before, most of the heat flow would occur through the $6 \mu\text{m} \times 0.24 \mu\text{m}$ cross-section area. As a whole, the thermal conductance G_{lattice} would be greater than, but similar to, 1.82×10^{-2} W/K.

Note the assumption $\Delta T_{\text{lattice}} \sim 0$ in eq.(2.5.1) would be valid for mild terahertz radiations only (e.g., microwatt-level terahertz radiation from the Virginia diode sources). If kW-level terahertz radiations from the UCSB free electron lasers (FELs) were used, the assumption would be invalid.

Calculation shows that $0.4 \mu\text{W}$ dissipated by the electron plasma would raise T_{el} by 0.82 K, but raise T_{lattice} only by $< 22 \mu\text{K}$. Considering the dynamic thermal equilibrium, inflow and outflow of the heat should be equal. Therefore,

$$0.4 \mu\text{W} = G_{\text{el}} \Delta T_{\text{el}} = G_{\text{lattice}} \Delta T_{\text{lattice}} \quad (2.5.4)$$

, where $\Delta T_{\text{el}} = T_{\text{el}} - T_{\text{lattice}}$, $\Delta T_{\text{lattice}} = T_{\text{lattice}} - 300$ K. From these equations, the change of electron temperature (ΔT_{el}) and lattice temperature ($\Delta T_{\text{lattice}}$) can be obtained:

$$\Delta T_{el} = \frac{0.4 \mu W}{G_{el}} \sim 0.82 \text{ K} \quad (2.5.5)$$

$$\Delta T_{lattice} = \frac{G_{el} \Delta T_{el}}{G_{lattice}} < 22 \mu K \quad (2.5.6)$$

In comparison, if 20 Watt dissipated by the electron plasma is assumed, $\Delta T_{el} \sim 4.1 \times 10^7 \text{ K}$, and $\Delta T_{lattice} \sim 1100 \text{ K}$ are obtained. The melting temperature of GaAs is about 1500 K. So, depending on how the kW-level output of the FEL is coupled into the system, it could melt down the GaAs (see Fig. 2.11).

The DC source-to-drain bias voltage ($V_{SD} = V_D$) also raises T_{el} and $T_{lattice}$ by ohmic heating. The power dissipated by the ohmic heating is given by:

$$P_{DC} = \frac{(V_{SD})^2}{R_{SD}}. \quad (2.5.7)$$

Assuming a thermal equilibrium,

$$P_{DC} = G_{el} \Delta T_{el} = G_{lattice} \Delta T_{lattice} \quad (2.5.8)$$

ΔT_{el} and $\Delta T_{lattice}$ due to the ohmic heating are obtained:

$$\Delta T_{el} = \frac{P_{DC}}{G_{el}} = \frac{(V_{SD})^2}{G_{el} R_{SD}} \quad (2.5.9)$$

$$\Delta T_{lattice} = \frac{P_{DC}}{G_{lattice}} = \frac{(V_{SD})^2}{G_{lattice} R_{SD}} \quad (2.5.10)$$

As estimates for typical bias conditions, $\Delta T_{el} = 12 \text{ K}$ and $\Delta T_{lattice} = 0.32 \text{ mK}$ are obtained with $V_{SD} = 0.5 \text{ V}$. $\Delta T_{el} = 51 \text{ K}$ and $\Delta T_{lattice} = 1.37 \text{ mK}$ are obtained with $V_{SD} = 1.0 \text{ V}$.

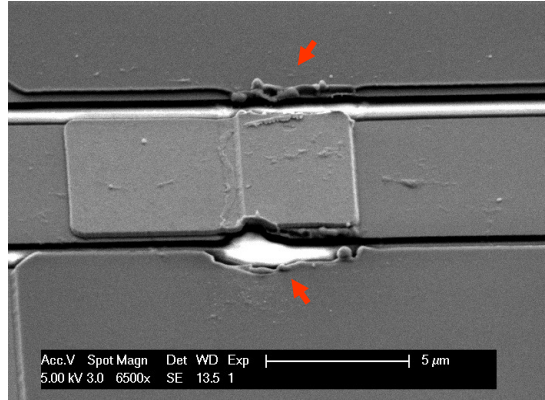


Figure 2.11 Scanning electron microscopy image of a sample destroyed by the full power of the free electron laser. Red arrows indicate the defects.

2.6 Readout Channel

Sections 2.3 and 2.4 dealt with coupling channel. This section will discuss the readout channel. For the bolometric detection mode, high rate of change of the readout resistance (source-to-drain resistance, $R = R_{SD}$) is desired. As a function of temperature (T), the readout resistance ($R(T)$) can be expressed as:

$$R(T) = R_{SD}(T) = \frac{1}{n(T) e \mu(T)} \times \frac{L}{W \cdot \delta} \quad (2.6.1)$$

, where $T = T_{lattice} = T_{el}$.

The temperature dependence of various quantities in this section assumes heating of the lattice *and* the electrons. As seen in Section 2.5, the terahertz input changes T_{el} significantly, but not $T_{lattice}$. So it is assumed here that the change of the readout resistance due to the electron heating *only*, is similar to the change due to the lattice *and* electron heating. If the former is significantly lower than the latter, it

can be responsible for the absence of the detector response following the proposed detection model.

2.6.1 Electron Mobility, $\mu(T)$

Electron mobility of GaAs at room temperature (300 K) is dominated by the polar optical phonon scattering process [47, 48]. An analytical form of the momentum scattering time can be found from Ref. [42]. However, the formula overestimates the mobility when compared with the literature (see Fig. 2.12, 2.13 and 2.14). For this work, therefore, an empirical formula

$$\mu(T) = 10^{\frac{\text{Log}_{10}(0.33 \cdot 10^4) - \text{Log}_{10}(0.61 \cdot 10^4)}{500 - 300} (T - 300) + \text{Log}_{10}(0.61 \cdot 10^4)} \quad (2.6.1.1)$$

is extracted from J. S. Blakemore [48] as a good approximation (see Fig. 2.12 for plot).

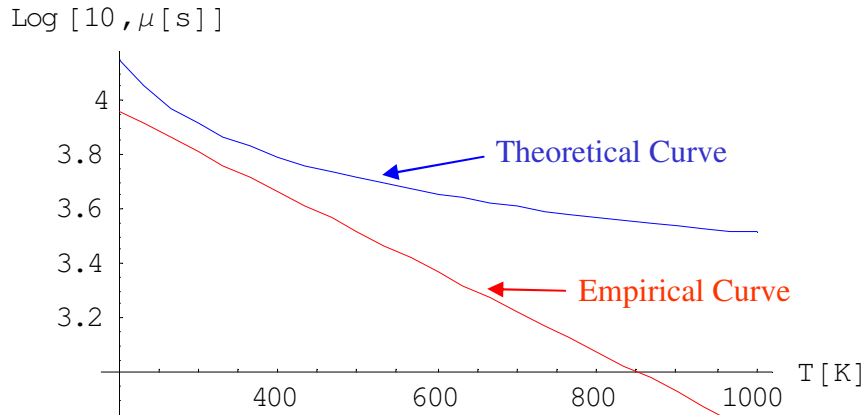


Figure 2.12 Theoretical and empirical electron mobility as functions of GaAs lattice temperature.

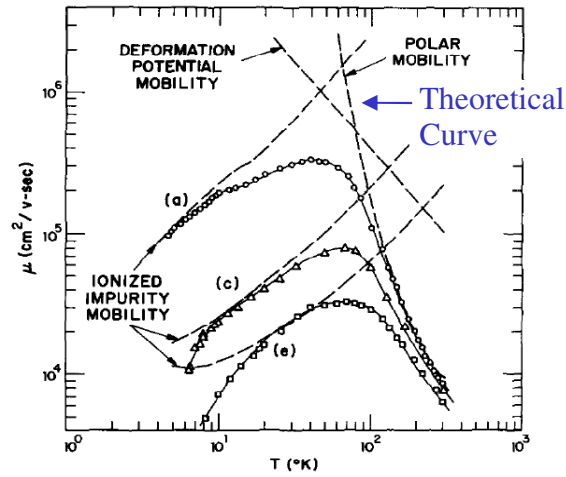


Fig. 2. Temperature variation of Hall mobility at 5 kG for three samples. In the temperature range from 300 to 77°K the mobility of sample (a) is dominated by polar mode scattering. Samples (c) and (e) show increased effects of ionized impurity scattering.

Figure 2.13 Electron mobility as a function of temperature for $T < 300$ K. From Stillman *et al.*, Ref. [47].

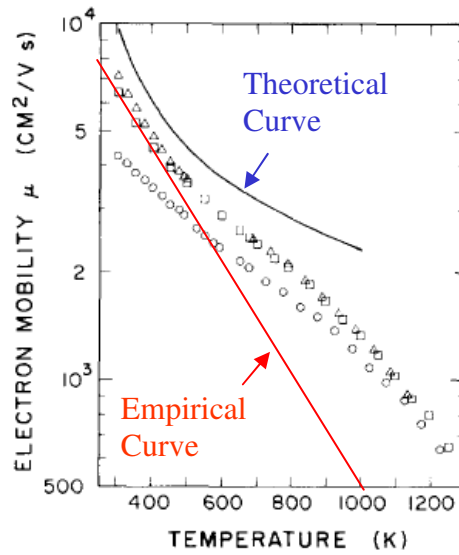


Figure 2.14 Electron mobility as a function of temperature for $T > 300$ K. From Blakemore *et al.*, Ref. [48].

2.6.2 Electron Number Density, $n(T)$

Additional properties and symbols will be defined for the use in this section only (see pages 15~19 of S. M. Sze, Ref. [49]).

$$m_{de} = 0.067 \quad : \text{electron effective mass,} \quad (2.6.2.1)$$

$$m_{dh} = (0.082^{3/2} + 0.45^{3/2})^{2/3} \quad : \text{hole density-of-state effective mass,} \quad (2.6.2.2)$$

$$E_g(T) = 1.519 - \frac{5.405 \times 10^{-4} T^2}{T + 204} \quad : \text{empirical equation for the GaAs bandgap energy.} \quad (2.6.2.3)$$

$$n_i(T) = 4.9 \times 10^{15} (m_{de} m_{dh})^{3/4} M_C^{1/2} T^{3/2} e^{-\frac{E_g(T)}{2k_B T}} \quad : \text{intrinsic carrier density, where} \\ M_C = 1 \text{ is the number of minima in the conduction band.} \quad (2.6.2.4)$$

$$n_{300} = 5.818 \times 10^{16} \text{ cm}^{-3} \quad : \text{extrinsic carrier density at 300 K, in order to match the} \\ \text{calculated resistance with experimentally measured resistance,} \quad (2.6.2.5)$$

$$n_e(T) = 10^{17 - \frac{300(17 - \text{Log}_{10} n_{300})}{T}} \quad : \text{extrinsic carrier density,} \quad (2.6.2.6)$$

$$n(T) = n_i(T) + n_e(T) \quad : \text{total electron density,} \quad (2.6.2.7)$$

Fig. 2.15 shows the resulting electron density vs. temperature plot.

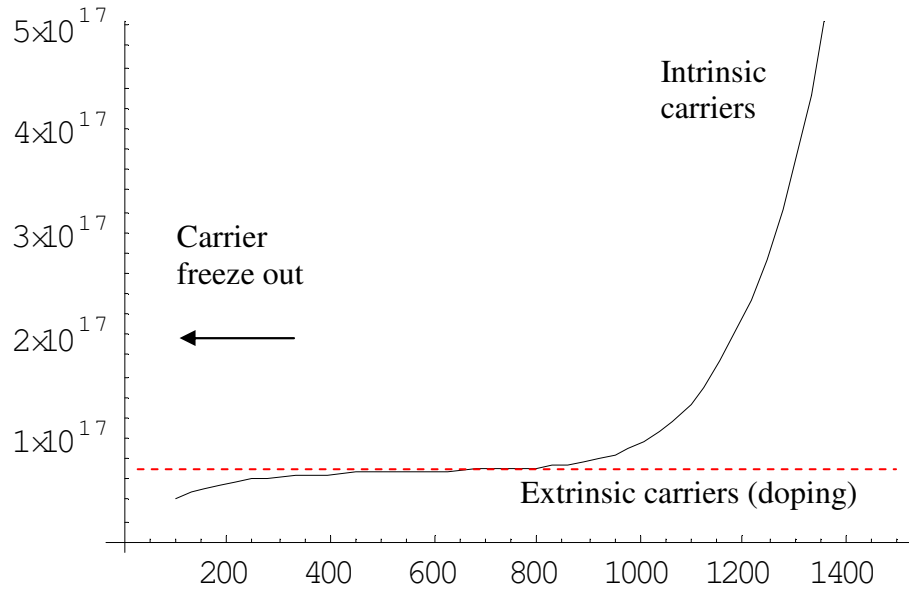


Figure 2.15 Electron density (cm⁻³) vs. temperature.

2.6.3 Read-Out Resistance, $R(T)$

Combining the results from the Sections 2.6.1 and 2.6.2, the read-out resistance as a function of temperature $R(T)$ is obtained.

$$R(T) = R_{SD}(T) = \frac{1}{n(T) e \mu(T)} \times \frac{L}{W \cdot \delta} . \quad (2.6.3.1)$$

Fig. 2.16 shows the resulting resistance vs. temperature plot.

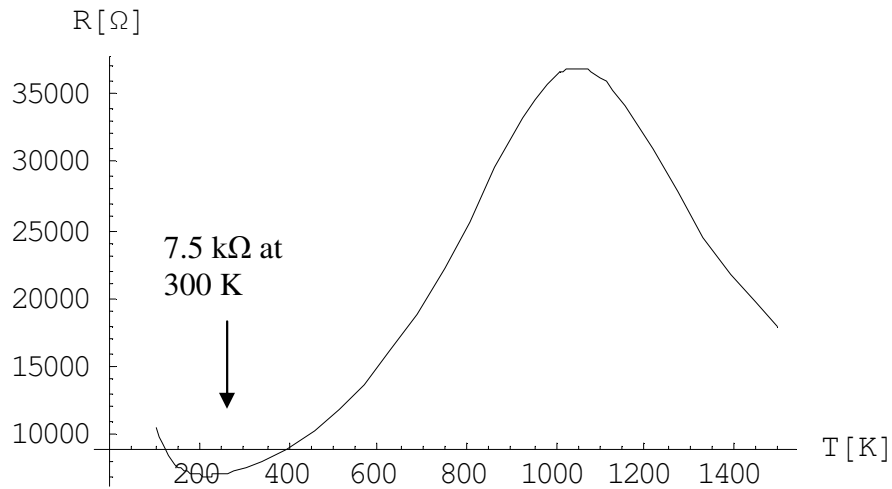


Figure 2.16 Readout (source-to-drain) resistance as a function of temperature.

2.6.4 Rate of Change of the Readout Resistance, γ

The rate of change of the resistance can be obtained.

$$\gamma(T) = \frac{1}{R(T)} \frac{\partial R(T)}{\partial T} . \quad (2.6.4.1)$$

At room temperature (300 K), the calculation results,

$$\gamma(300) = 0.00158397 . \quad (2.6.4.2)$$

The temperature dependence of the electron mobility and electron density compensate each other to produce a small value for the rate of change of resistance. It appears to be a very small number around 0.001 at 300 K.

2.6.5 Experimental Verification of γ

IV curves at different temperature were taken (Fig. 2.17).⁶ The differential resistance was computed at $V_D = 0$ and plotted against temperature (Fig. 2.18).

From the slope of the curves, the rate of change of resistance $\gamma(T) = \frac{1}{R(T)} \frac{\partial R(T)}{\partial T}$

can be determined. The values obtained from this experiment agree with the theoretical values from Section 2.6.4 to the first effective number. $\gamma = 0.001$ is taken as a good approximation.

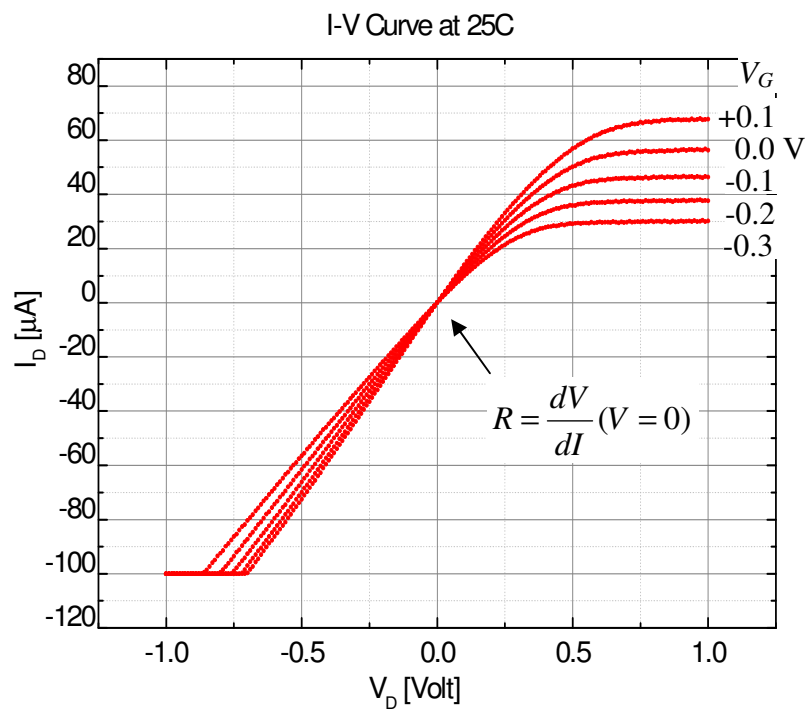


Figure 2.17 IV curves at 25 °C.

⁶ Thanks to Coldren Group for the probe station.

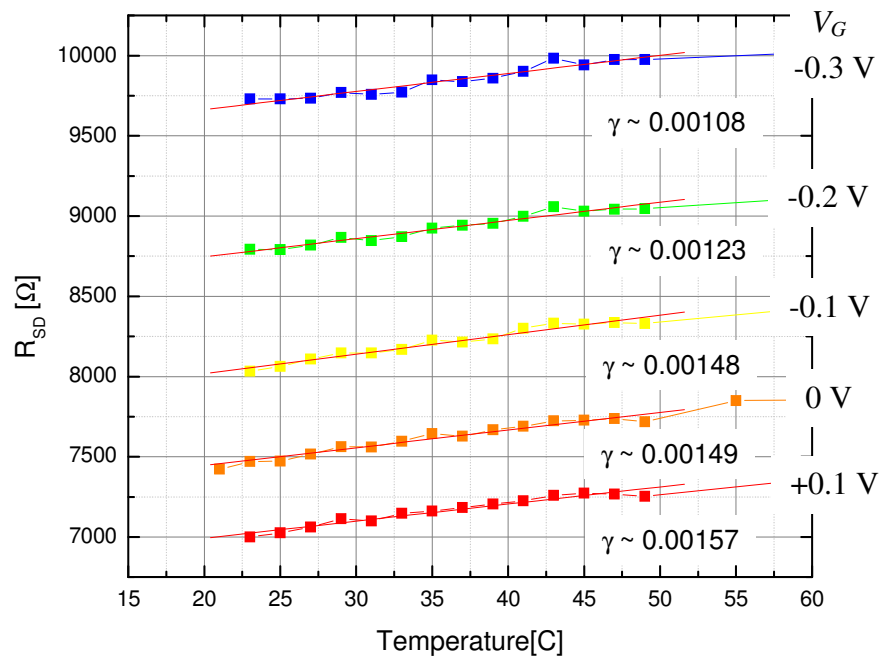


Figure 2.18 Experimental resistance versus temperature at various gate bias conditions. $\gamma = 0.001$ is taken as a good approximation.

2.7 Responsivity, \mathfrak{R} , and Noise Equivalent

Power, NEP

If the terahertz power from the source is increased by dP , the power dissipated by the electron plasma is increased by αdP , where α ($0 < \alpha < 1$) is the power coupling efficiency as discussed in Section 2.4. The induced change in the electron temperature is given by $dT_{el} = \alpha dP / G_{el}$. Therefore,

$$dP = G_{el} dT_{el} / \alpha. \quad (2.7.1)$$

The change of the read-out resistance induced by dT_{el} is $dR = R \gamma dT_{el}$, where γ is the rate of change of resistance as discussed in Section 2.6. The induced change in the read-out voltage is

$$dV_{SD} = d(IR) = I dR = (V/R) dR = V_{SD} \gamma dT_{el}, \quad (2.7.2)$$

, where V ($= V_{SD}$) and I ($= I_{SD}$) are the source-to-drain voltage and current, respectively.

Responsivity can be defined as the read-out voltage per incident power. From eq. (2.7.1) and eq. (2.7.2),

$$\mathfrak{R} = \frac{dV_{SD}}{dP} = \frac{V_{SD} \gamma dT_{el}}{G_{el} dT_{el} / \alpha} = \alpha \frac{V_{SD} \gamma}{G_{el}} \quad (\text{V/W}). \quad (2.7.3)$$

The spectral density of the Johnson noise power is given by:

$$P_N = 4k_B T_{el} \quad (\text{W/Hz}). \quad (2.7.4)$$

The root mean square of the Johnson noise voltage from R_{SD} is given by:

$$V_N = \sqrt{P_N R_{SD}} = \sqrt{4k_B T_{el} R_{SD}} \quad (\text{V/Hz}^{1/2}). \quad (2.7.5)$$

The noise equivalent power (NEP) is defined by the noise voltage divided by the responsivity (i.e., the power needed in order to achieve the same magnitude of signal as the noise). Therefore, for the Johnson noise, the NEP is given by:

$$NEP_J = \frac{\sqrt{4k_B T_{el} R_{SD}}}{\alpha \mathfrak{R}} \quad (\text{W/Hz}^{1/2}). \quad (2.7.6)$$

Likewise, the NEP due to the thermal fluctuations of the electron temperature [50, 51] is given by

$$NEP_{TF} = \frac{1}{\alpha} \sqrt{2k_B T_{el}^2 G_{el}} \quad (\text{W/Hz}^{1/2}). \quad (2.7.7)$$

These two noises add incoherently, therefore the total NEP [17]⁷ is given by

$$NEP = \sqrt{NEP_J^2 + NEP_{TF}^2} = \frac{1}{\alpha} \sqrt{\frac{4k_B T_{el} R_{SD}}{\mathfrak{R}^2} + 2k_B T_{el}^2 G_{el}} \quad (\text{W/Hz}^{1/2}). \quad (2.7.8)$$

⁷ April 24, 2006 correction: from $NEP = \sqrt{\frac{4k_B TR_{xx}}{\alpha \mathfrak{R}^2} + \frac{2k_B T^2 G}{\alpha}}$ to $NEP = \frac{1}{\alpha} \sqrt{\frac{4k_B TR_{xx}}{\mathfrak{R}^2} + 2k_B T^2 G}$, B. S. Karasik, *et al.*, APL 68, 853 (1996). Typos in eq. 7, 8 of the refernece were confirmed via email correspondences with the author.

2.8 Design Tool Software

Design tool software is programmed with Labview for ease of determining the length (L), width (W) and thickness (d) of the transistor. Basically, I have identified 4 independent variables (L , W , d , and T_{el}) from which all the other relevant quantities can be derived. See Fig. 2.19 for the design tool software and Fig. 2.20 for the dependence tree of the quantities.

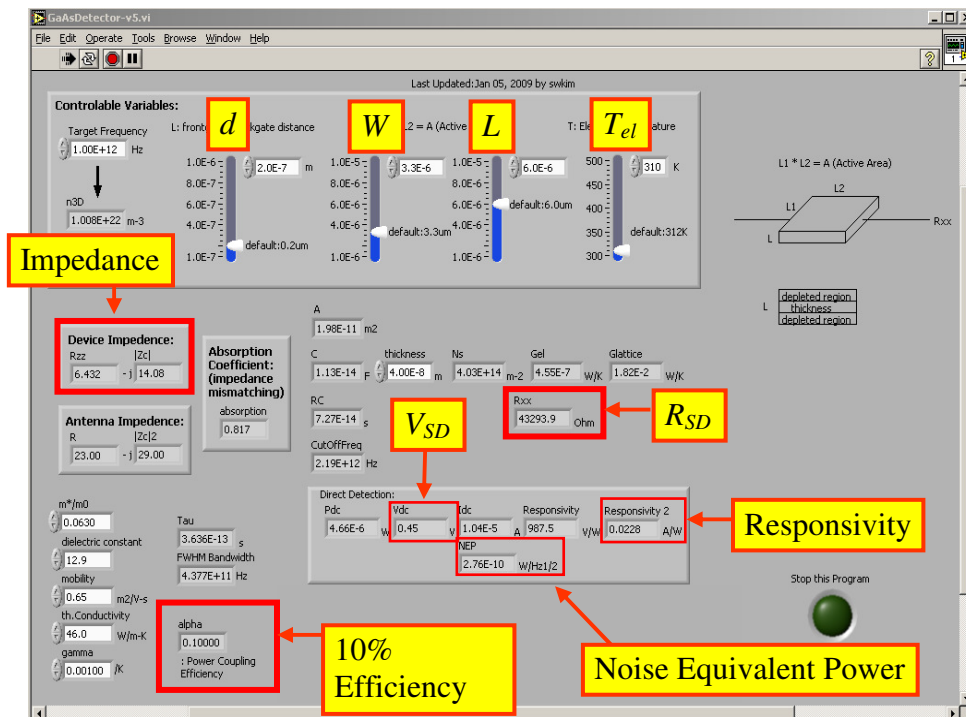


Figure 2.19 Design Tool Software which gives an expected $NEP = 2.76 \times 10^{-10}$ W/Hz^{1/2} with a readout bias voltage $V_{SD} = 0.45$ V.

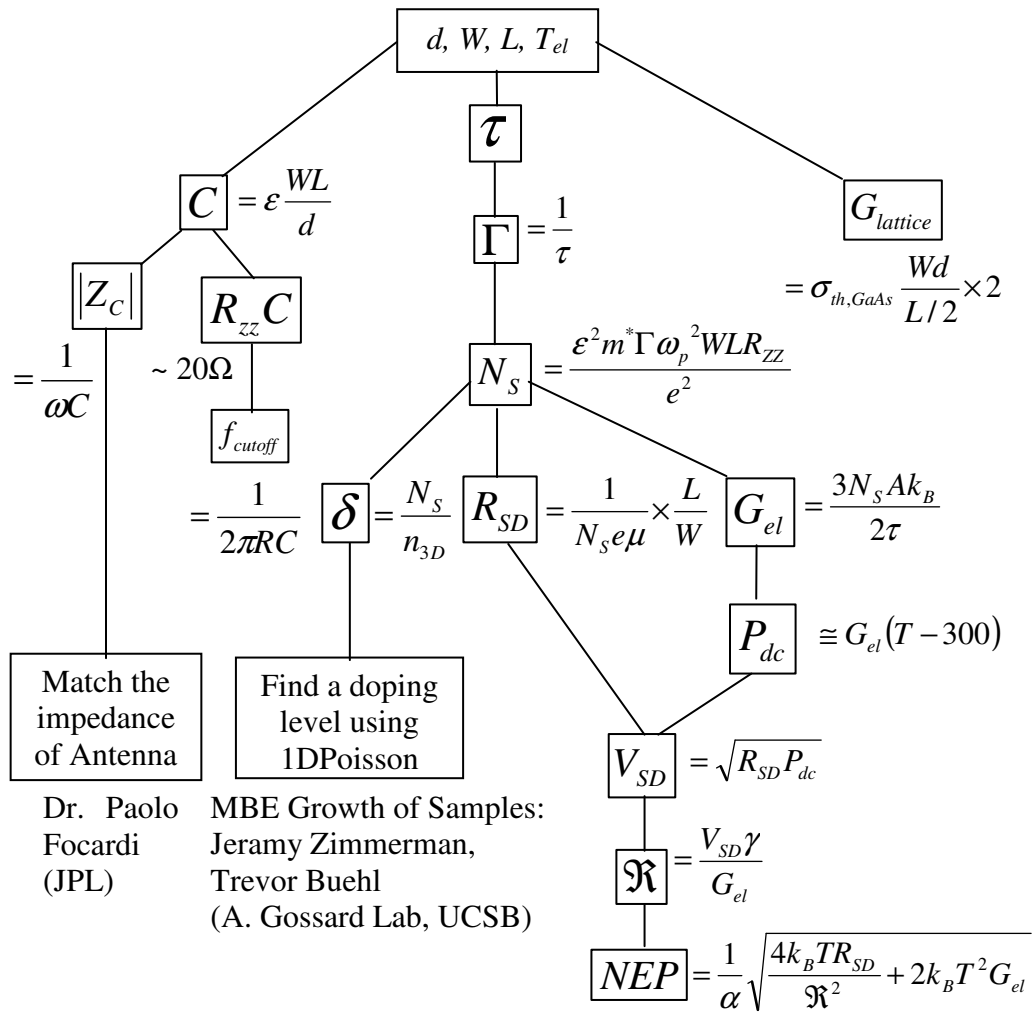


Figure 2.20 Dependence tree for all the relevant detector performance parameters.

Chapter 3 Samples

3.1 MBE Grown Wafers

Sample wafers were grown by Jeramy Zimmerman and Trevor Buhel in the Art Gossard Lab, UCSB Materials Department. Two-inch diameter, 500 μm -thick, high-resistivity, undoped GaAs wafers with crystallographic orientation (100) were used. An etch-stop layer (for spray-etch step) of thickness 1 μm was grown first, and then 0.2 μm -thick n-type doped GaAs layer was grown. The wafer was then cleaved into 4 pieces. Each quarter-wafer piece was processed separately. With a GCA stepper, 22 identical patterns were exposed in a single quarter wafer piece. One exposure area had 4 mm \times 4 mm dimensions and the areas were spaced adjacent to each other.

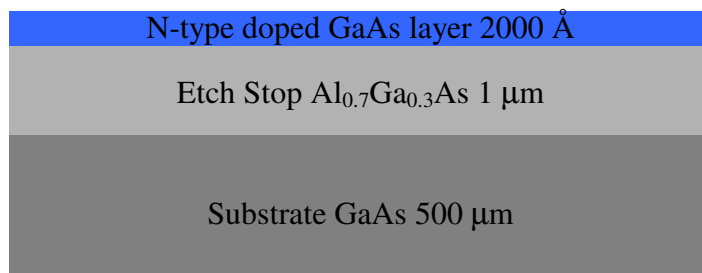


Figure 3.1 MBE Sample Structure.

3.2 Cleanroom Processing Overview

A detailed processing recipe is included in Appendix A. In the cleanroom, alignment marks, ohmic contacts, and antenna metals are formed on the MBE-grown side of the sample wafer. The processed side is bonded to another wafer (new carrier wafer) using epoxy glue [46], then the whole substrate of the sample ($\sim 500 \mu\text{m}$) is removed [52] by the spray-etch technique [53]. See Fig. 3.3 for the pictures of the set-up. The bonded wafer is mounted on a glass slide with wax and photoresist in order to keep the new carrier wafer from being etched during the spray-etch process. After the substrate removal, the sample is unmounted from the glass slide. GaAs mesa is formed followed by back gate metallization. During the mesa formation etch, all the necessary electrodes are exposed for the following electrical measurements.



Figure 3.2 Spray etch setup. Pressure is maintained at 4 ~ 4.5 pounds per square inch (psi).

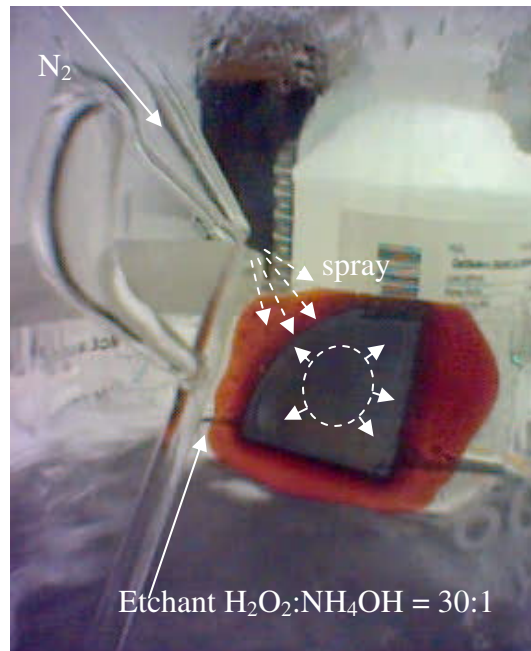


Figure 3.3 Close-up pictures of the spray etch setup. The AlGaAs etch-stop layer is reached first at the center of the wafer where the etch rate is highest. Over-etch of about 1 hour is needed in order to complete etching the whole wafer.

3.3 Silicon Lens Mount

After the cleanroom processing is finished, the wafer is diced to square chips with dimensions 4 mm by 4 mm. The detector chip is mounted on a silicon lens [54] (Fig. 3.4).

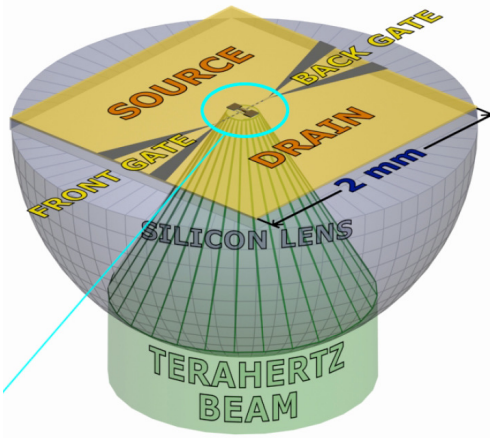


Figure 3.4 Silicon Lens mounting. Chip dimension is 4 mm x 4 mm and is greatly exaggerated in this picture.

Assuming 30° half incidence cone angle, the diffraction limited beam waist radius [55] is about 50 μm.

$$\sim \frac{0.3mm}{n_{Si} \pi \tan 30^\circ} \sim 50 \mu m \quad (3.3.1)$$

, where $n_{Si} = 3.4$ is the index of refraction of silicon.

Fig. 3.5 and 3.6 show the schematic and the pictures, respectively, of the setup that was used to align the focus of the silicon lens to the center of the detector chip.

Two 1310 nm diode lasers were used in order to locate the focus of the lens and to view the pattern on the detector chip during the manipulation.

The manipulations have been duplicated for testing the repeatability of this alignment method. By using the micrometer and the known geometry of the detector (Fig. 2.1), the method has positioning accuracy of $\pm 10 \mu\text{m}$. The table in Fig. 3.6 is the repeatability data for the sample S5-3 chip #8 on Jan 28, 2007. The numbers in the first two rows of the table are the micrometer readings at the fixed positions on the detector chip for repeated trials. A silicon-lens mounted sample is then connected to a printed circuit board (PCB) with gold wires. The front and back gates were shorted on the PCB in order to apply symmetric bias voltages to the nearly parabolic potential well.

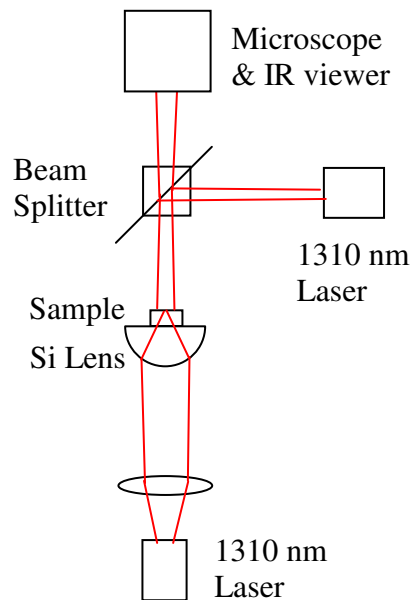
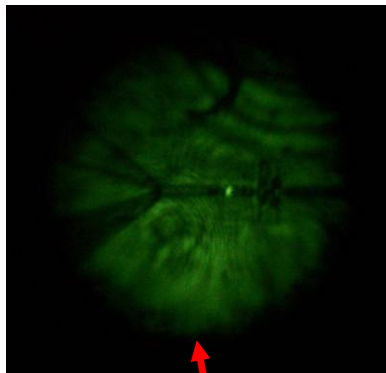
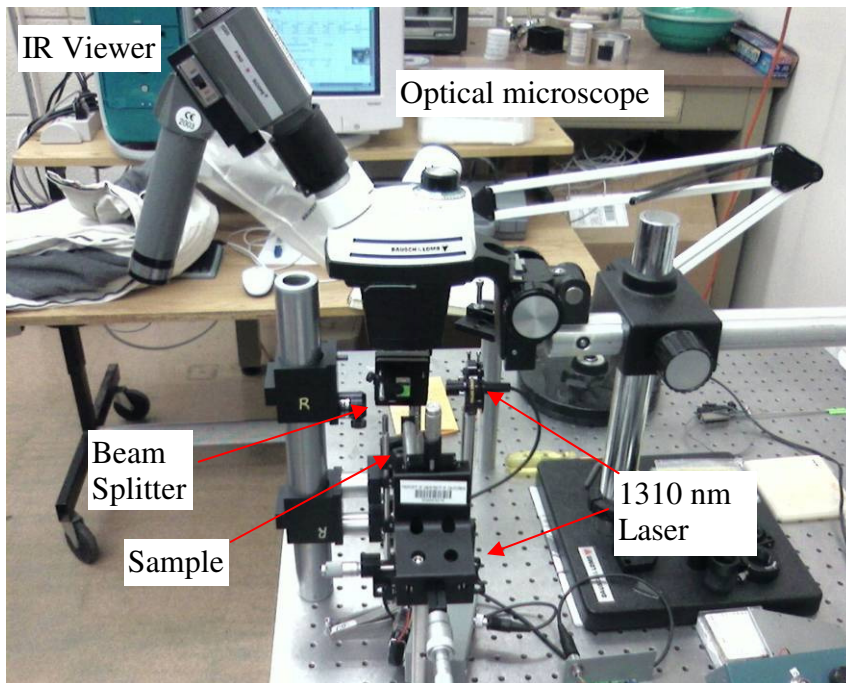


Figure 3.5 Schematic diagram of silicon lens mounting setup.



Positioning Accuracy
+/- 10 μm



	try1 (L->R)	try2(R->L)	try3	try4	try5	try6
left	38.3	28.1	38.5	28	38.1	28.1
right	69.8	59.2	70	59.6	70	59.4
difference	-31.5	-31.1	-31.5	-31.6	-31.9	-31.3

Figure 3.6 Silicon lens mount setup. Positioning accuracy of this method is within $\pm 10 \mu\text{m}$. The numbers shown in the first two rows of the table are the micrometer readings at the fixed positions on the detector chip for repeated positioning trials.

Chapter 4 Experiment

4.1 Detector Measurement Setup

A tabletop, linearly polarized, stable CW microwave source at 1 THz recently became available from Virginia Diodes, Inc. The technology starts with a 14 GHz Gunn oscillator source with ~ 100 mW output power. The output undergoes multiplication by cascaded harmonic generators and results in 1 THz radiation with 4 μ W output power. This output can be modulated with a PIN diode switch, thereby enabling lock-in measurement without a mechanical chopper. The chopping frequency was typically around 40 kHz. Note the slow detectors (e.g., Golay cells or pyros) are not able to measure such rapid modulation, nor the weak power.

See Fig. 4.1 for the schematic diagram of the detector measurement setup. A current preamplifier (Stanford Research, model SR570) was used for biasing the drain and readout of the signal. A source meter (Keithley, model KE2400) was used for biasing the gates. The signal from the current preamplifier was fed to a lock-in amplifier (Stanford Research, model SR830) or a spectrum analyzer (Stanford Research, model SR760). Using two wire grid polarizers (P1 and P2), the

polarization and the power dependence of the detector response could be examined without changing the alignment of the setup. By fixing P2 at 0° or 90°, the polarization of the input terahertz radiation is chosen as X-polarization (X-pol.) or Y-polarization (Y-pol.), respectively. By rotating P1, the magnitude of the input terahertz power is modulated.

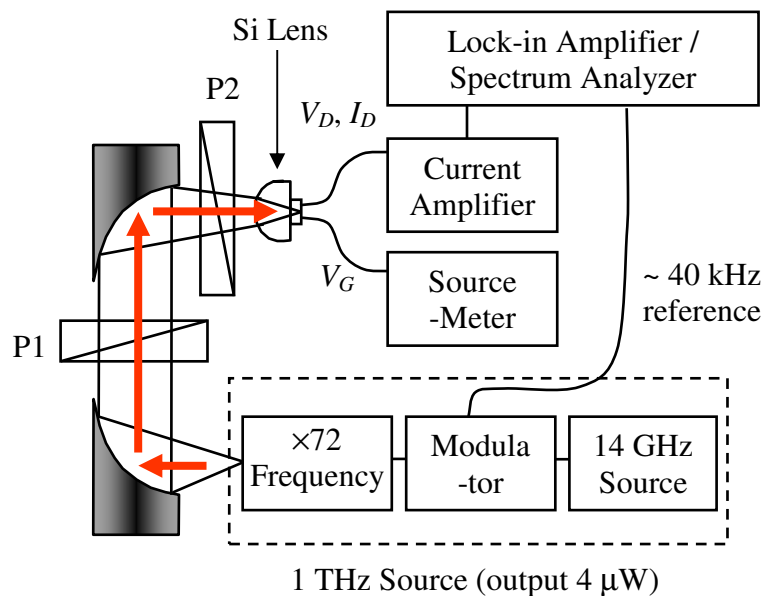


Figure 4.1 Detector measurement setup with lock-in amplifier or spectrum analyzer. P1 and P2 stand for the two rotating wire-grid polarizers.

Combining polarizations of the P2 and the source results in four possible configurations of setup: (A, B, C, and D in Fig. 4.2). If the source and the P2 are parallel, the angle dependence of the output radiation intensity is $(\cos\theta)^4$, whereas if the source and P2 are crossed, the angle dependence is $(\cos\theta \sin\theta)^2$.

(a)

	Polarization angles (X-pol. = 0°, Y-pol. = 90°)			Source-P2 alignment	Terahertz input to the detector	
	Terahertz Source	P1	P2		Polariz- ation	Intensity
A	X-pol.	θ	X-pol.	Parallel	X-pol.	$I_0 (\cos\theta)^4$
B		θ	Y-pol.	Crossed	Y-pol.	$I_0 (\cos\theta \sin\theta)^2$
C	Y-pol.	θ	X-pol.	Crossed	X-pol.	$I_0 (\cos\theta \sin\theta)^2$
D		θ	Y-pol.	Parallel	Y-pol.	$I_0 (\cos\theta)^4$

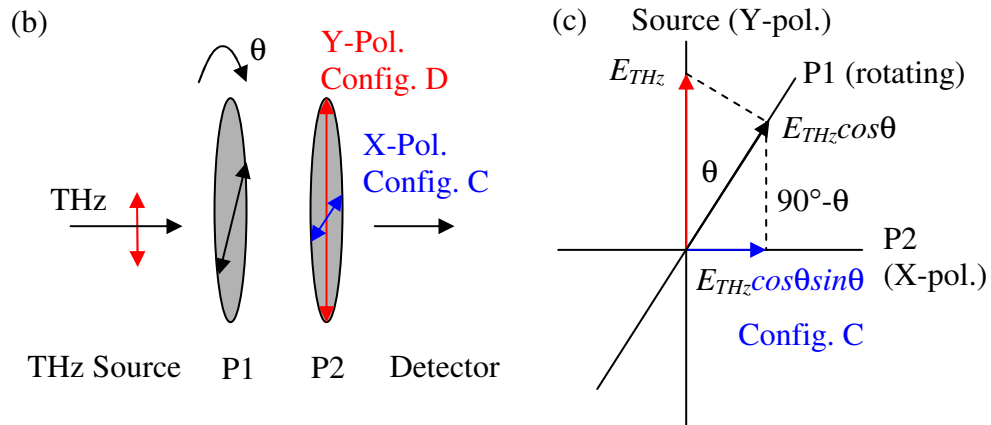


Figure 4.2 (a) Table of four possible configurations (A, B, C, and D) for the polarizations of the detector measurement setup. (b) is the schematic diagram of configurations C and D. (c) shows the projections of the electric fields for the configuration C.

See Fig. 4.3 for the plot of the normalized intensity (I / I_0) vs P1 angle θ . For example, configuration A measures the detector responsivity for X-pol. and the angle dependence of the input power is $(\cos\theta)^4$. Configuration B measures the detector responsivity for Y-pol. and the angle dependence of the input power is

$(\sin\theta\cos\theta)^2$. The range of the terahertz input to the detector is reduced for configurations B and C by 1/4 since the source and P2 are cross-polarized. A polarization rotator composed of a wire grid polarizer at 45° and a mirror would solve this problem [56].

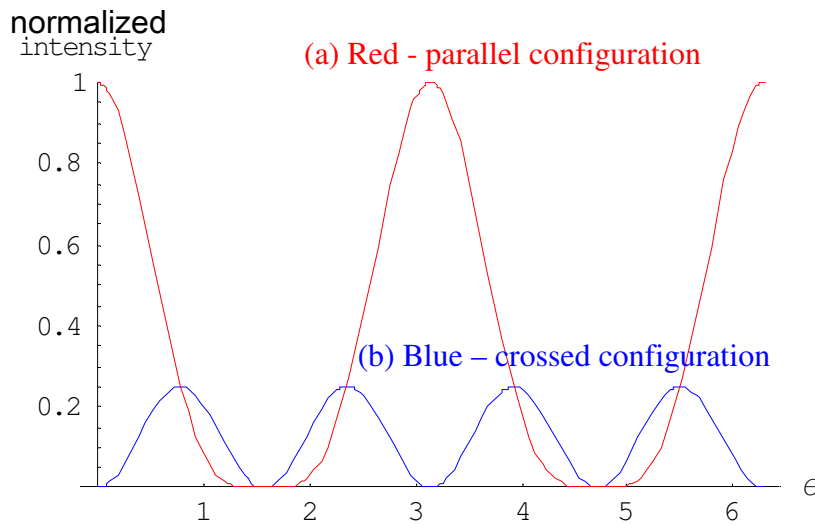


Figure 4.3 Normalized intensity (I / I_0) plot for the terahertz input. Red curve results when the terahertz source and P2 are cross-polarized to each other (configurations B and C in Fig. 4.2). Red curve results when they are parallel-polarized to each other (configurations A and D in Fig. 4.2).

4.2 Weak Response with X-polarization

The proposed detection principle in Chapters 1~2 suggests detection of X-pol. only. Therefore, configuration A in Fig. 4.2 was initially tried and the angle dependence of $(\cos\theta)^4$ was expected. However, a featureless response was obtained

from this configuration. As shown in Fig. 4.4, the detector response to the 4 μW terahertz source was not strong enough to overcome the thermal noise.

Although the causes of weak response are largely unknown, a few arguments can be made. First, the terahertz radiation changes only the electron temperature T_{el} significantly. Hence, the rate of change of the readout resistance γ could be smaller than what was estimated in Section 2.6. Second, when the detector was simulated with a full 3D electromagnetic simulator (HFSS) with X-pol., the result showed weak field enhancement at the active area (see Fig. 2.3). Also, the bare harmonic oscillator frequency ($\omega/2\pi \sim 3 \text{ THz}$ for $n_+ = 10^{17} \text{ cm}^{-3}$) of the sloshing mode is independent of electron density. The frequency of the sloshing mode is thus far above the 1 THz excitation frequency (which was not realized until long after the experiments were performed). These might be responsible for the weak response with X-polarized terahertz input.

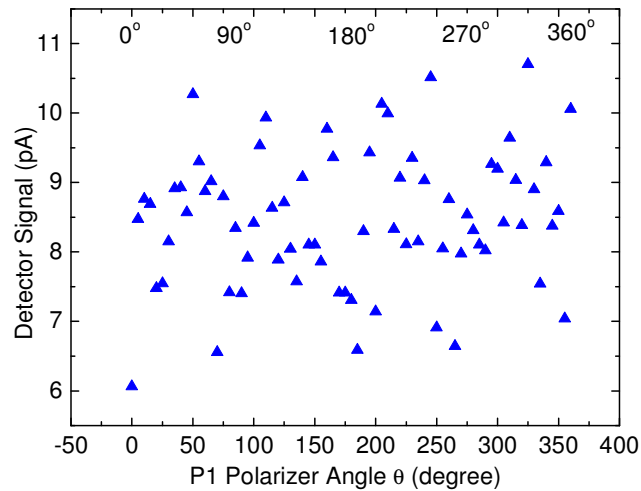


Figure 4.4 Detector response to X-polarized, 4 μW output of the VDI source, showing only the noise. Data measured with a current preamplifier (gain = 10^6 V/A) and a spectrum analyzer (reading in $V_{\text{rms}}/\text{Hz}^{1/2}$, ENBW = 1.95 Hz).

4.3 High Power Measurement

The signal was detectable with a more powerful terahertz source (Fig. 4.5).⁸ The output of UCSB free electron laser (FEL) is close to kW and has blown up several good samples. After attenuating the output down to a Watt, the detector operated in a stable manner, which suggests high threshold for the detectable terahertz power. The detector registered the shape of the FEL pulses on the scope with better sensitivity and speed when compared to those of the pyroelectric detectors available in the lab.

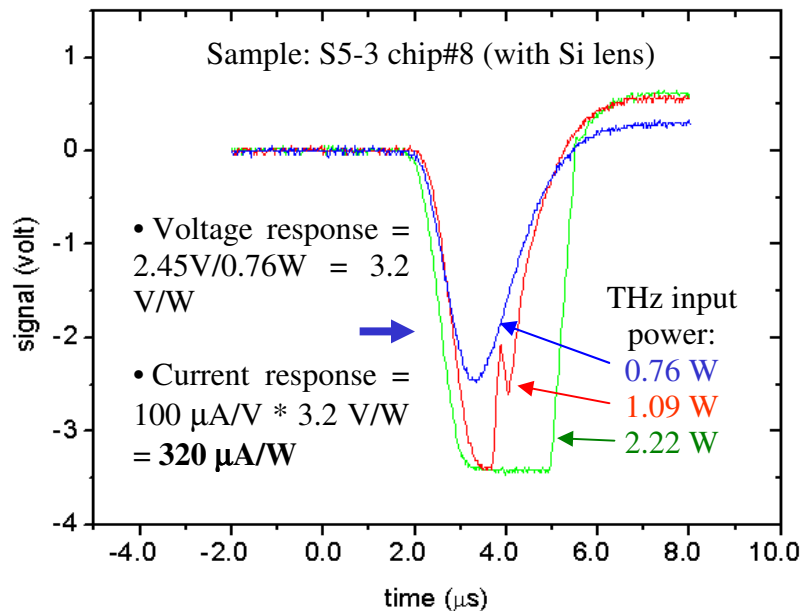


Figure 4.5 Single-shot detector responses to X-pol., 3 μs long, 1 THz pulses from the UCSB free electron laser (FEL). Output power was attenuated down to a Watt.

⁸ Thanks to Dan Allen for help with these measurements.

There were several strange observations with high power detection which could become subjects of further investigation. First, the response from this high-power detection regime is not *photoconductive* as suggested by the proposed detection theory in Chapters 1 ~ 2. There was response *without the readout bias voltages* on the readout channel; therefore it is a *photovoltaic* response. Second, when detector was rotated 90°, a response of a similar magnitude was observed. Third, the signal flipped the sign with a weak adjustment of the alignment, which suggests competition of multiple photovoltaic regions with opposite polarity of the signal. The number of such photovoltaic regions is at least two, however were not identified thoroughly. Some of these behaviors can be explained with the new detection theory later in this chapter. However, it must be done with caution due to the complexity of the system and possible non-linearity at high power.

4.4 Strong Photovoltaic Response with Y-Polarization

The detection configuration A in Fig. 4.2 can be switched easily to the configuration B by turning the polarizer P2 by 90°. The proposed detection mode suggests no or small *photoconductive* response with configuration B, since the antenna was not designed for the Y-pol. (see Chap. 1 ~ 2 or Ref. [43] for the

operation of the antenna system). However, surprisingly, a square-law, *photovoltaic* response with angle dependence of $(\cos\theta\sin\theta)^2$ was observed.

For the Y-pol., the antenna does not operate as an antenna. Instead, what receive the terahertz input are the “metal – 1 μm insulator gap – metal (MIM)” structures along the Y-direction. The MIM structures create electric fields on the two insulator gap regions as shown in Fig. 2.3(b). See also Fig. 4.6 for the cross-section of the FET part of the detector, along with the electric fields by the X-pol. and Y-pol terahertz inputs.

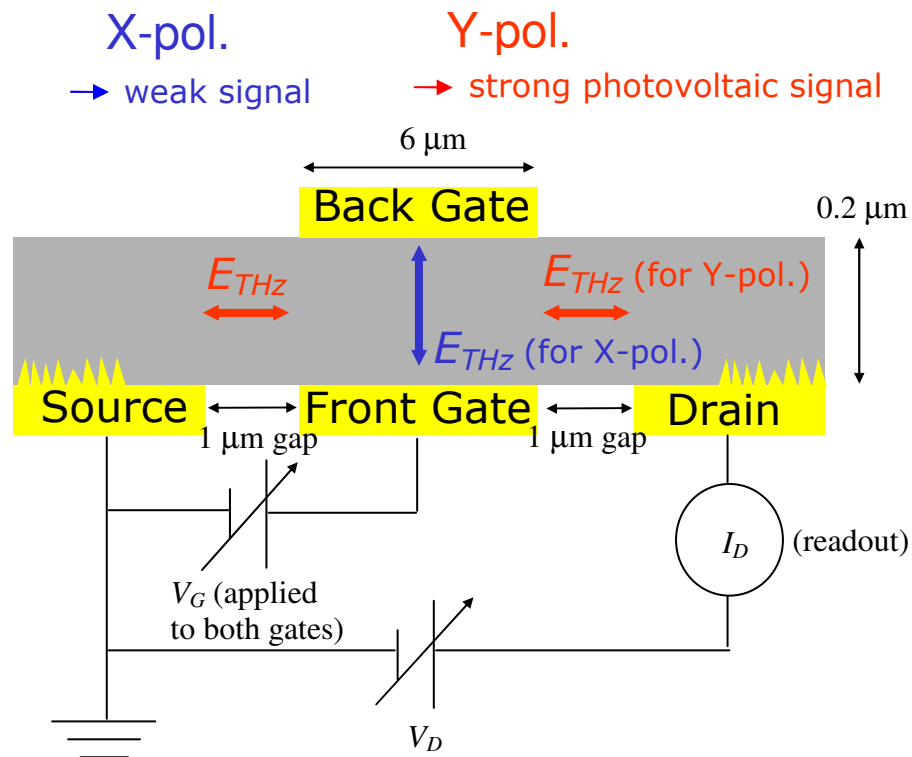


Figure 4.6 Cross-section of the FET part of the detector, with the electric fields induced by X-polarized (blue) and Y-polarized (red) terahertz input.

For the maximum signal strength with the Y-pol., the source polarization was switched to Y-pol. For this, the VDI source was physically turned by 90°, and the setup was re-aligned for peak signal. Then the configurations change from A / B to C / D. The observed detector responses for the configurations C and D are plotted in Fig. 4.7.

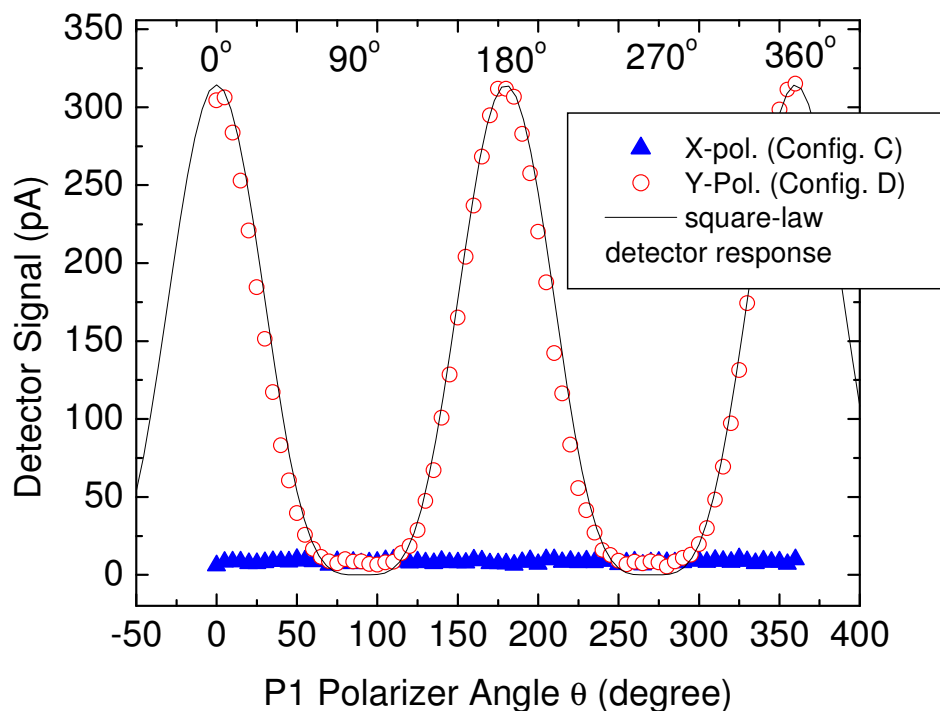


Figure 4.7 Detector measurement result with Y-polarization. Data measured with a current preamplifier (gain = 10^6 V/A) and a spectrum analyzer (reading in $V_{\text{rms}}/\text{Hz}^{1/2}$, ENBW = 1.95 Hz).

The $(\cos\theta)^4$ angle dependence of the configuration D was observed, whereas the $(\cos\theta\sin\theta)^2$ angle dependence of the configuration C was not observed due to the low responsivity to X-pol. Observations from all of the four detection configurations are summarized in Fig. 4.8.

	Configurations	Measured Polarization	Terahertz input intensity	Angle dependence of the measured signal
	A	X-pol.	$I_0 (\cos\theta)^4$	Below noise
	B	Y-pol.	$I_0 (\cos\theta \sin\theta)^2$	$(\cos\theta \sin\theta)^2$
	C	X-pol.	$I_0 (\cos\theta \sin\theta)^2$	Below noise
	D	Y-pol.	$I_0 (\cos\theta)^4$	$(\cos\theta)^4$

Figure 4.8 Summary of observations from different detection configurations.

The most puzzling observation was that the signal did not vanish at zero bias condition ($V_D = V_{SD} = 0$ V), which means the response is *photovoltaic*, rather than *photoconductive* as suggested from the bolometric response theory in Chapter 2. This requires a new theory for the operation of our device.

4.5 Measured Figures of Merit with Y-Polarization

The data shown in Fig. 4.7 were taken with a spectrum analyzer (Stanford Research, model SR760) with a post-detection bandwidth $BW = 1.95$ Hz. Terahertz input power $P_{in} = 4$ μ W has been assumed as supplied by VDI. The terahertz output was propagating through 60 cm-long path through the lab air and two wire grid polarizers. The water absorption and the insertion loss of the wire grid polarizers,

however, were not compensated for a conservative estimation. The data in Fig. 4.7 exhibits detector signal $I_{signal} = 314$ pA (maximum of the red open circles), noise $I_{noise} = 8.38$ pA (blue triangles), then a Signal to Noise Ratio (SNR) of 37.5 ($= I_{signal} / I_{noise}$). Responsivity (\mathfrak{R}) and Noise Equivalent Power (NEP) can be calculated from these measurements: $\mathfrak{R} = I_{signal} / P_{in} = 80$ $\mu\text{A}/\text{W}$, and $NEP = I_{noise} / (\mathfrak{R} * BW^{1/2}) = 80$ $\text{nW}/\text{Hz}^{1/2}$. From other measurements, and with an optimal bias condition, figures of merit as good as $SNR = 55.5$, $\mathfrak{R} = 80$ $\mu\text{A}/\text{W}$, $NEP = 50$ $\text{nW}/\text{Hz}^{1/2}$ have been obtained (see Fig. 5.32).

The response time is limited by the amplifier circuit, and has been estimated to be < 10 ns (on the order of nano-second) from a time series measurement with the oscilloscope trace (see Fig. 4.9).

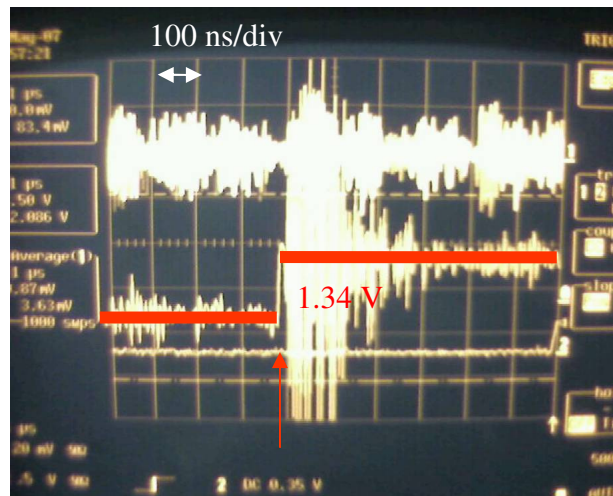


Figure 4.9 Response time measurement with 1 GHz scope and ~ 100 MHz bandwidth fast preamplifier. Trace is very noisy due to the admission of the noise across a wide bandwidth.

These figures of merit are better than those of the commercial pyroelectric detectors, but not as good as those of the state-of-the-art Schottky diode detectors. With these performance parameters, the detector can be paired with a compact microwatt level terahertz source and may perform useful applications, such as imaging and spectroscopy.

Fig. 4.10 and 4.11 shows an example of terahertz spectroscopy. The terahertz output of the VDI source is narrowband and tunable from 960 GHz to 1080 GHz. Spectra shown in Fig. 4.10 are taken with a bolometer as a reference.

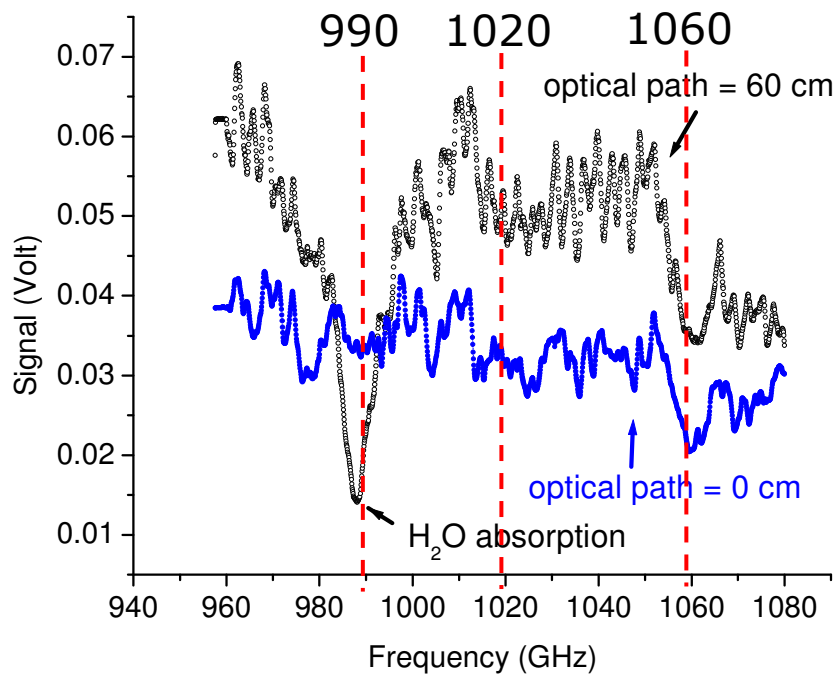


Figure 4.10 Reference detector (bolometer) measurements. Blue, filled circles are taken with an optical path = 0 cm (therefore no water absorption). Black, open circles are taken with an optical path = 60 cm and display water absorption lines at around 990, 1020, and 1060 GHz.

Trace shown as blue, filled circles is measured with the Bolometer right in front of the source, so it is the output spectrum of the terahertz source. Trace shown as black, open circles trace is measured with a 60 cm optical path between the terahertz source and the bolometer. Absorption peaks due to water vapor in the air at 990, 1020, and 1060 GHz can be seen. The same absorption lines can be observed with the detector in this work, as shown in Fig. 4.11. These absorption lines can be compared with the simulated plot shown in Fig. 4.12 [9].

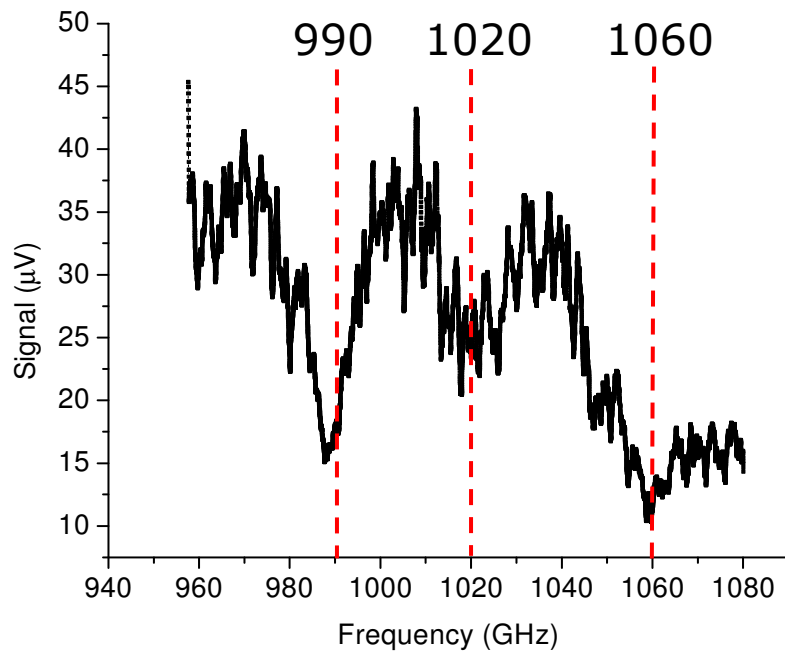


Figure 4.11 UCSB detector measurement with an optical path length of 60 cm. The spectrum also displays the water absorption lines at around 990, 1020, and 1060 GHz..

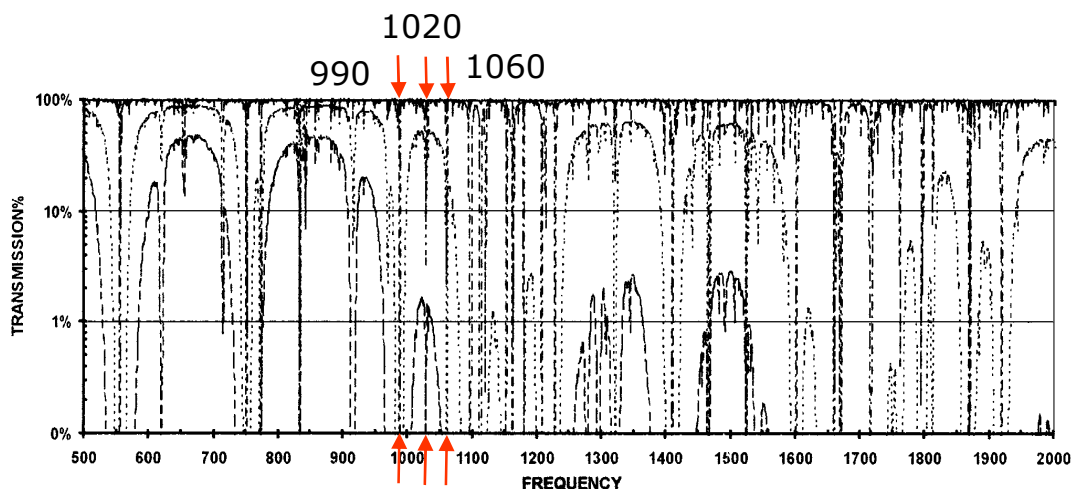


Figure 4.12 Simulated atmospheric transmission data from Ref. [9].

This spectroscopy example demonstrates that the detector in this work is indeed responding to terahertz radiation. Pyroelectric detectors, golay cells, and photon drag detectors would not be able to detect 4 μ W THz radiation modulated at 40 kHz. Only the state-of-the-art Schottky diode detectors would surpass the performance of the detector in this work.

The measured figures of merit in this work are very similar to those obtained from the plasma wave detectors reported by at least three different groups. As mentioned in Section 1.5, Tauk *et al.* reported $NEP \geq 10^{-10}$ W/Hz^{1/2} with silicon FETs at 0.7 THz and suggested the theory of two dimensional (2D) plasma waves for the detection mechanism [23]. U.R. Pfeiffer *et al.* also reported $NEP = 4 \times 10^{-10}$ W/Hz^{1/2} with silicon FETs at 0.6 THz and suggested self-mixing of terahertz

radiation with off-resonant 2D plasma waves (i.e., the theory of 2D plasma wave detection at off-resonant regime) for the detection mechanism [24-26]. Hartmut Roskos reported slightly worse NEP of about $3 \times 10^{-8} \text{ W/Hz}^{1/2}$ with GaAs FETs at 0.6 THz [27]. In comparison, this work reports $NEP = 5 \times 10^{-8} \text{ W/Hz}^{1/2}$ with GaAs FETs at 1 THz [30] and suggests *on-resonant three dimensional(3D) electron plasmon-assisted terahertz self-mixing* for the detection mechanism in the following Chapter 5.

Including this work, all four groups have detected terahertz radiation with field-effect-transistors and observed similar NEP and response time. These similar reports strongly suggest that all these observations might be based on the same phenomenon.

Chapter 5 Photovoltaic Detection Mode

The detector of this work was originally designed to generate *photoconductive* response for X-pol. but nothing for Y-pol. Therefore, small response with X-pol. (Sections 4.2 ~ 4.3) and large *photovoltaic* response with Y-pol. (Sections 4.4 ~ 4.5) were completely surprising. The possible reasons of the weak response with X-pol. were discussed at the end of Section 4.3. This chapter will investigate on the photovoltaic detection mode with Y-pol. Section 5.1 will introduce a new theory of “plasmon-assisted self-mixing” that explains the observed data in Sections 4.4 ~ 4.4). Section 5.1 will also present various data which supports the model. Sections 5.2 ~ 5.3 will discuss on other aspects of the detector such as noise and low temperature measurements. Furthermore, Section 5.4 will discuss on how this unexpected operation mode can be optimized for the best performance.

5.1 Theory of Plasmon-Assisted Self-Mixing

The concept of self-mixing is borrowed from U.R. Pfeiffer [25] and ultimately from “self controlled rectification of the RF signal” by H.-G. Krekels, *et al.*[24].

The concept of bulk (3D) plasmon is not borrowed from the 2D plasma wave theory of M.S. Shur Group [23, 57, 58]. Rather, it comes directly from considering the microscopic carrier dynamics in the field-effect-transistor. The theory developed in this work is comparable to a recent paper by Lisauskas *et al.* on the self-mixing theory with off-resonant 2D plasma waves [26]. Ref [26] is a follow-up paper of Ref [25], and was published while I was writing this dissertation. In my dissertation work, I introduce a microscopic description of the excited electrons (3D plasmons) while adopting the self-mixing theory of [26]. As a result, a simple and intuitive analytical model is derived.

5.1.1 Enhanced E-fields due to the Metal-Insulator-Metal (MIM) Structure

The device structure of this work is shown in Fig. 5.1, along with the two plasmon excitation regions (marked by E-fields) and four density modulation regions (marked by letters A, B, C, D, and dotted ellipses).

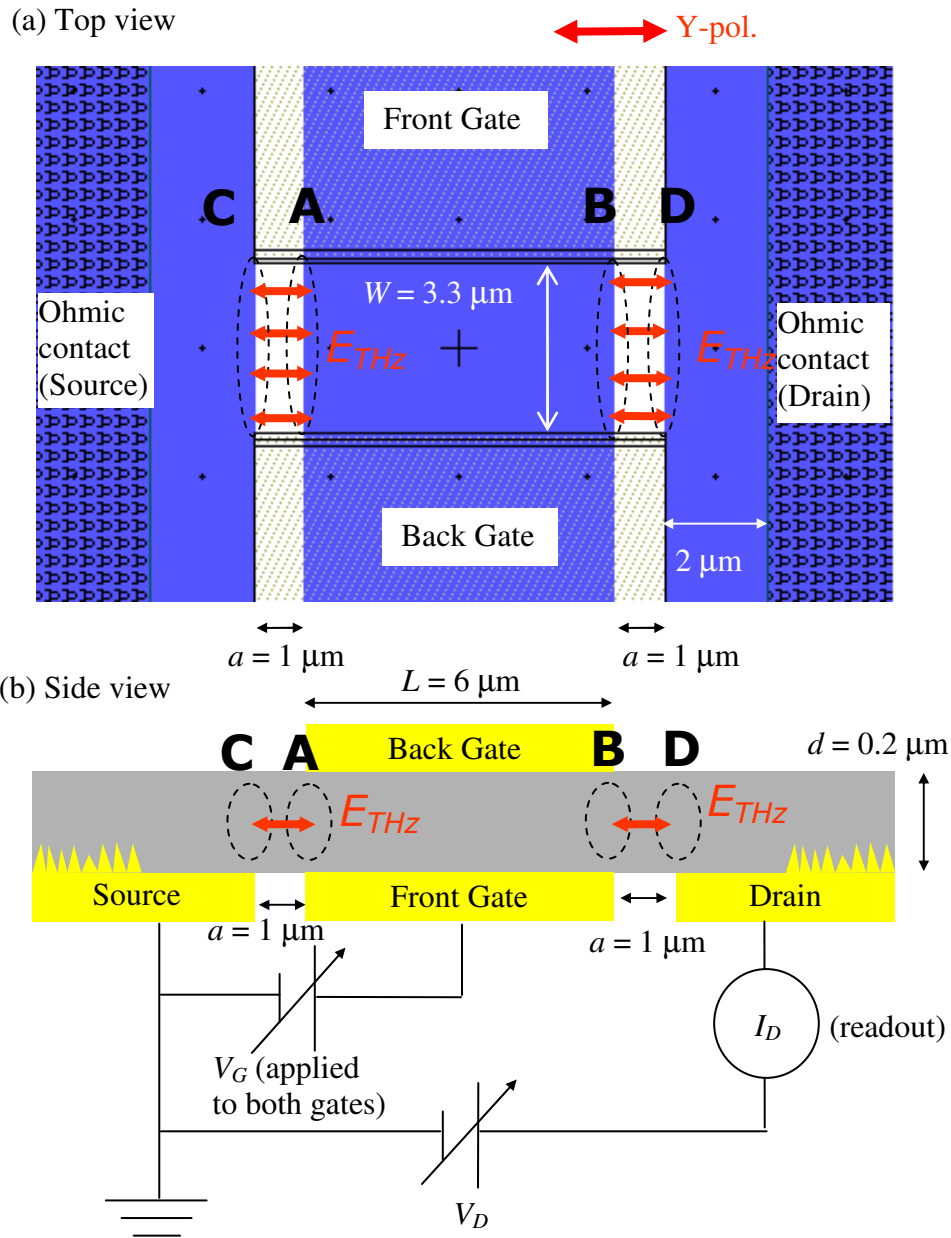


Figure 5.1 Top view (a) and Side view (b) of the FET part of the detector with Y-pol. Terahertz input. The two plasmon excitation regions are defined by the enhanced E-Fields on the two gaps ($a = 1 \mu\text{m}$). The four density modulation regions are marked with dashed circles and letters (A, B, C, and D).

The two plasmon excitation regions are defined by the enhanced E-fields on the two metal-insulator-metal (MIM) gaps. As shown in Fig. 2.3 (b), Y-polarized (Y-pol.) terahertz input can form enhanced electric fields at the two MIM gap regions. See Fig. 5.2 for the directions of the induced E-fields. The E-fields are perpendicular to the MBE growth direction (z-direction), and can drive the electrons (= excite electron plasmons) along the source-drain direction (y-direction). On the other hand, these electric fields would not excite the intersubband transitions of the double quantum wells in TACIT detectors, since the transitions have oscillator strength in the MBE growth direction only [17, 18].

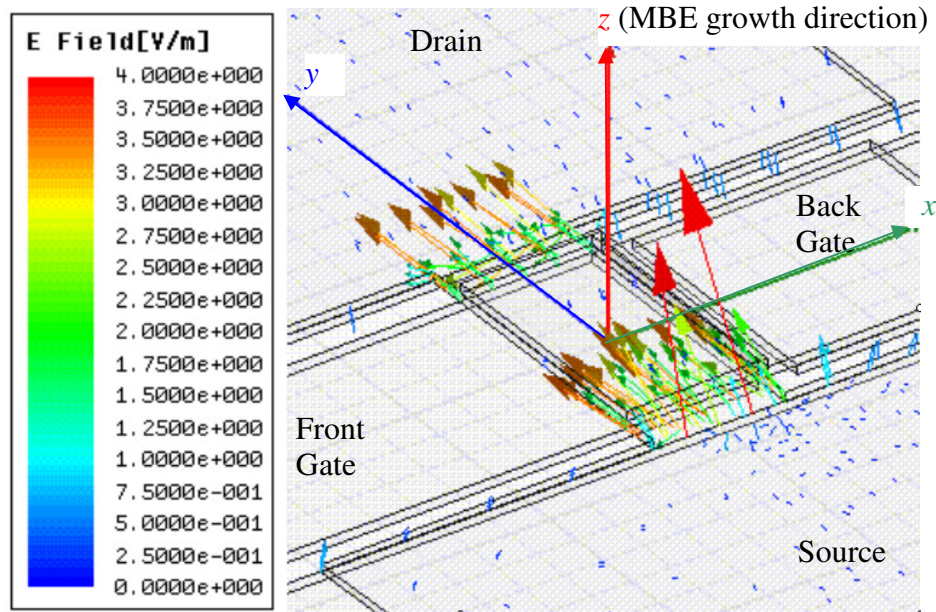


Figure 5.2 Electric field vectors induced by Y-pol. terahertz input. A Gaussian input beam with $E_0 = 1$ V/m, beam waist radius = $50 \mu\text{m}$ (incident cone half angle = 30° implied) was used.

The voltage formed on the gap by the terahertz electric field E_{THz} is given by:

$$V_{THz} = a * E_{THz} \quad (5.1.1.1)$$

, where $a = 1 \mu\text{m}$ is the gap size.

The voltage V_{THz} is driving electrons along the source-drain channel (y-direction), and also *simultaneously* modulates the electron density in the channel via field-effect of the metal-semiconductor Schottky junctions, at the four regions (A~D in Fig. 5.1): The high-density and highly mobile electrons in metals can be driven to the edge of the metal gates, and form surplus of negative (or positive) charges there. Therefore the edges of the gates are under an equivalent positive (or negative) bias voltage V_{THz} . Then, V_{THz} modulates the electron density in n-GaAs near the metal edges.

The diffusion time of electrons over the changed depletion length can be estimated as follows:

$$l_d / v_{th} \quad (5.1.1.2)$$

, where l_d and v_{th} are respectively the change of depletion length by V_{THz} and the thermal velocity of electrons.

l_d is assumed to be $10 \text{ nm} = 10^{-6} \text{ cm}$. v_{th} can be obtained from the average kinetic energy of an ideal gas particle in thermal equilibrium with a heat bath at temperature $T = 300 \text{ K}$:

$$\frac{1}{2} m * v_{th}^2 = \frac{3}{2} k_B T, \quad (5.1.1.3)$$

Therefore,

$$v_{th} \sim \sqrt{3k_B T / m^*} \sim 4.5 \times 10^7 \text{ cm/s.} \quad (5.1.1.4)$$

Then eq. (5.1.1.2) gives

$$l_d / v_{th} \sim \frac{10^{-6} \text{ cm}}{4.5 \times 10^7 \text{ cm/s}} \sim 20 \text{ fs.} \quad (5.1.1.5)$$

Therefore, the channel charge density can be modulated in response to terahertz radiation.

Also, due to the inhomogeneity of the driving terahertz E-fields and the electron distributions, the resonant frequency of absorption is the bulk plasmon frequency ω_p (See Section 1.6.1).

In summary, bulk electron plasmons are being excited by the terahertz E-fields in the source-to-drain direction. The induced AC-currents are being modulated (via the modulation of channel charge density) coherently by the same terahertz E-fields. In this context, the name “plasmon-assisted self-mixing” for the new detection mechanism should be appropriate.

5.1.2 Qualitative, Simplified Model

In this section, the new detection model is approached largely qualitatively. For the simplicity of the argument, regions A and B in Fig. 5.1 are discussed first. Regions C and D in Fig. 5.1 will be discussed as additional effects. In addition, the channel center approximation of Section 1.6.1 will be assumed initially, and more rigorous modeling will be presented later.

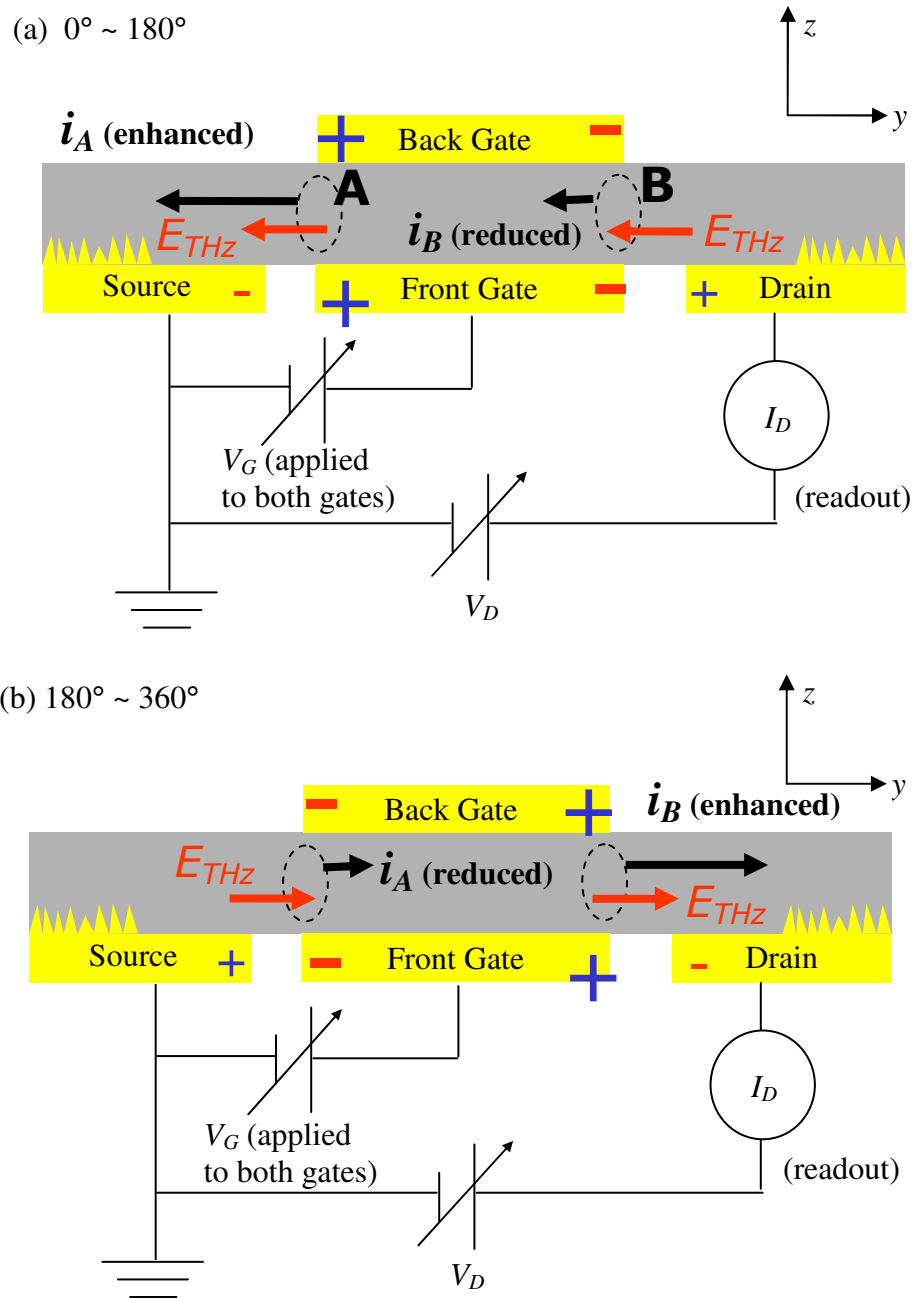


Figure 5.3 Induced instantaneous currents for (a) the first half-cycle and (b) the second half-cycle of terahertz oscillations. The polarity of the effective bias voltages due to the terahertz input are marked as blue + or red - signs.

Fig. 5.3 (a) shows the cross-section of the device during the first half-cycle of the terahertz oscillations. As E-fields are in $-y$ direction (coordinates are shown in the Figures), the voltage V_{THz} (eq. (5.1.1.1)) formed on the gap regions A and B drives instantaneous currents i_A and i_B , respectively, in $-y$ direction.

As discussed in Section 1.6.1, the same E-fields modulate the electron densities n_A and n_B in the space-charge regions A and B (terahertz self-mixing), respectively. The polarity of the effective gate voltage V_{THz} over the region A is positive. Since n_A is a monotonically increasing function of V_G (see Fig. 1.8), the current flow (i_A) in $-y$ direction is amplified. On the other hand, the polarity of the effective gate voltage V_{THz} over the region B is negative, i_B in $-y$ direction for region B is reduced.

For the next half-cycle, as shown in Fig. 5.3 (b), the E-fields and the induced currents are in $+y$ direction. This time, i_A in $+y$ direction is reduced, whereas i_B in $+y$ direction is enhanced.

As a result, the time-averaged net currents are DC, rectified photovoltaic currents I_A and I_B in opposite directions, as shown in Fig. 5.4.

The regions C and D in Fig. 5.1 also generate photovoltaic currents I_C and I_D ; these currents counter I_A and I_B , respectively. However, regions C and D have ohmic contacts nearby, so the effective voltage is smaller than the voltages formed on regions A and B. Also, regions C and D have only one Schottky junction for each, whereas A and D have two (double gates) for each. Therefore, lower efficiencies for the terahertz self-mixing at those regions are expected. That is, I_A

and I_C (or I_B and I_D) do not cancel each other, although they oppose each other and have the same bias dependences:

$$I_A - I_C > 0, \text{ and} \quad (5.1.2.1)$$

$$I_B - I_D > 0. \quad (5.1.2.2)$$

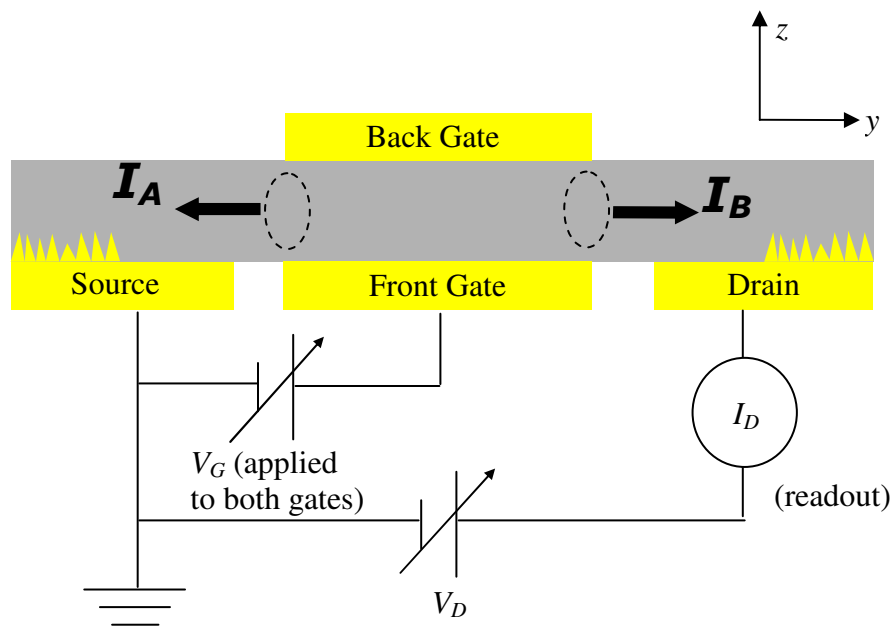


Figure 5.4 The net result of the terahertz self-mixing is rectified DC photovoltaic currents in opposite directions from regions A and B. (time average of Fig. 5.3 (a) and (b))

In addition to the terahertz self-mixing that was just discussed, electron plasma resonance is involved in the signal generation process. The electron mobility, therefore the generated signal at each region can be resonantly enhanced by the plasmons (resonant excitation of collective motion of electrons).

An electron density (n) relates to a plasma resonance frequency:

$$f_p = \frac{1}{2\pi} \sqrt{\frac{ne^2}{m^* \epsilon}} \quad (5.1.2.3)$$

, where e is the charge of an electron, m^* is the effective mass of an electron in GaAs, and ϵ is the dielectric constant of GaAs.

Since n is voltage-tunable (see Fig. 1.9 (a)), at a fixed radiation frequency f_p , n can be swept through plasma resonance, for example, with V_G (see Fig. 1.9 (b)). Since there are two tunable bias voltages (V_G , V_D), a false-color, two-dimensional (2D) plot of the detector response is obtained at a fixed frequency (see Fig. 5.5 for an example of 1 THz). Plasma resonance will appear as a line peak (for example, $V_G = \text{constant}$) in the 2D false-color plot.

The electron densities (n_A , n_B , n_C , and n_D) tune with bias voltages (V_G and V_D).

$$n_A = n_A(V_G) \text{ is a function of } V_G \text{ only,} \quad (5.1.2.4)$$

$$n_B = n_B(V_G, V_D) = n_B(V_G - V_D) \text{ is a function of } V_G \text{ and } V_D, \quad (5.1.2.5)$$

$$n_C = n_C(V_G) \text{ is a function of } V_G \text{ only,} \quad (5.1.2.6)$$

$$n_D = n_D(V_G, V_D) = n_D(V_G - V_D) \text{ is a function of } V_G \text{ and } V_D. \quad (5.1.2.7)$$

In (5.1.2.5) and (5.1.2.7), it is assumed that the voltage dependency reduces to an effective voltage $V_G - V_D$, the voltage difference between the drain and the gates. Due to these voltage dependences, the plasma resonance of the electrons in regions A and C ($I_A - I_C$) appears as a horizontal line peak ($V_G = \text{constant}$), whereas the resonance of the electrons in regions B and D ($I_B - I_D$) appears as a diagonal line peak ($V_G - V_D = \text{const.}$) in the 2D false-color plot (see Fig. 5.5 for an example).

5.1.3 Experimental Data Support the Qualitative

Model

Fig. 5.5 shows measured detector responses to $4 \mu\text{W}$, 1 THz radiation, recorded in 2D false color plot versus V_D for the horizontal-axis and V_G for the vertical axis. With the theoretical framework of the simplified model in Section 5.1.2, the experimental data in Fig. 5.5 can be interpreted successfully:

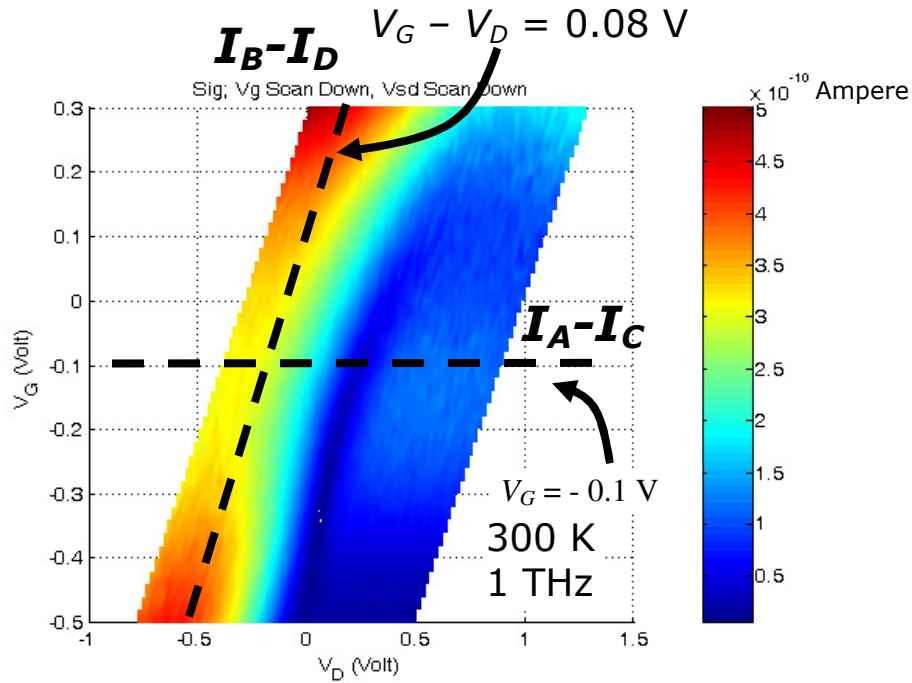


Figure 5.5 (Experimental) detector responses to $4 \mu\text{W}$, 1 THz radiation. The photovoltaic current signal was converted to a voltage signal by a current preamplifier with a gain of $1 \mu\text{A/V}$ and was recorded in a false-color scale. A voltage signal of 10^{-4} Volt is equal to a current signal of 10^{-10} Ampere.

First, the rectified, photovoltaic current signals from each region can be seen as two distinct resonance lines. As discussed in Section 5.1.2, $I_A - I_C$ is responsible for the $V_G = 0.08$ Volt resonance, whereas $I_B - I_D$ is responsible for the $V_G - V_D = -0.1$ Volt resonance. $I_A - I_C$ and $I_B - I_D$ are in opposite directions from each other. Therefore, the two resonance lines cancel each other at their common resonance condition (where the dashed lines meet in Fig. 5.5). On the lock-in amplifier, a 180° phase difference across the two resonances is observed. Also, quenching and sharp turnarounds of the responsivity across the two resonances are observed (see Fig. 5.15).

Second, interestingly, the diagonal peak seems to be stronger than the other, horizontal peak. That is,

$$I_B - I_D \text{ (function of } V_G \text{ and } V_D, \text{ diagonal)} > I_A - I_C \text{ (function of } V_G \text{ only, horizontal)} \quad (5.1.3.1)$$

This can be attributed to a built-in asymmetry made during the cleanroom fabrication, and the alignment of the terahertz input beam during the measurement. The fabrication-related asymmetry refers to the misalignment of the back gate lithography layer, relative to the front gate lithography layer. Due to this built-in asymmetry, one of the two MIM gaps is expected to generate the response signal more efficiently. This does not contradict the observed behavior during the spatial alignment with the terahertz input beam. Only one peak during the alignment is observed, even though the terahertz beam can be made to illuminate each gap more efficiently than the other. By peaking up the signal during the alignment with $V_D =$

0, the difference of the two gap is maximized. When a detector is tested, the electrode close to the weaker gap is selected to be the source (grounded), whereas the other electrode close to the stronger gap is selected to be the drain. If the source / drain electrodes are exchanged, the strength of the peaks follows exchanged (Fig. 5.6). The selection is by chance, and the former configuration is preferred. If data with the latter configuration are obtained, the experiment was done again with the source / drain electrode exchanged to get the preferred data format with the former configuration.

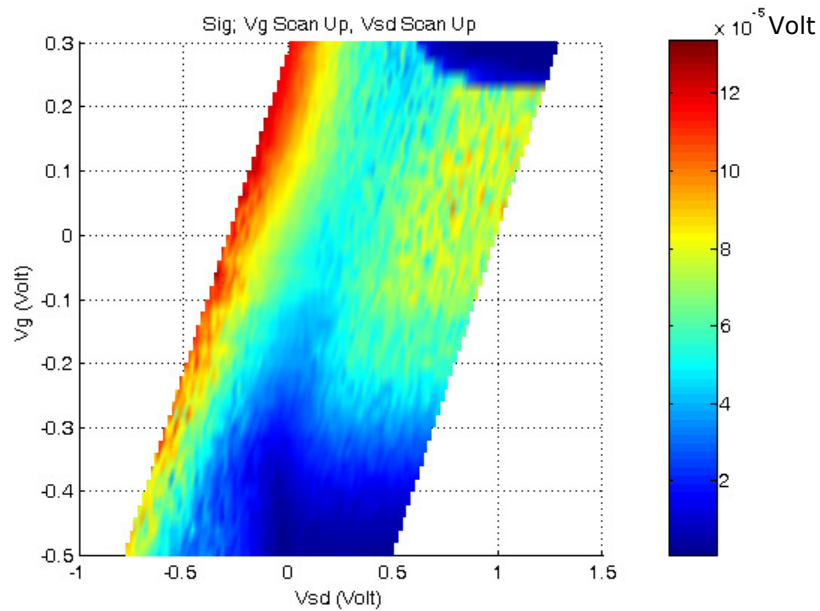


Figure 5.6 (Experimental) detector signal to $4 \mu\text{W}$, 1 THz radiation, with source/drain exchanged. The photovoltaic current signal was converted to a voltage signal by a current preamplifier with a gain of $1 \mu\text{A/V}$ and was recorded in a false-color scale. A voltage signal of 10^{-4} Volt is equal to a current signal of 10^{-10} Ampere.

5.1.4 Frequency Dependence of the Plasma

Resonance

Luckily, within the UCSB campus, three more radiation sources were available at 140, 240, and 600 GHz with output powers of 0.5, 30, and 20 mW, respectively⁹.

If the resonance peaks are indeed due to the bulk electron plasmons, the peak positions in voltage must shift once the incident terahertz frequency is changed. That is, the plasma frequency and electron density are related by:

$$f_p = \frac{1}{2\pi} \sqrt{\frac{ne^2}{m^* \epsilon}} . \quad (5.1.4.1)$$

According to this relation, lower radiation frequency (f_p) requires lower electron density (n) for the resonance. In an enhanced-mode n-type field-effect-transistor as in this work, more negative gate voltage or more positive drain voltage results in a reduced electron density. Therefore, eq.(5.1.4.1) predicts the diagonal resonance peak to move to the right (or downward) and the horizontal resonance peak to move downward.

⁹ 140 GHz source - Professor S. James Allen Group, 240 GHz source - Professor Mark Sherwin Group, 600 GHz source - Professor Elliot R. Brown Group

Fig. 5.7 ~ 5.9 are the data from 600, 240, and 140 GHz, respectively, demonstrating the expected shift of the resonance peaks and therefore, suggesting the resonant excitation of the bulk electron plasmons. Note that responsivities from Fig. 5.5 ~ 5.9 cannot be compared with each other, because the power coupling of Fig. 5.8 ~ 5.9 are not known. The radiation sources at 240 GHz and 140 GHz were very powerful so Fig. 5.8 ~ 5.9 were measured without collecting the radiations into the detector with parabolic mirrors as in Fig. 5.5 ~ 5.7. Note that these data were used only to demonstrate the excitation of bulk electron in our detector via comparison with 1DPoisson simulation and eq. (5.1.4.1).

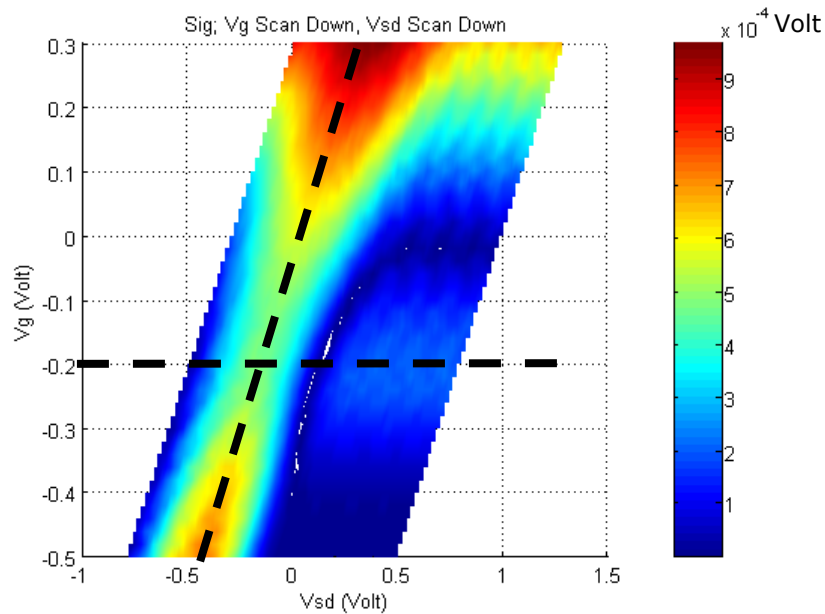


Figure 5.7 (Experimental) detector signal to 0.5 mW, 0.6 THz radiation. Incident power is not calibrated.

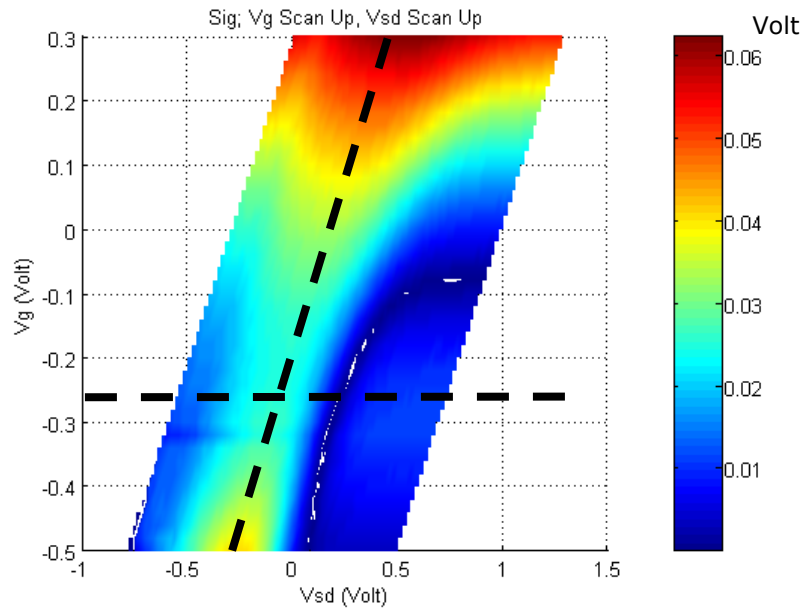


Fig. 5.8 (Experimental) detector signal to 30 mW, 0.24 THz radiation. Incident power is not calibrated.

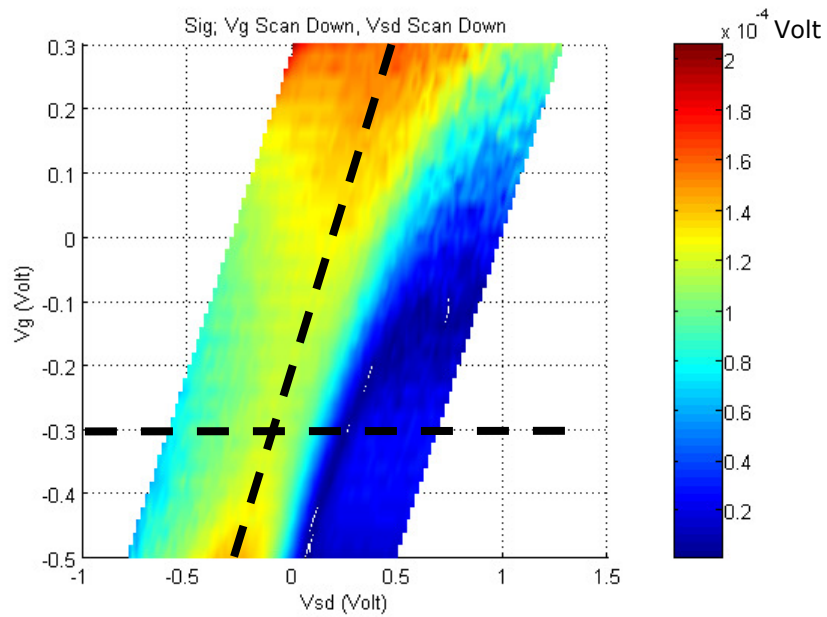


Figure 5.9 (Experimental) detector signal to 20 mW, 0.14 THz radiation. Incident power is not calibrated.

5.1.5 Analytic, Simplified Model

Following the qualitative model, an analytic model is developed. A cross-section of the device is shown in Fig. 5.10.

A current density at the x-z plane of the region A is given by:

$$j = j_A = -e \cdot n \cdot v \quad (5.1.5.1)$$

, where $n = n_A$ is the electron density, e is the charge of an electron, and v is the drift velocity of the electrons. n is given by the 1D-Poisson simulation of the nearly parabolic potential well structure. v is given by the equation of motion for the electron. The current density is integrated over the x-z plane cross-section and time averaged in order to calculate the observable DC photovoltaic current.

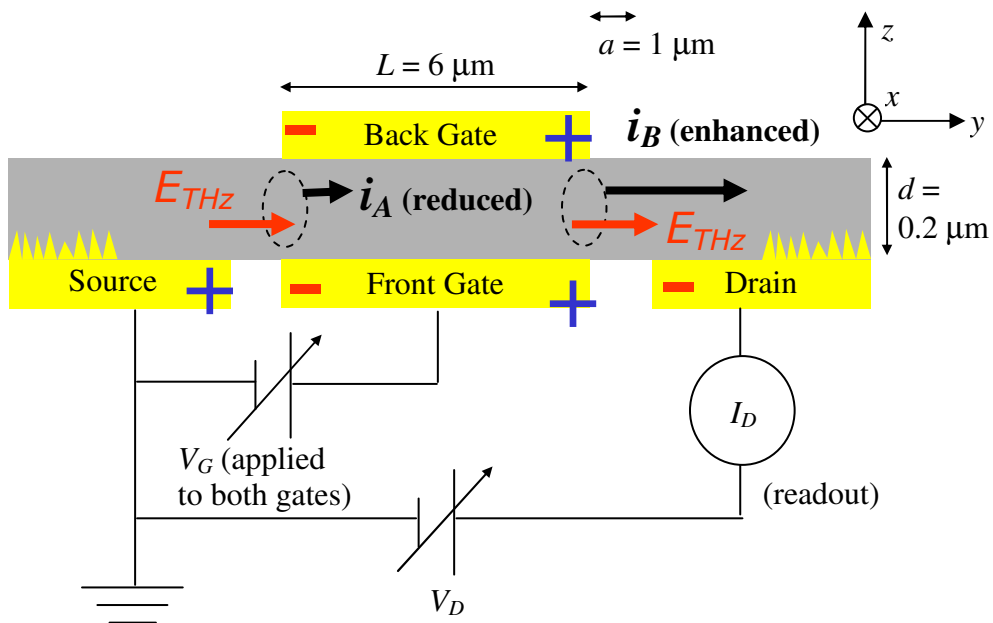


Figure 5.10 Cross-section of the FET part of the detector.

The electron density could be ideally acquired from a 3D Poisson simulator including carrier flow and high field effects due to the multi-valley band structure. However, in this section, channel center approximation in Section 1.6.1 with the 1D-Poisson simulation results will be used and high field effect will be neglected. In addition, for an analytic treatment, the voltage dependent electron density in Fig. 1.9 (a) is approximated to an analytic function composed of an error function Erf (V_G) and proper scaling factors (see Fig. 5.11 for a plot).:

$$n = n_0 \cdot Erf(V_G) + n_l \quad (5.1.5.2)$$

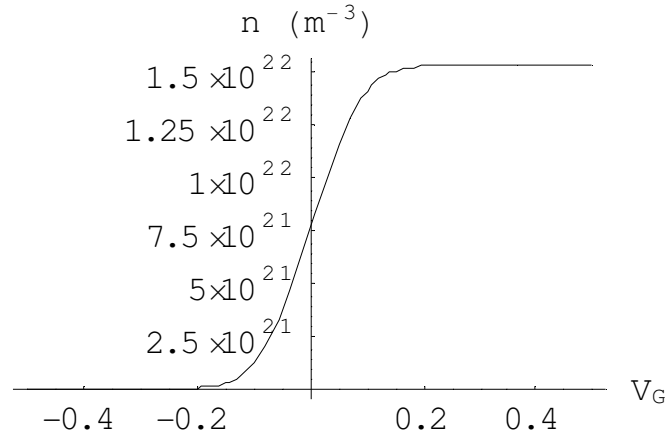


Figure 5.11 Electron density (n) vs. gate voltage (V_G). This is a rough, analytic approximation to the one-dimensional Poisson calculation results. Compare this plot with Fig. 1.9 (a).

Due to the self-mixing, the electron density varies with the terahertz radiation, and can be expressed as:

$$n(t) = n_{DC} + \frac{dn}{dV_G} aE_{THz} e^{j\omega t} \quad (5.1.5.3)$$

, where n_{DC} is the time-independent electron density due to the DC gate bias voltage V_G , ω is the terahertz angular frequency, $a = 1 \mu\text{m}$ is the MIM gap size and E_{THz} is the electric field at the gap.

The density modulation (dn/dV) is calculated from the analytic form of the electron density n in Fig. 5.11, and shown in Fig. 5.12.

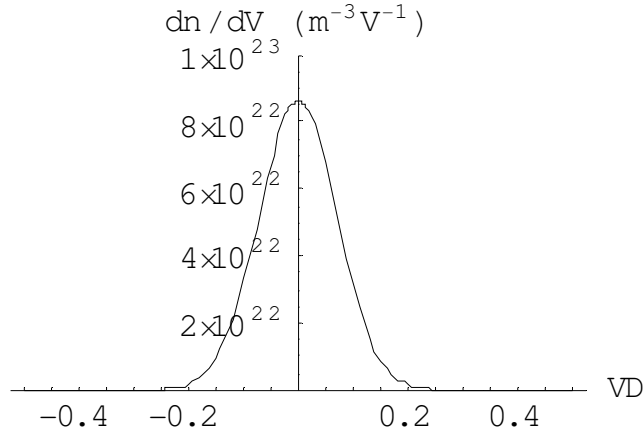


Figure 5.12 Electron density modulation (dn/dV) vs. gate voltage, or the self-mixing envelope.

The self-mixing process exploits the (dn/dV) curve for signal rectification. The dn/dV curve provides an “envelope” to the resulting signal in eq. (5.1.5.15) and Fig. 5.14.

Then the electron plasmon resonantly enhances this rectification process. The oscillating electrons in the plasma satisfy the equation of motion:

$$\ddot{x} + \Gamma\dot{x} + \omega_p^2 x = -\frac{eE_{THz}}{m^*} e^{j\omega t} \quad (5.1.5.4)$$

, where $\omega_p = 2\pi f_p$ is the angular plasma resonance frequency.

Solving the equation for the displacement $x(t)$,

$$x(t) = \frac{-e/m^*}{\omega_p^2 - \omega^2 + j\Gamma\omega} E_{THz} e^{j\omega t} \quad (5.1.5.5)$$

is obtained, and with differentiation, the electron drift velocity is obtained:

$$v(t) = \frac{dx}{dt}(t) = \frac{-j\omega e/m^*}{\omega_p^2 - \omega^2 + j\Gamma\omega} E_{THz} e^{j\omega t} \quad (5.1.5.6)$$

, where Γ is the energy relaxation time. Assuming low field,

$$v(t) = -\mu E_{THz} e^{j\omega t} \quad (5.1.5.7)$$

, where μ is the electron mobility given by

$$\mu = \frac{j\omega e/m^*}{\omega_p^2 - \omega^2 + j\Gamma\omega}. \quad (5.1.5.8)$$

The real parts of the electron mobilities for the frequencies of 0.14, 0.24, 0.6, and 1 THz are plotted in Fig. 5.13.

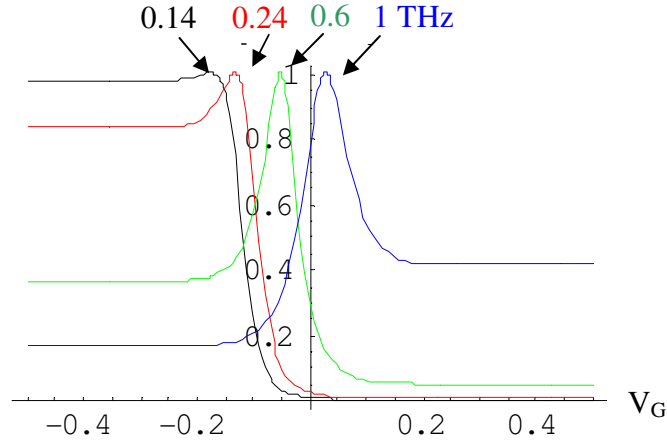


Figure 5.13 Real parts of the electron mobility vs. V_G (m^2/Vs). Resonances are due to the electron plasmons.

The current density eq.(5.1.5.1) can be derived by multiplying eq.(5.1.5.3) and eq.(5.1.5.7). Only the real parts of each quantity should be taken for multiplication, since only the real parts of each have physical meanings (see p.264 of Ref. [39]). Therefore, the current density is given by:

$$\begin{aligned}
j(t) &= -e \cdot \text{Re}(n) \cdot \text{Re}(v) \\
&= -e \times \left(n_{DC} + \frac{dn}{dV} a E_{THz} \cos \omega t \right) \\
&\quad \times (v_{DC} - \text{Re}(\mu) E_{THz} \cos \omega t + \text{Im}(\mu) E_{THz} \sin \omega t) \\
&= -e n_{DC} v_{DC} + e \text{Re}(\mu) \frac{dn}{dV} a E_{THz}^2 \cos^2 \omega t \\
&\quad - e \text{Im}(\mu) \frac{dn}{dV} a E_{THz}^2 \sin \omega t \cos \omega t \\
&\quad + e n_{DC} \text{Re}(\mu) E_{THz} \cos \omega t - e n_{DC} \text{Im}(\mu) E_{THz} \sin \omega t \\
&\quad + e \frac{dn}{dV} a v_{DC} E_{THz} \sin \omega t \cos \omega t
\end{aligned} \tag{5.1.5.9}$$

By integrating the current density over the x-z plane cross-section, the instantaneous current is obtained.

$$i(t) = \left(\int_z j(t) dz \right) \cdot W \tag{5.1.5.10}$$

, where W is the width of the channel. With the channel center approximation, eq.(5.1.5.10) reduces to

$$i(t) = j(t) \cdot W \delta \tag{5.1.5.11}$$

, where δ is the effective thickness of the electron plasmon.

After time averaging, two DC terms remain.

$$\begin{aligned}
I = \langle i(t) \rangle &= -en_{DC}v_{DC}W\delta + e \operatorname{Re}(\mu) \frac{dn}{dV} aE_{THz}^2 \frac{1}{2} W\delta \\
&= I_{DC} + \frac{e}{\varepsilon} \operatorname{Re}(\mu) \frac{dn}{dV} \left(\frac{1}{2} \varepsilon E_{THz}^2 \right) \cdot (aW\delta)
\end{aligned} \tag{5.1.5.12}$$

The first term in eq.(5.1.5.12),

$$I_{DC} = -en_{DC}v_{DC}W\delta \tag{5.1.5.13}$$

is the current which is responsible for all features in DC IV curves (I_D saturation, gate modulation) as shown in Fig. 2.17. The second term is the detector response to the terahertz input, the rectified, photovoltaic current signal. The terms on the parentheses can be recognized as part of the terahertz power coupled into a gap region (energy density times the volume of the excitation region times the energy relaxation rate):

$$\left(\frac{1}{2} \varepsilon E_{THz}^2 \right) \cdot (aWd) \cdot \Gamma = \alpha P_{in} \tag{5.1.5.14}$$

, where α is the power coupling efficiency and d is the distance between the gates.

The rectified, photovoltaic current signal can be written as:

$$I_{signal} = \frac{e}{\varepsilon} \operatorname{Re}(\mu) \frac{dn}{dV} \alpha P_{in} \frac{\delta}{\Gamma \cdot d} . \tag{5.1.5.15}$$

The current responsivity can be written as

$$\mathfrak{R} = \frac{I_{signal}}{P_{in}} = \alpha \frac{e}{\varepsilon} \operatorname{Re}(\mu) \frac{dn}{dV} \frac{\delta}{\Gamma \cdot d} . \tag{5.1.5.16}$$

Therefore, the detector performance can be improved by raising the coupling efficiency (α), tuning the plasmon on-resonance for the greatest mobility ($Re(\mu)$), and increasing the density modulation (dn/dV) of the Schottky junction.

Fig. 5.14 is the resulting plot of the current responsivity with 100% power coupling efficiency ($\alpha = 1$). With a realistic power coupling efficiency of 1 ~ 10 %, the theoretical responsivity is on the order of 0.01 ~ 1 A/W, which is better by 2 ~ 4 orders of magnitude than the best observed responsivity of 80 μ A/W.

As can be noticed, the signal in Fig. 5.14 is a product of Fig. 5.12 and 5.13, the electron density modulation peak (or the self-mixing envelope) and electron mobility peak (or the electron plasma resonance), respectively. Therefore, lining up those two peaks will maximize the detector response.

The theoretical responsivity plots in Fig. 5.14 can be compared with the experimental responsivity data. Fig. 5.15 shows the data cross-sections along $V_D = +0.5$ Volt-line of the Fig. 5.5, 5.7, 5.8, and 5.9. The analytical model and the experimental data are in good agreement with each other.

The data in Fig. 5.15 were fit to two canceling Gaussian peaks in order to quantify the peak positions, and were compared with the 1D-Poisson results shown in Fig. 1.9 (a). Fig. 5.16 shows the comparison.

Note that the responsivities at 240 and 140 GHz are not calibrated. These data were used only to demonstrate the excitation of bulk plasmons in our detector via comparison with 1DPoisson simulation and eq. (5.1.4.1). The work done in this

section leaves the door open for analytical forms of the device impedance and the power coupling efficiency.

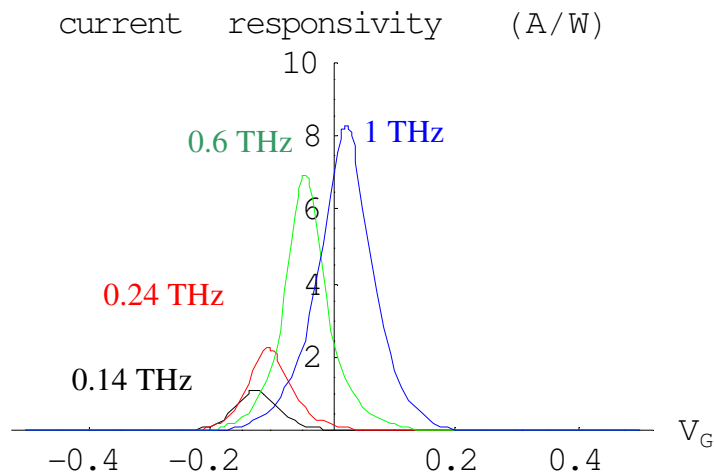


Figure 5.14 Analytic current responsivity vs. V_G .

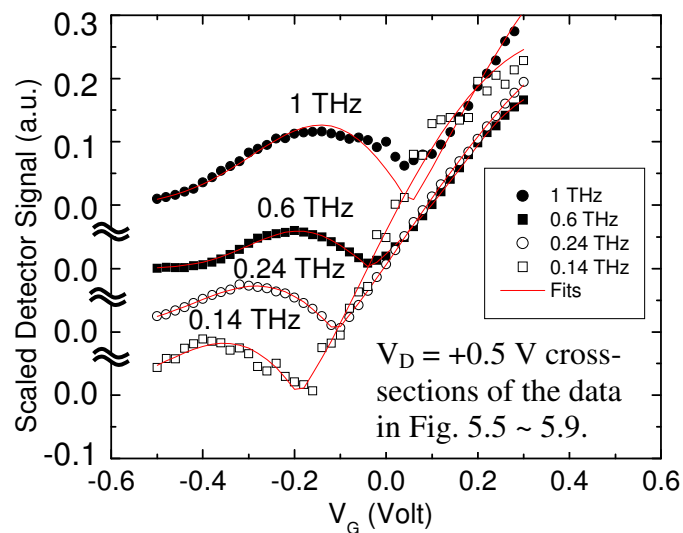


Figure 5.15 Detector data cross-sections at $V_D = +0.5$ Volt of the data in Fig. 5.5, 5.7 ~ 5.9. with appropriate scaling and vertical shifts. Data were fit to two canceling Gaussians.

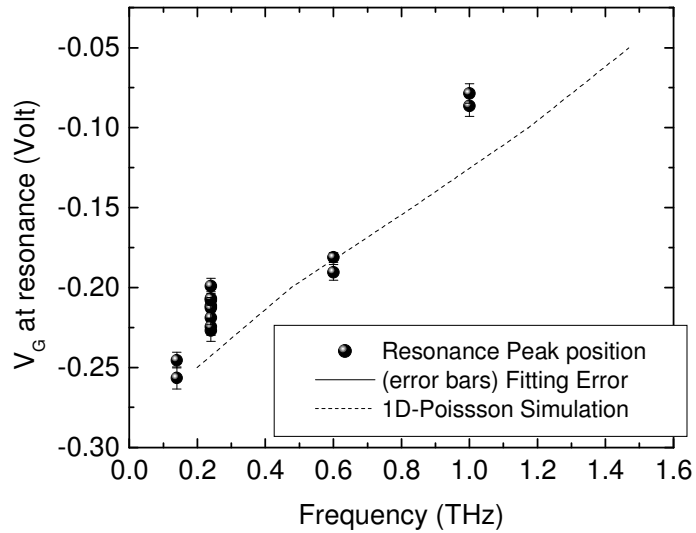


Figure 5.16 The positions of the peaks related to the excitation region A is plotted versus terahertz frequency. Dotted line is not a fit but a 1D-Poisson simulation results. The increasing trend is in good agreement.

5.1.6 Model without the Channel Center

Approximation

The analytic modeling in the previous section can be done without the channel center approximation. The integration over z (5.1.5.10) is done point-by-point in Matlab. The Matlab code is included in Appendix. This section will show the results only. Note Fig. 5.17 is a 3-dimensional version of the Fig. 1.8.

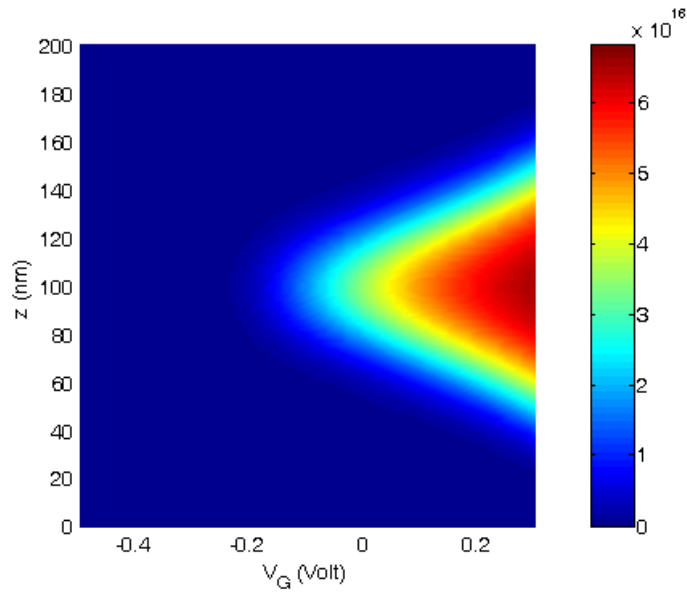


Figure 5.17 The electron density vs. MBE growth direction (z) vs. gate voltage (V_G).

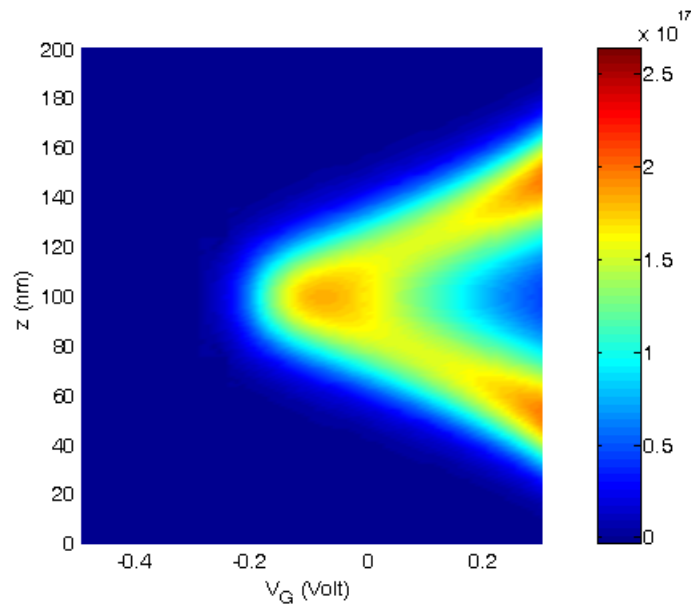


Figure 5.18 Electron density modulation (dn/dV) vs. MBE growth direction (z) vs. gate voltage (V_G). Note the device becomes useless above $V_G = 0.3$ V due to the gate leakage current.

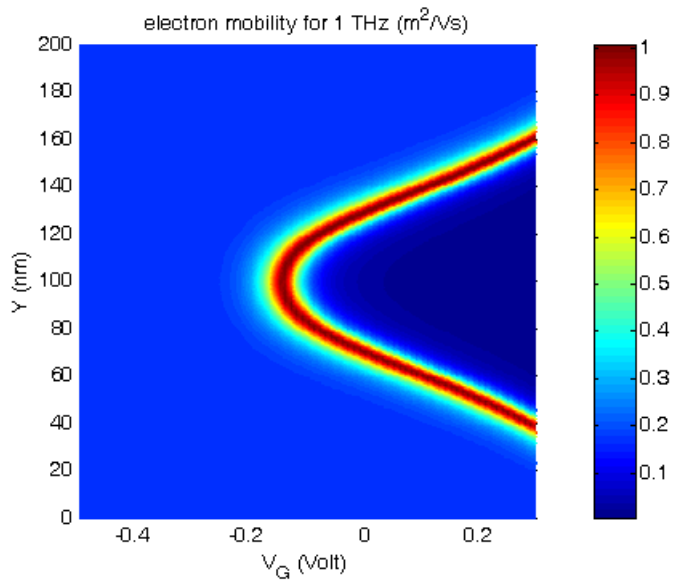


Figure 5.19 $Re(\mu)$ (eq.(5.1.5.8)) for 1 THz vs. MBE growth direction (z) vs. gate voltage (V_G).

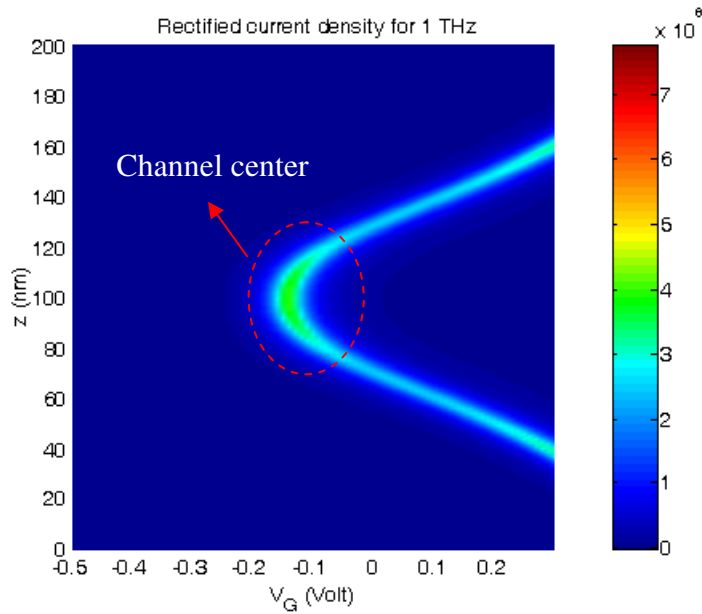


Figure 5.20 The signal current density (eq. (5.1.5.9), proportional to the product of Fig. 5.18 and Fig. 5.19) for 1 THz vs. MBE growth direction (z) vs. gate voltage (V_G). Most of the signal originates from the channel center. Therefore, this one-dimensional simulation validates the channel center approximation in Section 5.1.5.

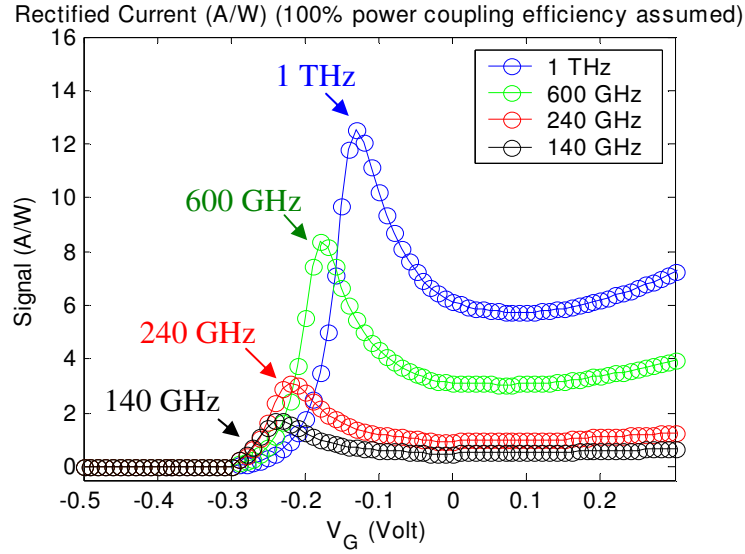


Figure 5.21 The integrated signal current responsivity (eq.(5.1.5.16)) vs. gate voltage (V_G). The result of one-dimensional model agrees with the channel center approximation of Fig. 5.14, as well as the experimental data of Fig. 5.15.

Again, the model (Fig. 5.21) and the experimental data (Fig. 5.15) are in good agreement with each other, both qualitatively and quantitatively. Most of the signal originates from the channel center. Therefore, the result of one-dimensional model validates the channel center approximation in Section 5.1.5 (see Fig. 5.20).

So far, the models are one-dimensional, and have made many assumptions and simplifications on the way. For example, the one-dimensional Poisson calculations are inaccurate for the Y-pol., since the excitation regions are not directly under the gates. Therefore, more accurate results are expected with three dimensional self-consistent 3D Poisson simulations.

5.1.7 Circuit Simulation (Off-Resonant Self-Mixing)

The detector circuit can be simulated with the advanced design system (ADS).¹⁰ ADS requires a device model, and not surprisingly, there seems to be no available GaAs MESFET models for terahertz frequencies. Therefore, ADS simulations can only be done at much lower frequencies. The low-frequency simulations in this section correspond to the operations of the detector at off-resonant condition. Without the resonant assistance of the plasmon, the response exhibits the self-mixing envelope (or the electron density modulation dn/dV peak, Fig. 5.12) only. The simulation correctly captures the bias dependence of the self-mixing envelope.

Fig. 5.22 is the equivalent circuit diagram for the self-mixing detector, or the “self controlled rectification of the RF signal” circuit from Ref [24-26]. The microwave input of frequency 1 GHz is applied across the ground and the gate of the transistor. The microwave leaks into the drain and the source through the built-in parasitic capacitances (C_{gs} : gate-source parasite, C_{gd} : gate-drain parasite). The transistor model NE722S01 is provided by NEC electronics [59], and has $C_{gd} = 0.05$ pF and $C_{gs} = 0.92$ pF (see Fig. 5.23).

¹⁰ ADS is a commercial Electronic Design Automation (EDA) software by Agilent.

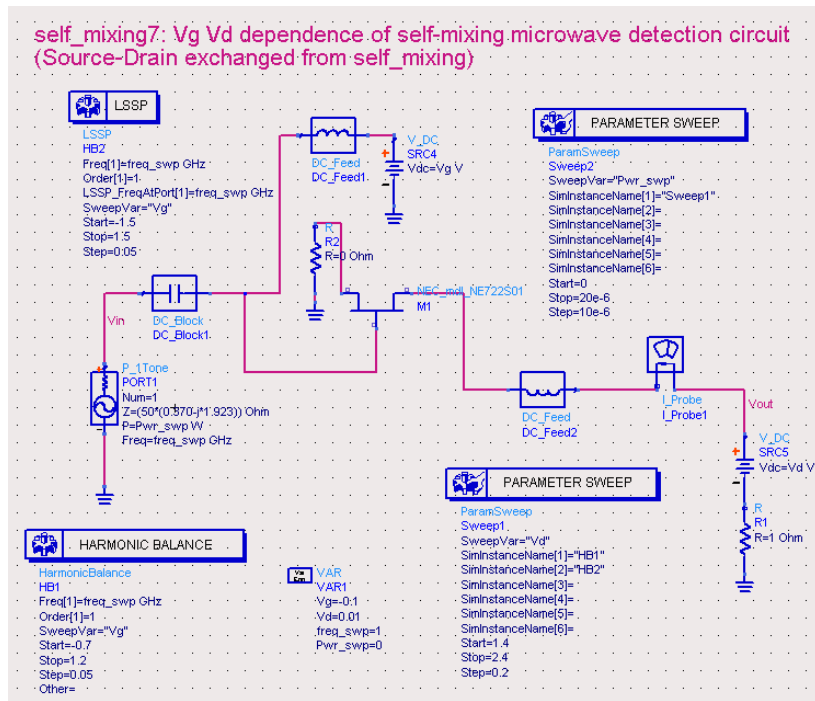


Figure 5.22 Circuit diagram of the self-mixing circuit.

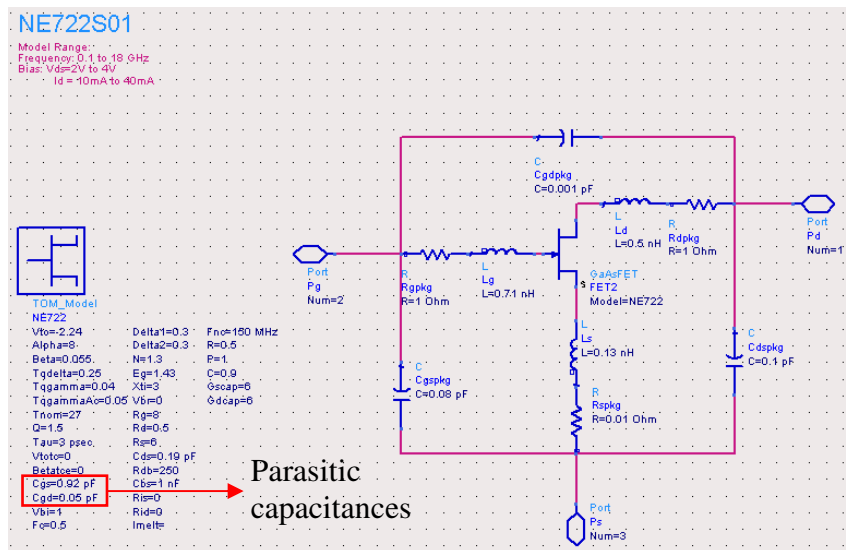


Figure 5.23 Circuit diagram of the GaAs MESFET used in the simulation. The model is provided by NEC electronics. $C_{gd} = 0.05$ pF, $C_{gs} = 0.92$ pF, $C_{gdpkg} = 0.001$ pF, and $C_{gspkg} = 0.08$ pF.

Since the microwave can leak into the source more efficiently in this particular transistor model, the self-mixing generates the rectified signal more strongly when the source is used as an output lead. So, in this section only, V_D is applied across the ground and the “source” of the transistor, and the “drain” is grounded.

In order to obtain the rectified current at each DC bias condition (V_D 's and V_G 's), the current *with* the microwave input was subtracted by the current *without* the microwave input. The resulting response is plotted in Fig. 5.24, and can be compared with the simplified analytical model at the same frequency (1 GHz) in Fig. 5.25, and with the Silicon metal-oxide-semiconductor-field-effect-transistor (MOSFET) based off-resonant self-mixing circuit at 0.6 THz [25] in Fig. 5.26, and finally, with the 0.14 THz experimental result of this work in Fig. 5.15.

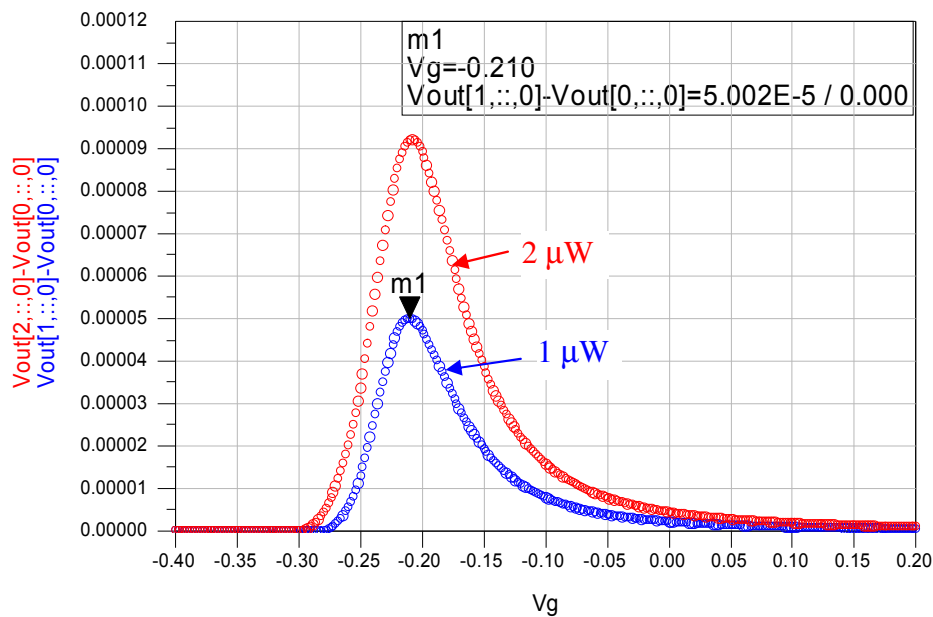


Figure 5.24 ADS simulation with an equivalent self-mixing circuit. Gate voltage (V_G) dependence at 1 GHz. $V_D = 1.5$ Volt was applied.

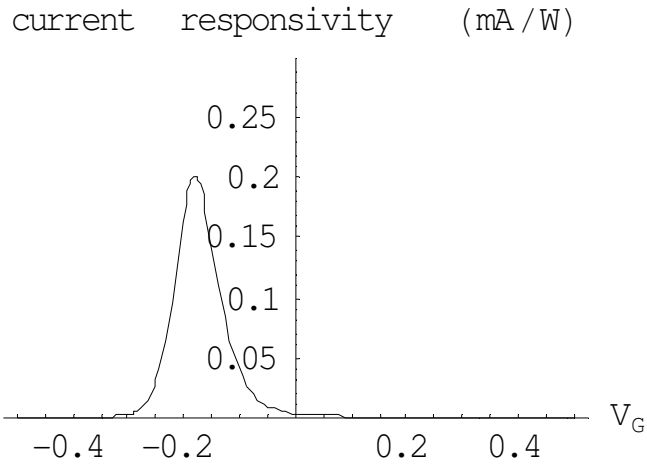


Figure 5.25 Analytical model (eq.(5.1.5.16)) at frequency 1 GHz (off the plasma resonance).

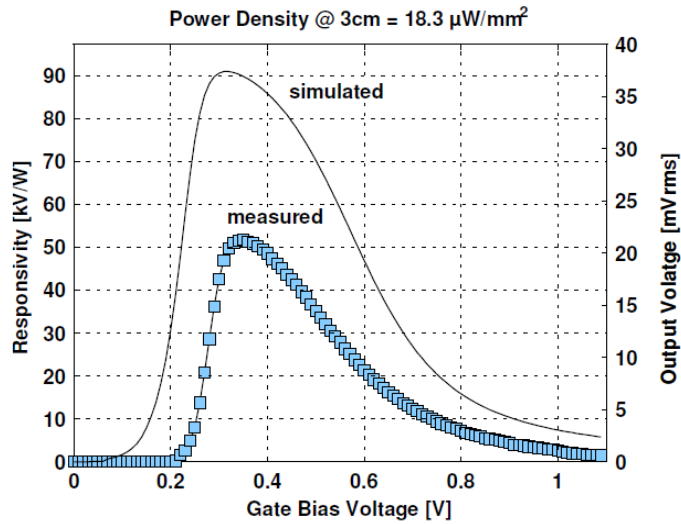


Fig. 5. Measured and simulated pixel responsivity versus V_{gs} -bias.

Figure 5.26 Gate voltage dependence of the Silicon MOSFET-based, off-resonant self-mixing circuit at 600 GHz. Ref [25].

Fig. 5.27 shows the microwave power dependence of the signal. For a small power range (0 ~ 1 μW), the response follows (approximately) the power law –

typical for a rectification process. That is, the magnitude of the generated voltage or current is proportional to the input power.

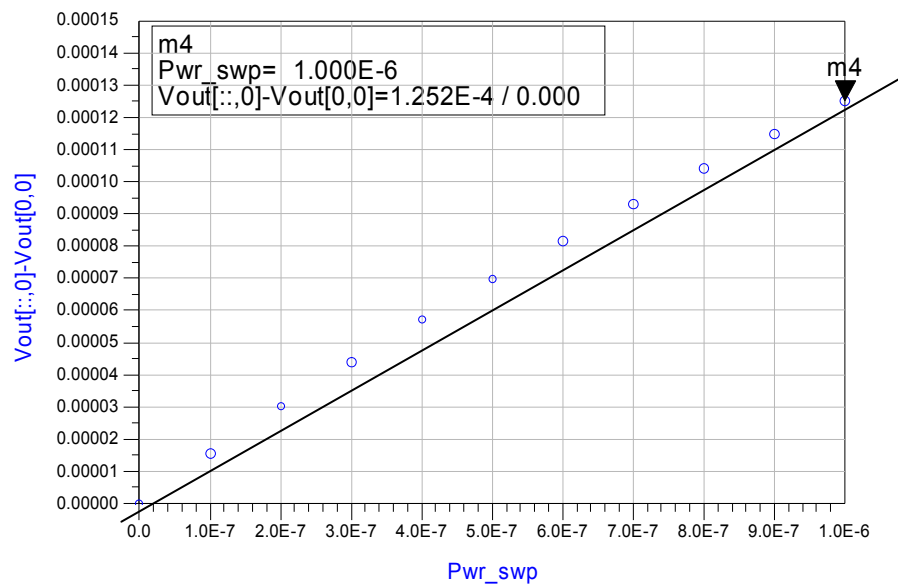


Figure 5.27 Gate voltage dependence of the Silicon MOSFET-based off-resonant self-mixing circuit at 600 GHz.

As the input microwave power increases further, the responsivity drops gradually as shown in Fig. 5.28 (note the scales are logarithmic). The responsivities obtained from this simulation are 125 V/W for small power (0 ~ 1 μ W) regime, and 10 V/W for high power (~ 1mW) regime.

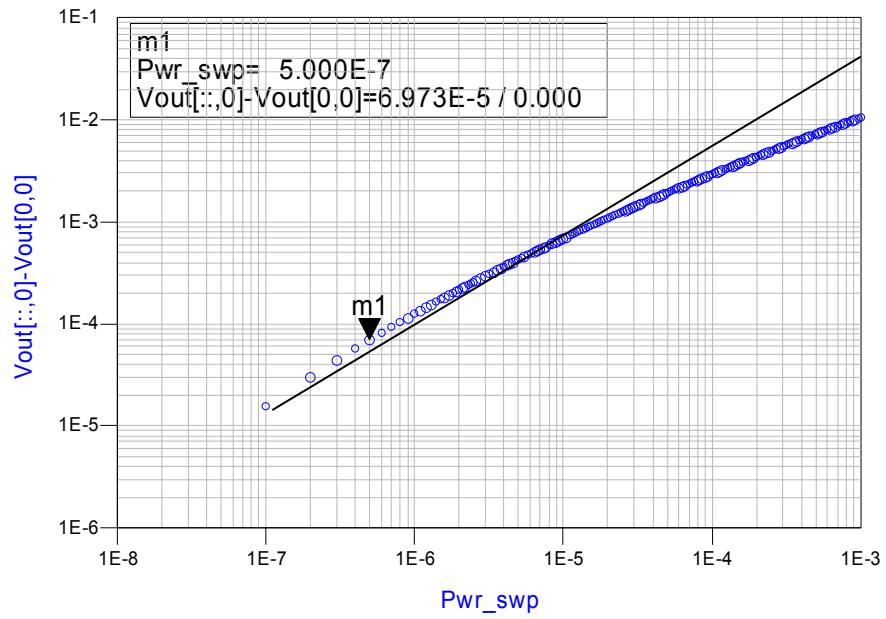


Figure 5.28 The responsivity drops gradually as the input power increases over a wide range. Note the scales are logarithmic.

Finally, V_D dependence of the response is examined in Fig. 5.29, and can be compared with the experimental data of this work shown in Fig. 5.5 ~ 5.9 and Fig. 5.30. In simulations as well as in all the experimental data, the peak position in V_G shifts toward more positive bias, as V_D increases toward more positive bias.

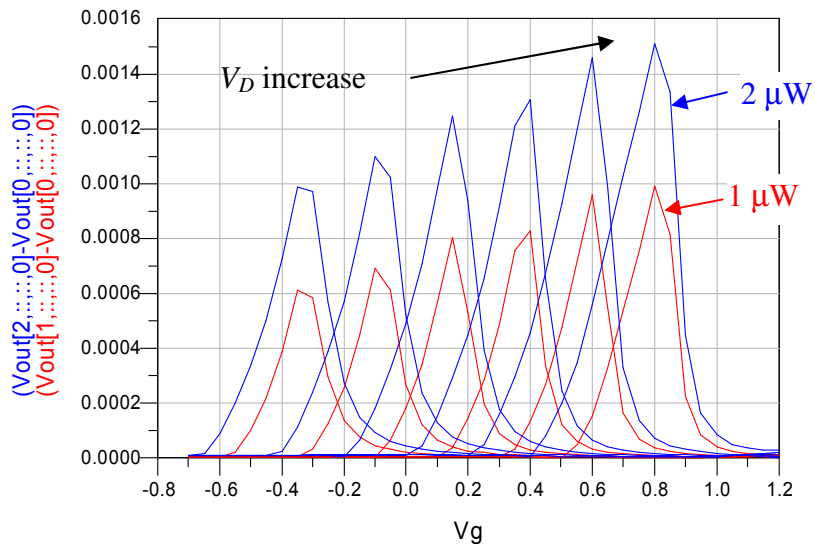


Figure 5.29 V_D dependence of the signal. The signal curves for $V_D = 1.4 \sim 2.4$ V, in 0.2 V step are shown. As V_D increases, the peak position in V_G also increases.

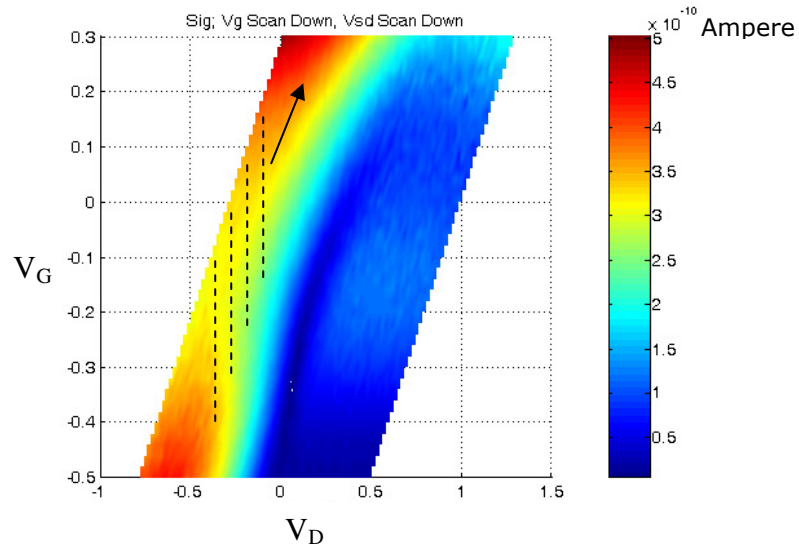
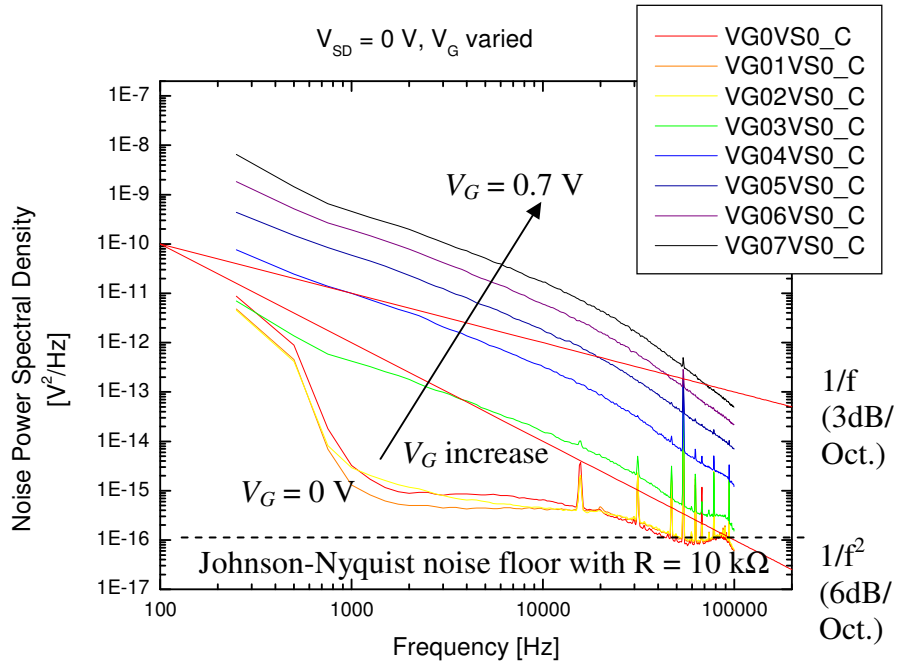


Figure 5.30 V_D dependence of the signal at 1 THz. The experimental data of Fig. 5.5 is shown again. As V_D increases, the peak position in V_G also increases.

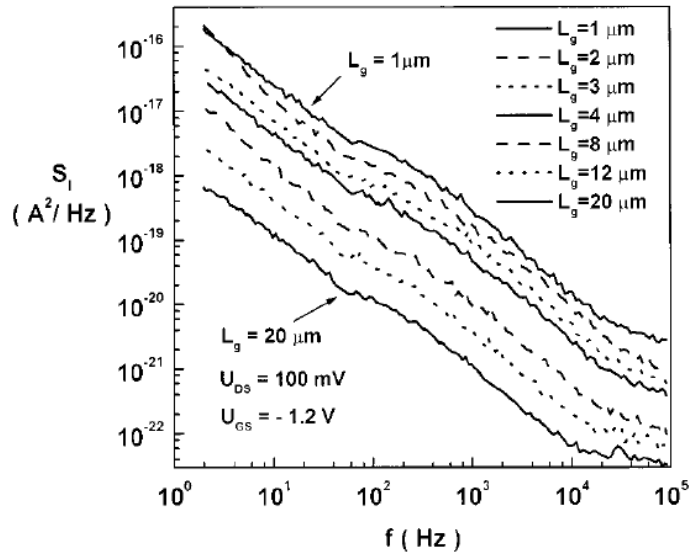
5.2 Noise, SNR , and NEP

The devices in this work exhibit noise spectrum mixture of $1/f$ (power spectral density decrease by 3 dB per octave) and $1/f^2$ (power spectral density decrease by 6 dB per octave) as shown in Fig. 5.31 (a). The source of the $1/f$ noise is suggested to be the Shockley-Read-Hall recombination process in the depleted channel region (see Fig. 5.31 (b) and Ref. [60]). The source of the $1/f^2$ noise is Brownian motion of electrons. Fig. 5.32 shows (a) the signal (identical to Fig. 5.5), (b) noise, and (c) signal-to-noise ratio. $1/f$ -like noise is minimal along the $V_D = 0$ line as can be seen from Fig. 5.31 (a) and Fig. 5.32 (b). This is when there is no DC source-to-drain current. In this purely photovoltaic readout condition, the detector is Johnson / Nyquist noise limited (will be checked at the end of this section).

Therefore, as the detector response is tuned with V_G and V_D , the maximum SNR is found with $V_D = 0$ and a non-zero V_G . For the data shown in (a), the best $SNR = 55.5$ is obtained at $V_G = 0.06$ Volt and $V_D = 0$ Volt. The best reported figures of merits of this work (responsivity = $80 \mu A/W$ and $NEP = 50 \text{ nW/Hz}^{1/2}$) are taken from this point. As V_G is increased, the responsivity improves (see Fig. 5.5 (d)). However, the gate leakage current increases exponentially with V_G , adds an increasing noise (see Fig. 5.5 (e)), and eventually overloads the current preamplifier for $V_G > +0.3$ V.

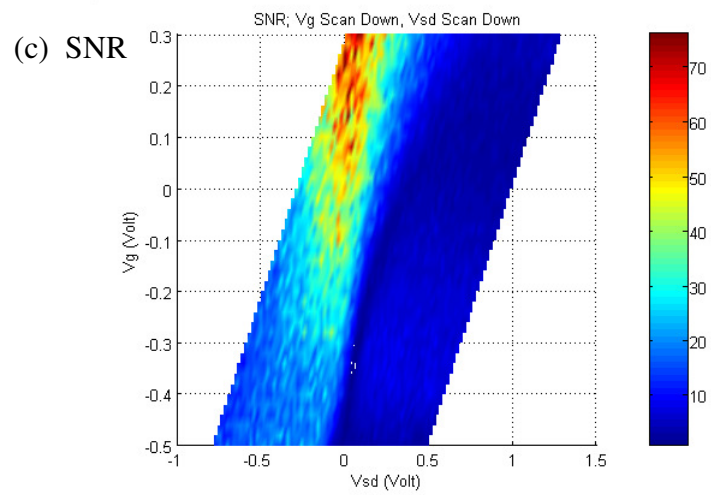
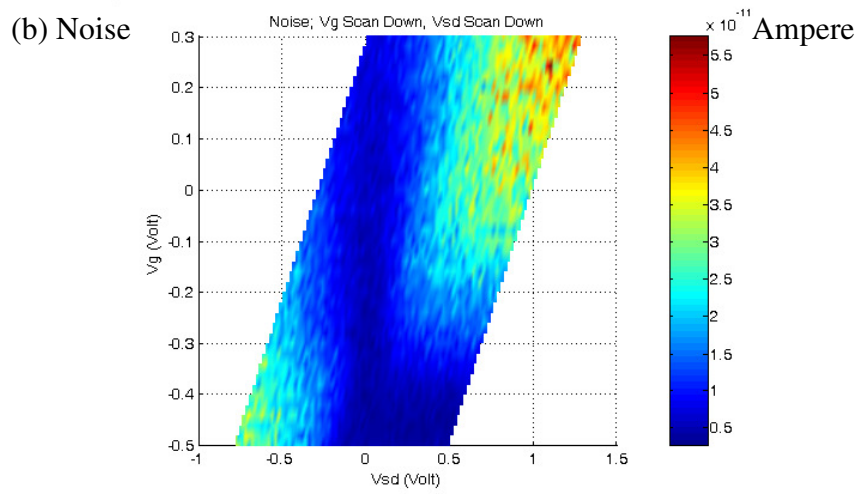
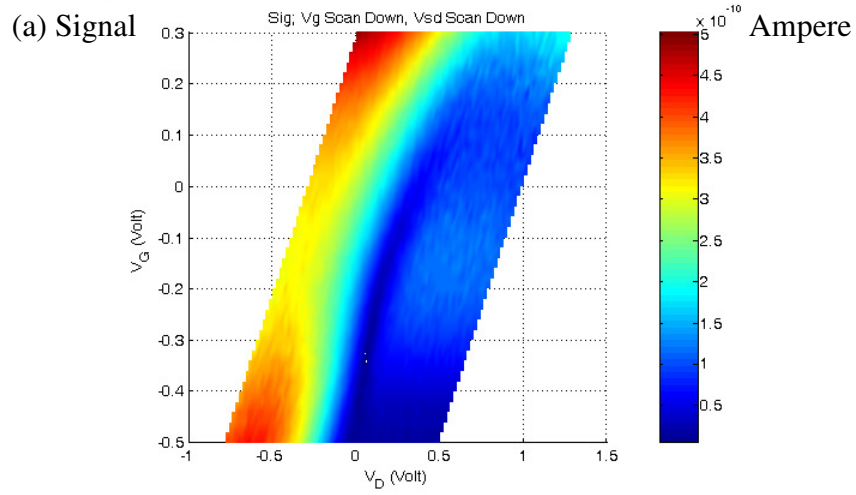


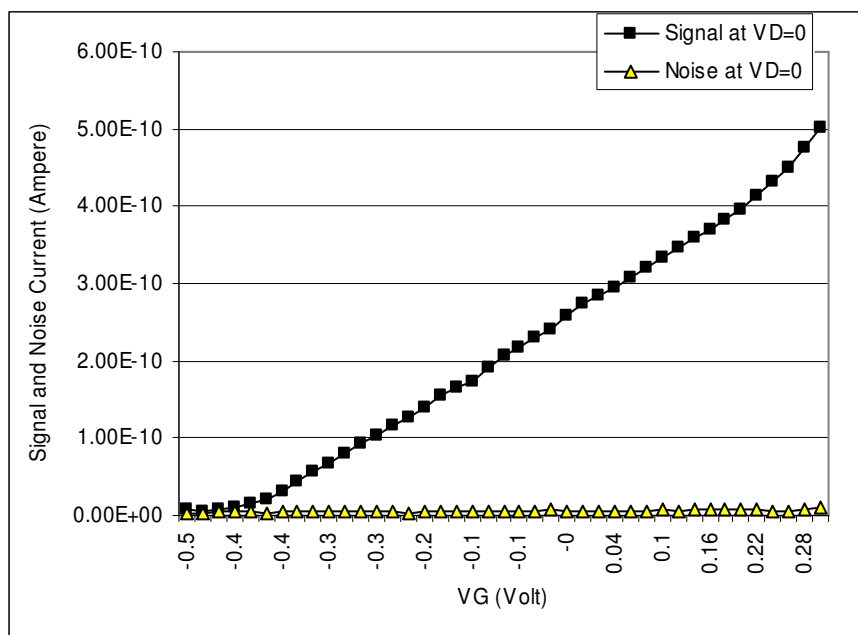
(a)



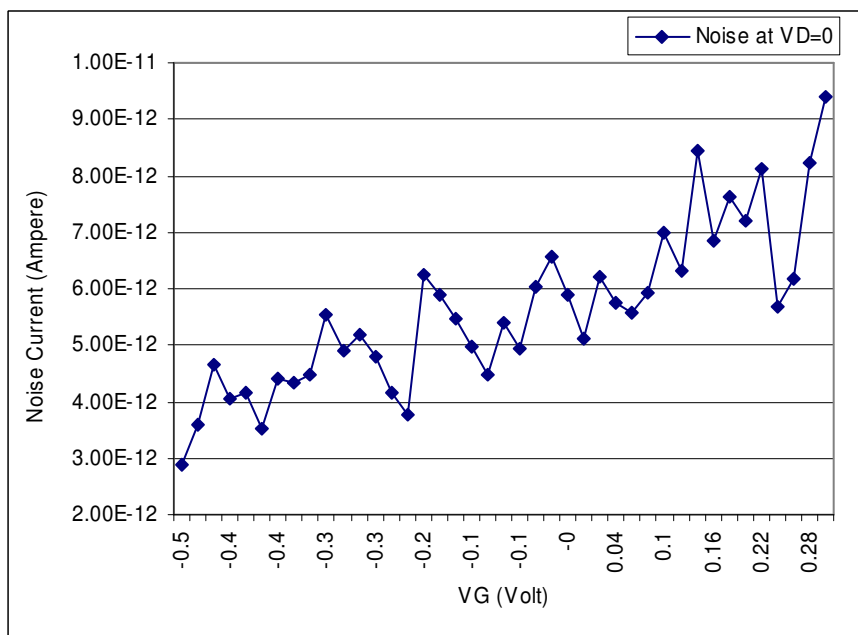
(b)

Figure 5.31 (a) Noise spectrum of device. The dashed line shows the Johnson-Nyquist noise floor $V_N = \sqrt{4k_B T R_{SD}} = I_N \cdot R_{SD} / \sqrt{ENBW}$ with $R_{SD} \sim 10 \text{ k}\Omega$. (b) $1/f$ noise due to the “charge fluctuations in the Shockley–Read–Hall centers found inside the depleted layer below the gate electrode” Dobrzanski *et al.*, Ref. [60].

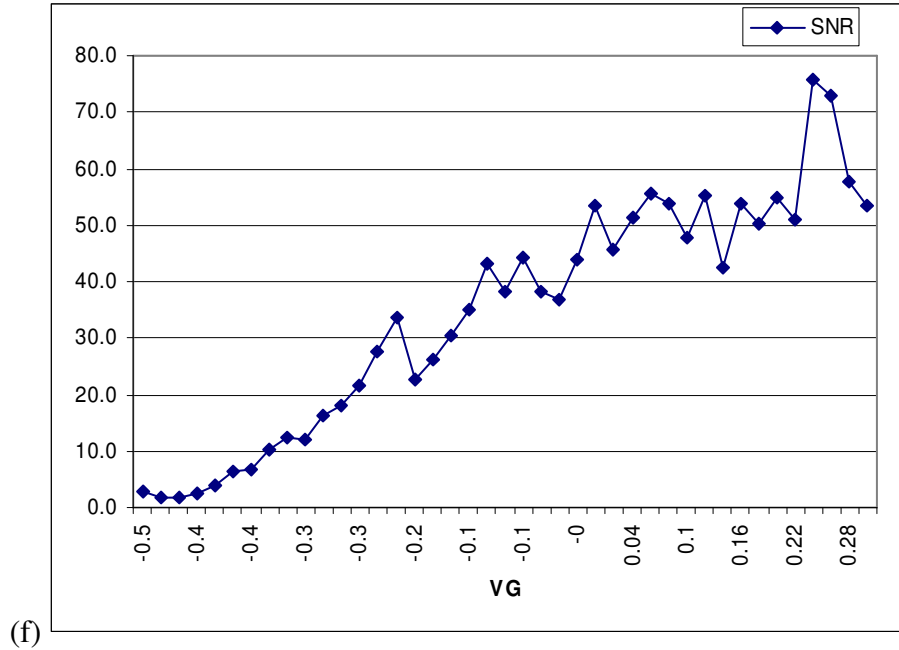




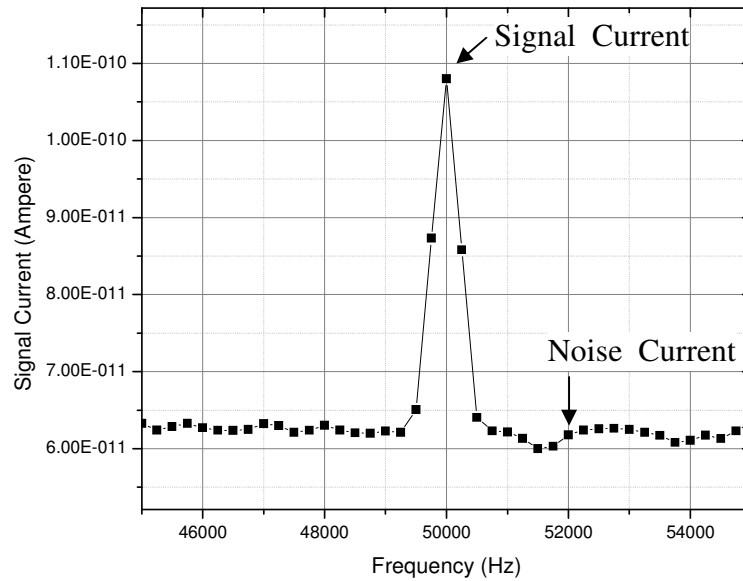
(d)



(e)



(f)



(g)

Figure 5.32 signal-to-noise ratio (*SNR*) (a) Signal (identical to Fig. 5.5), (b) noise, (c) *SNR*; (d), (e), and (f) cross-sections of the signal, noise, and *SNR*, respectively at $V_D = 0$ for $4 \mu\text{W}$, 1 THz radiation. (g) is an example of a spectrum analyzer (SA) trace. The maximum $SNR = 55.5$ and lowest $NEP = 50 \text{ nW/Hz}^{1/2}$ were obtained at $V_G = 0.06$ Volt and $V_D = 0$ Volt. (a) and (b) were taken simultaneously from SA at two different frequencies as shown in (g).

SR760 settings for these measurements were span = 380 Hz, $df = 0.977$ Hz. These settings mean an effective noise bandwidth (= post detection bandwidth) of 1.95 Hz:

$$ENBW = 2 * df = 1.95 \text{ Hz.} \quad (5.2.1)$$

The measured signal current at $V_G = 0.06$ Volt and $V_D = 0$ Volt (the best SNR condition) from the data shown in Fig. 5.32 (a) is ($\sqrt{2}$ for converting rms amplitude to a normal amplitude, 10^{-6} A/V for preamp gain):

$$I_{Signal} = 1.56 * 10^{-4} V_{rms} / \text{Hz}^{1/2} * \sqrt{2} * 10^{-6} \text{ A/V} * \sqrt{ENBW} = 309 \text{ pA.} \quad (5.2.2)$$

The measured responsivity is:

$$\mathfrak{R} = I_{Signal} / P_{in} = 309 \text{ pA} / 4 \mu\text{W} = 77.3 \mu\text{A/W.} \quad (5.2.3)$$

The measured noise current is:

$$I_N = 2.82 * 10^{-6} V_{rms} / \text{Hz}^{1/2} * \sqrt{2} * 10^{-6} \text{ A/V} * \sqrt{ENBW} = 5.57 \text{ pA.} \quad (5.2.4)$$

The measured noise current density is:

$$\text{Noise current density} = \frac{I_N}{\sqrt{ENBW}} = 3.98 \text{ pA/Hz}^{1/2}. \quad (5.2.5)$$

This is comparable to the theoretical thermal noise estimate:

$$\sqrt{\frac{4k_B T}{R_{SD}}} \sim 1.29 \text{ pA/Hz}^{1/2}, \quad \text{with } R_{SD} = 10 \text{ k}\Omega. \quad (5.2.6)$$

Hence, detector of this work is close to thermal noise limited.

The noise equivalent power is

$$NEP = \frac{I_N}{\mathfrak{R} \sqrt{ENBW}} = 5.15 * 10^{-8} \text{ W/Hz}^{1/2}. \quad (5.2.7)$$

The minimum detectable temperature difference ($NE\Delta T$) is also a useful detector metric [21]. At least several hundred mK is desired for a passive thermal imaging application. However, for our detector, $NE\Delta T$ is very large.

$$NE\Delta T = \frac{NEP}{k_B * (spectralBW)} = 7500 \text{ K, with spectral BW} \sim 0.5 \text{ THz.} \quad (5.2.8)$$

This large figure implies that our detector currently is only good for active imaging application where an object is illuminated with an external THz source (e.g., VDI sources).

5.3 Low Temperature Measurements

Low temperature behavior needs more investigation for further understanding of this detector system. An increase of responsivity, as well as a decrease of the thermal noise level, was observed. Here are some preliminary results:

Fig. 5.33 shows the detector responses from the liquid nitrogen-cooled detector (77 K). Responsivity from both polarization was observed. For a comparison of the responsivities, the measurement setup configurations A and B in Fig. 4.8 were used. As shown in Fig. 4.3, Config. A (measures X-pol.) appears as $(\cos\theta)^4$, and Config. B (measures Y-pol.) appears as $(\sin\theta\cos\theta)^2$. By comparing the measured peak detector signals for each configuration, the ratio of the sensitivities to X-pol. and Y-pol. can be estimated as X-pol. : Y-pol. $\sim 1 : 2$.

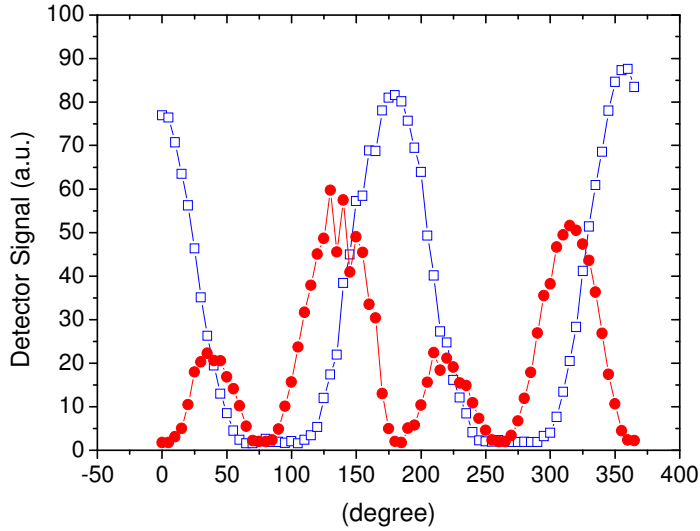


Figure 5.33 Detector measurement at 77 K. The measurement configuration A and B of Fig. 4.8 are used. Terahertz source – X-pol., P2 polarizations: blue, open squares – X-pol.(config A); red, filled circles – Y-pol.(config B). Absolute responsivity is not determined due to the unknown power coupling into the detector.

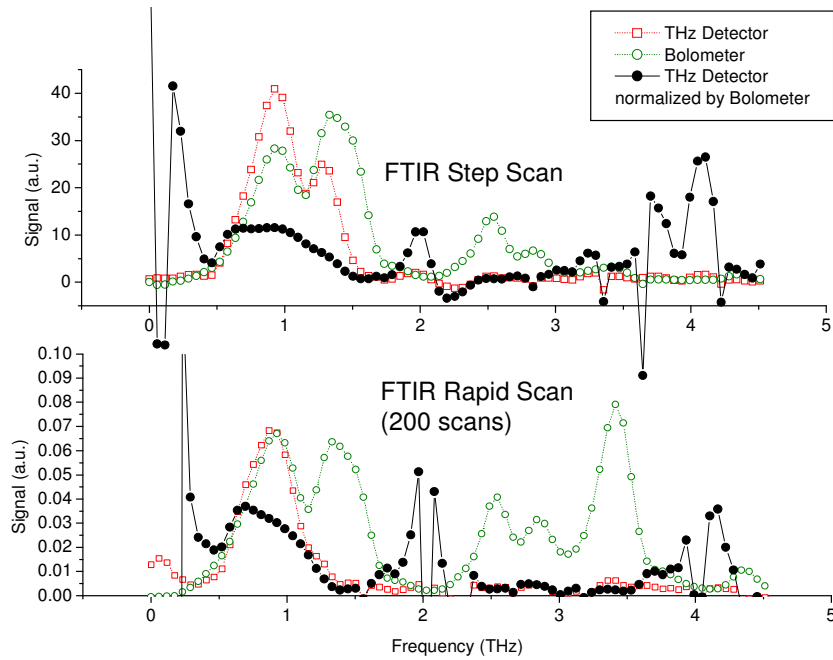


Figure 5.34 FTIR measurement at 4 K. Absolute responsivity is not determined due to the unknown power coupling into the detector.

At 4 K, *SNR* was big enough to see the weak broadband sources of the Bruker Fourier transform infrared (FTIR) spectrometer.¹¹ See Fig. 5.34 for the step scan and the rapid scan data. Both of them show a responsivity peak, which may suggest electron plasmon at around 1 THz.

5.4 Suggestions for Improvement

As mentioned at the end of Section 1.4, the performance of the 2nd generation device of this work would have to improve by factor of about 100 ~ 1000, if it wants to directly compete with the state-of-the-art commercial Schottky diodes. And it seems possible with a clever design, given that the quantitative models in Sections 5.1.5 and 5.1.6 suggest 2 ~ 4 orders of magnitude improvement. Here are a few suggestions for the next generation of plasmon-assisted self-mixing terahertz detector.

As can be seen from eq.(5.1.5.16), it is important to raise the coupling efficiency (α), to tune the plasmon on-resonance for the greatest mobility ($Re(\mu)$), and to increase the density modulation (dn/dV) of the Schottky junction. See Fig. 5.35 for the illustration of the three important factors for the responsivity.

¹¹ Thanks to Christopher Morris for operation of the FTIR spectrometer.

In order to raise the coupling efficiency (α), the detector layout can be modified such that the dual slot dipolar antenna system can be used properly. Also, the multiple self-mixing regions that oppose each other (see Fig. 5.4) can be simplified to one self-mixing region. See Fig. 5.36 for a suggested layout for the 2nd generation detector. The relevant impedance of the GaAs mesa can be obtained for this layout and can be matched with the input impedance of the antenna system. The device should be designed to modulate the electron density efficiently for the most self-mixing (dn/dV). Double gate structure seems helpful, but may not be necessary. Plasma resonance ($Re(\mu)$) can be tuned into the peak of the self-mixing envelope by carefully controlling the dopant density of the MBE sample.

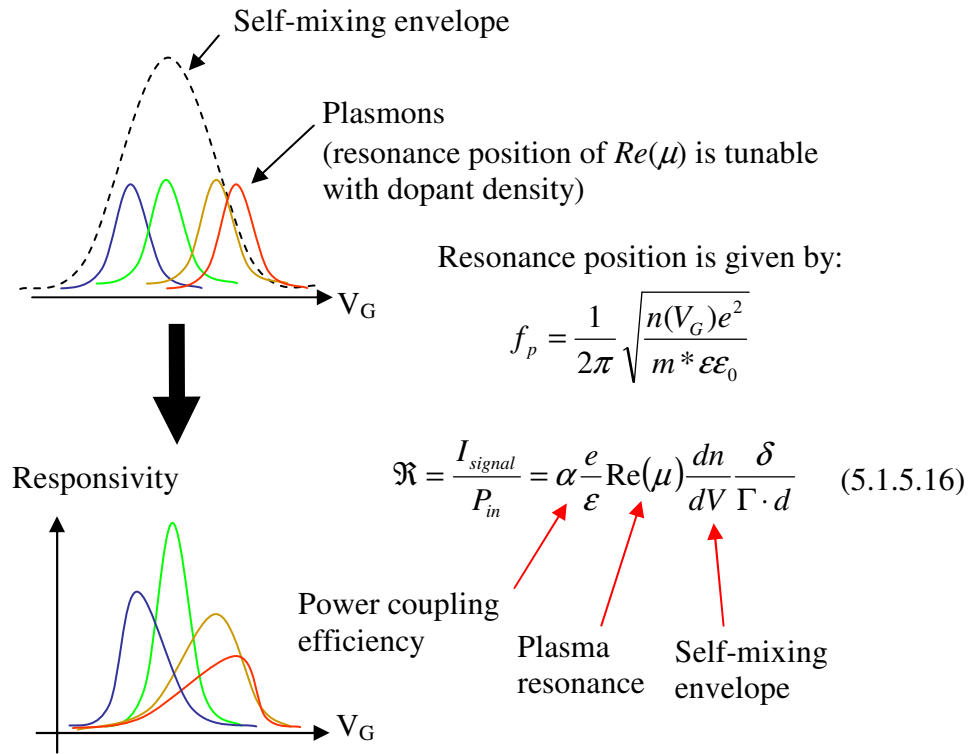


Figure 5.35 Three engineering factors for the responsivity: power coupling efficiency (α), plasma resonance ($Re(\mu)$), and the self-mixing envelope (dn/dV).

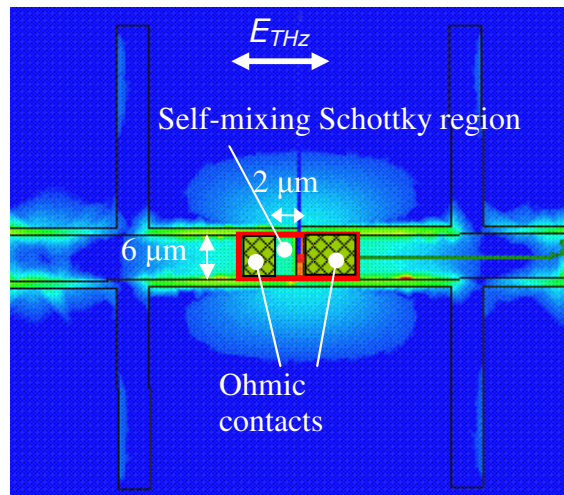


Figure 5.36 Suggested layout for the 2nd generation plasmon-assisted self-mixing detector.

Chapter 6 Conclusions

This work fills the detector version of the “terahertz technological gap” with the new concept of a plasmon detection, and also contributes to the understanding of the electron plasma at high frequency in solid-state systems.

The resonance of the bulk electron plasmons was detected at room temperature in a solid state system through electrical measurements for 0.14, 0.24, 0.6 and 1 THz. Through this work, three important factors for the detector sensitivity are revealed: power coupling efficiency, electron density modulation, and the plasma resonance. If optimized, this new detection concept might greatly improve the sensitivity. It might even enable competition with the state-of-the-art Schottky diode detectors in the room-temperature terahertz detectors market.

Successful detectors of this kind are easy to make in an array. Such devices may be employed to characterize various terahertz sources, such as THz – quantum cascade lasers (QCLs) and free electron lasers (FELs). They could also become affordable, compact receiver parts of a terahertz imaging or communication system. It would also be interesting to navigate the possibility of mid-infrared (MIR) operation or waveguide coupling where the technology may be integrated with various QCLs.

This work reports a responsivity of $80 \mu\text{A/W}$ and a NEP of about $50 \text{ nW/Hz}^{1/2}$ with GaAs FET at 1 THz [30]. The initial theory of the proposed *photoconductive* detection concept is based on previous works by Mark Sherwin *et al.* on TACIT detector [17] and Boris Karasik *et al.* on bolometers [31]. However, the proposed detection scheme did not work, and led to the discovery of another new detection model (*photovoltaic*, “plasmon-assisted self-mixing”). Based on the one-dimensional Poisson simulation results, quantitative device models are developed. The models can our observed data as well as other groups data [23, 25, 57, 58], both qualitatively and quantitatively.

The concept of self-mixing is borrowed from U.R. Pfeiffer [25] and ultimately from “self controlled rectification of the RF signal” by H.-G. Krekels, *et al.* [24].

The concept of 3D plasmon is not borrowed from the 2D plasma wave theory of M.S. Shur Group [23, 57, 58]. Rather, it comes directly from considering the carrier dynamics in the field-effect-transistor. The theory developed in this work is complementary to the work by Lisauskas *et al.* [26], in that this work adopts the self-mixing theory from Ref. [26] but in addition introduces bulk electron plasmon.

The original *photoconductive* model could also become useful, if the oscillator strength can be made in the MBE growth direction only. This is especially true for the intersubband transitions of double quantum wells.

Appendix A Cleanroom

Processings

A.a Overall Processing Steps

This chapter describes cleanroom processing steps for detector chips. The sample wafer is grown by MBE on a 2 inch diameter GaAs wafer (n-GaAs 200 nm / AlGaAs etch stop 1 μm / 500 μm substrate SI-GaAs). The 2-inch sample wafer is cleaved into 4 pieces and each quarter piece is processed separately. The stepper exposes 22 chips on the sample wafer. The first lithography step (0 - alignment marks photo) determines where and how many chips are being exposed. Since there is no alignment marks yet on the sample, the pins on the vacuum chuck are used as a reference. Roughly 2~3 mm apart from the pins gives well-centered exposure areas. All the following lithography layers are aligned to the marks formed at this step 0. The layout can be confirmed after development. If the result is not satisfactory (e.g., chips are too close on wafer edges), the pattern can be washed off with PR stripper 1165 and lithography can be done again. This rework process applies to every step.

A.b Processing Steps Details

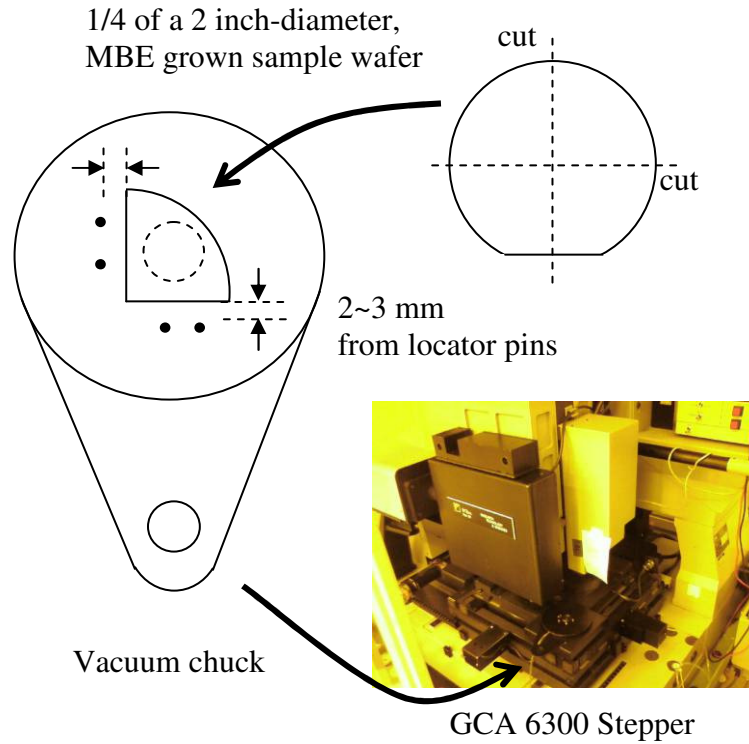


Figure A.1 Stepper, placing sample wafer on the vacuum chuck.

Step 0: Alignment Marks Photo

	Action	Equipment	Comments
1	Clean	clean bench	
2	N ₂ blow, Dry	clean bench	
3	Dehydrate 100 °C, 5 min	hot plate	
4	SPR 510A, 4 krpm, 30 s	PR spinner	TPR ~ 1 μm
5	soft bake 95 °C, 60 s	hot plate	
6	Expose 1.6 s, file:0ALNV5\0	GCA 6300 Stepper	
7	PEB 105 °C, 60 s	hot plate	
8	AZ 300 MIF, 90 s	develop bench	
9	DI rinse + N ₂ blow, Dry	develop bench	
10	Inspection	microscope	

Step 0.1: Alignment Marks Etch 2000Å

11	Descum O ₂ , 300 mT, 100 W, 30 s	PE-IIA	oxide removal
12	NH ₄ OH:DI = 1:10, 20 s	acid wet bench	
13	Citric Acid:H ₂ O ₂ = 4:1, 40 s	acid wet bench	67 Å/s
14	DI rinse + N ₂ blow, Dry	acid wet bench	
15	etch depth check	Dektak	
16	Inspection	microscope	

Step 1: Ohmic Contact Photo

	Action	Equipment	Comments
1	Clean	clean bench	
2	N ₂ blow, Dry	clean bench	
3	Dehydrate 100 °C, 5 min	hot plate	
4	LOL 2000, 1 krpm, 30 s	PR spinner	3500 Å
5	soft bake 150 °C, 5 min	hot plate	
6	SPR 950-0.8, 4 krpm, 30 s	PR spinner	0.8 μm
7	soft bake 95 °C, 60 s	hot plate	
8	CEM 5 krpm, 30s	PR spinner	
9	Expose 1.7 s, file:1OHMV5\1	GCA 6300 Stepper	
10	DI rinse + N ₂ blow, Dry	develop bench	
11	PEB 105 °C, 60 s	hot plate	
12	AZ 300 MIF, 70 s	develop bench	
13	DI rinse + N ₂ blow, Dry	develop bench	
14	Inspection	microscope	

Step 1.1: Ohmic Contact Metal Deposition and Liftoff

15	Descum O ₂ , 300 mT, 100 W, 30 s	PE-IIA	oxide removal
16	NH ₄ OH:DI = 1:10, 20 s	acid wet bench	
17	DI rinse + N ₂ blow, Dry	acid wet bench	
18	Inspection	microscope	
19	Ni/Ge/Au/Ni/Au deposition 50/177/350/100/2000 Å	E-beam #4	
20	Liftoff Aceton or 1165, 2 hr	clean bench	

21	DI rinse + N ₂ blow, Dry	clean bench	
22	Inspection	microscope	
23	Alloy 430 °C, 60 s with forming gas Recipe: 430 45sec forming.rcp	AET RTA	GeAu alloy eutectic 375 °C
24	Check resistance	Probe station	< 1000 Ω
25	Inspection	microscope	

Step 2: Antenna Photo

	Action	Equipment	Comments
1	Clean	clean bench	
2	N ₂ blow, Dry	clean bench	
3	Dehydrate 100 °C, 5 min	hot plate	
4	LOL 2000, 1 krpm, 30 s	PR spinner	3500 Å
5	soft bake 150 °C, 5 min	hot plate	
6	SPR 950-0.8, 4 krpm, 30 s	PR spinner	0.8 μm
7	soft bake 95 °C, 60 s	hot plate	
8	CEM 5 krpm, 30s	PR spinner	
9	Expose 1.7 s, file:2ANTV5\2	GCA 6300 Stepper	
10	DI rinse + N ₂ blow, Dry	develop bench	
11	PEB 105 °C, 60 s	hot plate	
12	AZ 300 MIF, 70 s	develop bench	
13	DI rinse + N ₂ blow, Dry	develop bench	
14	Inspection	microscope	

Step 2.1: Antenna Metal Deposition and Liftoff

15	Descum O ₂ , 300 mT, 100 W, 30 s	PE-IIA	oxide removal
16	Ti/Pt/Au deposition 200/200/2000 Å	E-beam #4	
17	Liftoff Aceton or 1165, 2 hr	clean bench	
18	DI rinse + N ₂ blow, Dry	clean bench	
19	Check resistance	Probe station	< 1000 Ω
20	Inspection	microscope	

Step 2.2: EBASE (Ref. [52])

Epoxy Bonding

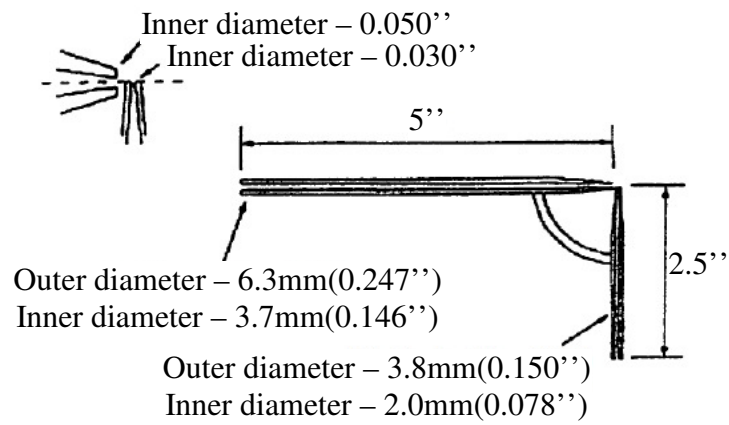
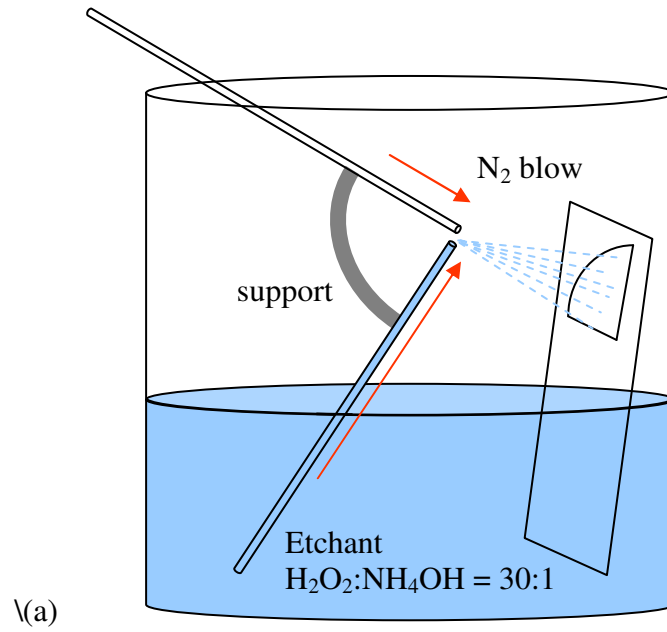
1	mix G-1 epoxy Resin:Hardener = 10:1 (by weight)	scale	squeeze the bottle hard
2	Spin 6 krpm	PR spinner	
3	glue the sample to a piece of GaAs wafer (use a blank undoped GaAs for a new carrier wafer)	PR spinner	press gently
4	Cure 100 °C, 15 min Be careful not to get stuck on the hot plate	hot plate	
5	glue sample on a glass slide with wax	hot plate	100 °C
6	apply SPR950-0.8 for wf side protection		
7	softbake 95 °C, 20~30 min	hot plate	

GaAs Stop Etch 500 μm (Spray, stop at AlGaAs) (Ref. [53])

8	H ₂ O ₂ :NH ₄ OH = 30:1, spray etch 3 hr 300 ml : 10 ml or 200 ml : 6.7 ml 167 μm/hr at wf center 125 μm/hr at wf edge need to over-etch for about 1 hr	Acid wet bench	
9	DI rinse + N ₂ blow, Dry	Acid wet bench	

AlGaAs Stop Etch 1 μm (stop at GaAs)

10	49% HF, 5~10 s, or until etch is finished. Buffered HF is too slow	HF bench	
11	DI rinse + N ₂ blow, Dry	HF bench	
12	PR removal, 1165 + DI Clean	Clean bench	No Aceton
13	Remove sample from the glass slide	Hot plate	100 °C
14	Wax removal, 1165 + DI Clean clean	Clean bench	No Aceton



(b)

Figure A.2 Spray etch setup [53].

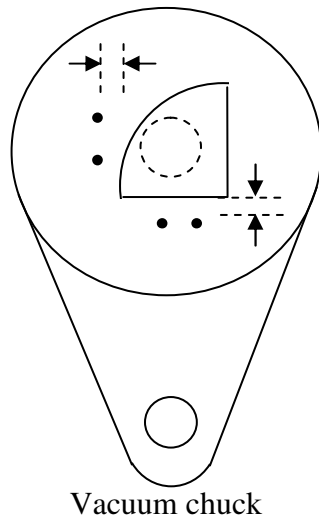


Figure A.3 Wafer loading After EBASE.

Step 3: Mesa Photo

	Action	Equipment	Comments
1	1165 + Clean	clean bench	No Aceton
2	N ₂ blow, Dry	clean bench	
3	Dehydrate 100 °C, 5 min	hot plate	
4	SPR 510A, 4 krpm, 30 s	PR spinner	TPR ~ 1 μm
5	soft bake 95 °C, 60 s	hot plate	
6	Expose 1.6 s, file:3MESV5\3	GCA 6300 Stepper	
7	PEB 105 °C, 60 s	hot plate	
8	AZ 300 MIF, 90 s	develop bench	
9	DI rinse + N ₂ blow, Dry	develop bench	
10	Inspection	microscope	

Step 3.1: Mesa Etch 2000Å

11	Descum O ₂ , 300 mT, 100 W, 30 s	PE-IIA	oxide removal
12	NH ₄ OH:DI = 1:10, 20 s	acid wet bench	
13	Citric Acid:H ₂ O ₂ = 4:1, 40 s	acid wet bench	67 Å/s
14	DI rinse + N ₂ blow, Dry	acid wet bench	
15	etch depth check	Dektak	
16	Inspection	microscope	

Step 4: Spacer Photo (Skip)

Step 5: Backgate Photo

	Action	Equipment	Comments
1	1165 + DI Clean	clean bench	No Aceton
2	N ₂ blow, Dry	clean bench	
3	Dehydrate 100 °C, 5 min	hot plate	
4	LOL 2000, 1 krpm, 30 s	PR spinner	3500 Å
5	soft bake 150 °C, 5 min	hot plate	
6	SPR 950-0.8, 4 krpm, 30 s	PR spinner	0.8 μm
7	soft bake 95 °C, 60 s	hot plate	
8	CEM 5 krpm, 30s	PR spinner	
9	Expose 1.7 s, file:5BGTV5\5	GCA 6300 Stepper	
10	DI rinse + N ₂ blow, Dry	develop bench	
11	PEB 105 °C, 60 s	hot plate	
12	AZ 300 MIF, 70 s	develop bench	
13	DI rinse + N ₂ blow, Dry	develop bench	
14	Inspection	microscope	

Step 5.1: Backgate Metal Deposition and Liftoff

15	Descum O ₂ , 300 mT, 100 W, 30 s	PE-IIA	oxide removal
16	Ti/Pt/Au deposition 200/200/2000 Å	E-beam #4	
17	Liftoff 1165, 2 hr	clean bench	No acetone
18	DI rinse + N ₂ blow, Dry	clean bench	
19	Check resistance	Probe station	< 1000 Ω
20	Inspection	microscope	
21	Measure 4-probe IV curves	Probe station	FET IV
22	Dicing	Disco Dicing Saw	
23	Fab. Out and Test		

A.c Processing Tips

A.c.1 Dehydration Bake

Dehydration bake is needed for good PR adhesion. Otherwise, the adhesion of PR is poor so the pattern lifts off during the wet etch process.

A.c.2 Step 0: Alignment Marks Photo

This step defines alignment marks and verniers with captions “TO 0.0” on the sample wafer. All following layers will be aligned to this mark. This step also determines the positions of 22 chips on a sample wafer. Use SPR 510A instead of SPR 950-0.8 for better adhesion.

A.c.3 GCA6300

Here is an example command sequence:

1	LOG IN [10,1] (Enter)	or L I [10,1] (Enter)
2	MODE (Enter)	mode should be 3
3	LOG OUT	or L O
4	L I [10,345] (Enter)	or LOG IN [10,345] (Enter)
5	LISTF (Enter)	list files
6	ORIG (Enter)	reset stage
7	EDIT 0ALNV5\0 (Enter)	edit expose file
8	EXEC 0ALNV5\0 (Enter)	run expose

A.c.4 Surface Treatment with NH₄OH:DI = 1:10

Solution

Do not skip the surface treatment with NH₄OH:DI = 1:10 solution. If skipped, citric acid:H₂O₂=4:1 etch solution may not work at all.

A.c.5 LOL 2000 and CEM

Use LOL 2000 for undercut to help liftoff. Use CEM (Contrast Enhancement Material) for contrast enhancement.

A.c.6 E-beam #4 vs. E-beam #3

E-beam #4 needs to be pumped for a long time to achieve low pressure. Try signing up for 2 slots (= 4 hours) and use the first 2 hours for pumping. Start deposition when the pressure is below 2×10^{-6} Torr. Use E-beam #4 instead of E-beam#3. The sample holder of E-beam#3 is not normal to the trajectory of evaporated metal sources. Liftoff is difficult with E-beam#3, since it deposits metals on the sides of the photoresist.

A.c.7 Making Ohmic Contacts to N-type GaAs

Ni/Ge/Au/Ni/Au = 50/177/350/100/2000 Å are deposited and annealed at a temperature higher than 400 °C. GeAu alloy forms at above 340 °C, and then spikes into the n-GaAs layer as deep as 750 Å to form an ohmic contact. If the temperature is further raised, the contact resistance gets even lower. For a range of 380 ~ 460 °C, the GeAu alloy takes Ga atoms away from nearby n-GaAs and replace the vacancies with Ge atoms, thereby forming heavily Ge-doped GaAs layer[61]. Therefore, the barrier height is reduced [62] and an ohmic contact is formed.

A.c.8 EPO-TEK 353ND (G-1) Epoxy

The EPO-TEK 353ND (or G-1) epoxy is supplied by Gatan, Inc. [46]. The epoxy endures 400 °C for several hours and operates continuously at 200 °C. Glass transition temperature is $T_g = 100$ °C. G-1 epoxy is not very resistive to solvents, especially to acetone. From here on, use PR stripper 1165 and DI water only (instead of solvents) for cleaning.

A.c.9 Spray Etch

If etch process should be interrupted for any reason, try immersing the sample completely in the etchant upside-down. This way, you can avoid any unwanted film to form, which often stops completely the etch process thereafter. Etch rate is

highest at the center of the wafer. Over-etch of about 1~2 hours is needed in order to etch the whole wafer. [53]

A.c.10 DI Rinse Cleaning

Nanofab staff Ning Cao did some test and gave us guidelines for DI rinse cleaning. The best practice is to repeat 30-seconds-rinse / dump cycles for at least four times.

	Action	Equipment	Comments
1	DI rinse 30 s	develop bench	
2	dump		
3	DI rinse 30 s	develop bench	
4	dump		
5	DI rinse 30 s	develop bench	
6	dump		
7	DI rinse 30 s	develop bench	
8	dump		
9	N ₂ Blow, Dry		

The table below is Ning's experiment for cleaning after AZ300MIF developer.

	Action	Equipment	Comments
1	Resistivity 2.09 MΩ-cm	develop bench	
2	SPR 220-3.0	PR Spinner	
3	Develop AZ 300MIF	develop bench	
4	Resistivity 0.033 MΩ-cm		
5	DI rinse 30 s	develop bench	
6	Resistivity 1.621 MΩ-cm		
7	DI rinse 30 s	develop bench	
8	Resistivity 2.07 MΩ-cm		

In this particular run, the resistivity recovered after 3 cycles of DI rinse / dump.

A.c.11 Solvent Cleaning

Use solvents if samples are contaminated with organic materials, such as finger oil or photoresist.

	Action	Equipment	Comments
1	Aceton 30 s	solvent bench	
2	Methanol 30 s	solvent bench	Skip possible
3	Isopropanol 30 s	solvent bench	Skip possible
4	DI rinse 30 s / dump cycles	develop bench	
5	N ₂ Blow, Dry		

A.c.12 Ultrasonic Cleaning

If additional mechanical vibrations seem helpful, use ultrasonic agitations in combination with DI cleaning or solvent cleaning. Use ultrasonic cleaning with caution, since it could easily destroy fragile samples (thin films, etc). Do not use ultrasonic cleaning after the backside processing.

A.d Processing Cartoons

Here are side views and top views at each step to help better understand the processing.

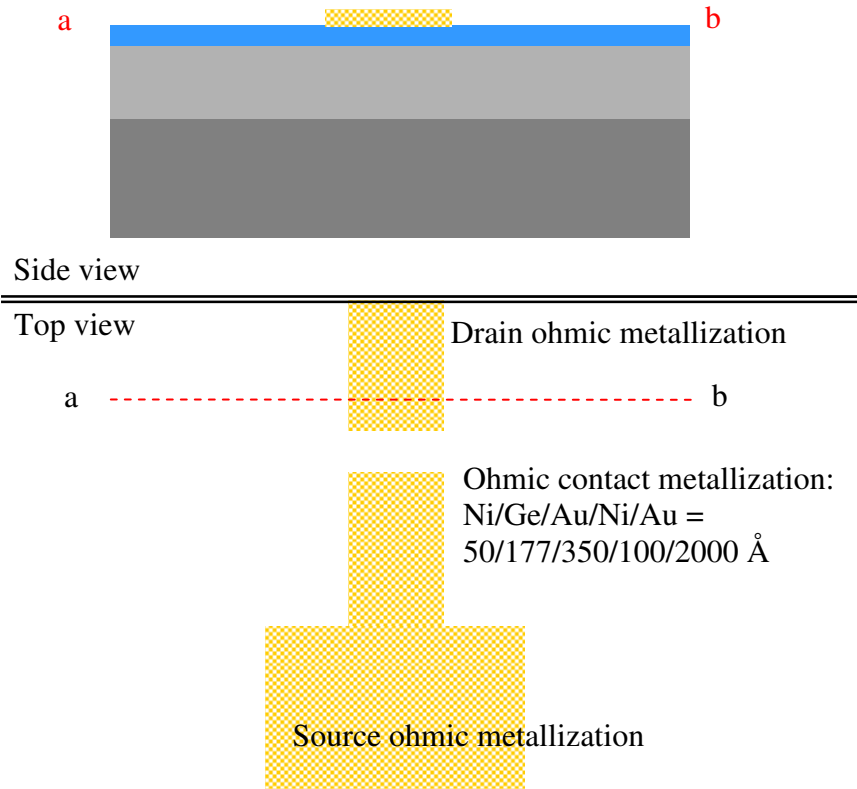


Figure A.4 Ohmic contact formation step.

Fig A.4 illustrates the sample after the step 1.1 (ohmic contact metallization). The lithography layer is aligned to the marks formed at the previous step 0 (alignment marks).

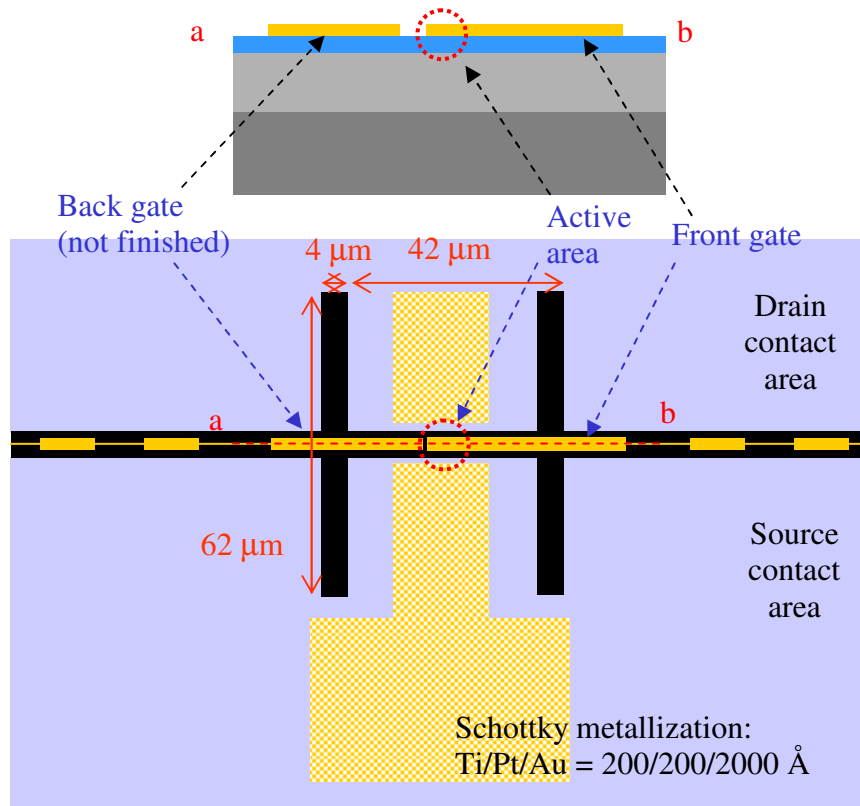


Figure A.5 Antenna metallization step.

Fig. A.5 illustrates the sample after step 2.1 (antenna metallization). Dual slot dipolar antennas, coplanar waveguides (CPWs) and filters are formed at this step.

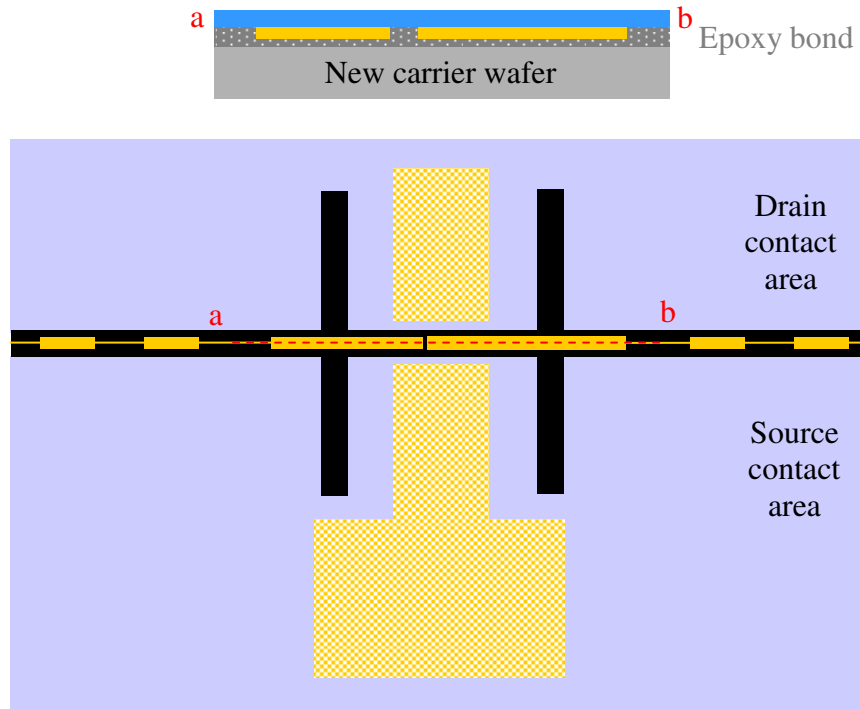


Figure A.6 Epoxy-bond-and-stop-etch (EBASE) step.

The processed side is bonded to another wafer (new carrier wafer) using an epoxy glue [46], then the whole substrate of the sample ($\sim 500 \mu\text{m}$) is removed [52] by the spray-etch technique [53]. See Fig. 3.2 and 3.3 for the pictures of the set-up. The bonded wafer is mounted on a glass slide with wax and photoresist in order to keep the new carrier wafer from being etched during the spray-etch process. After the substrate removal, the sample is unmounted from the glass slide.

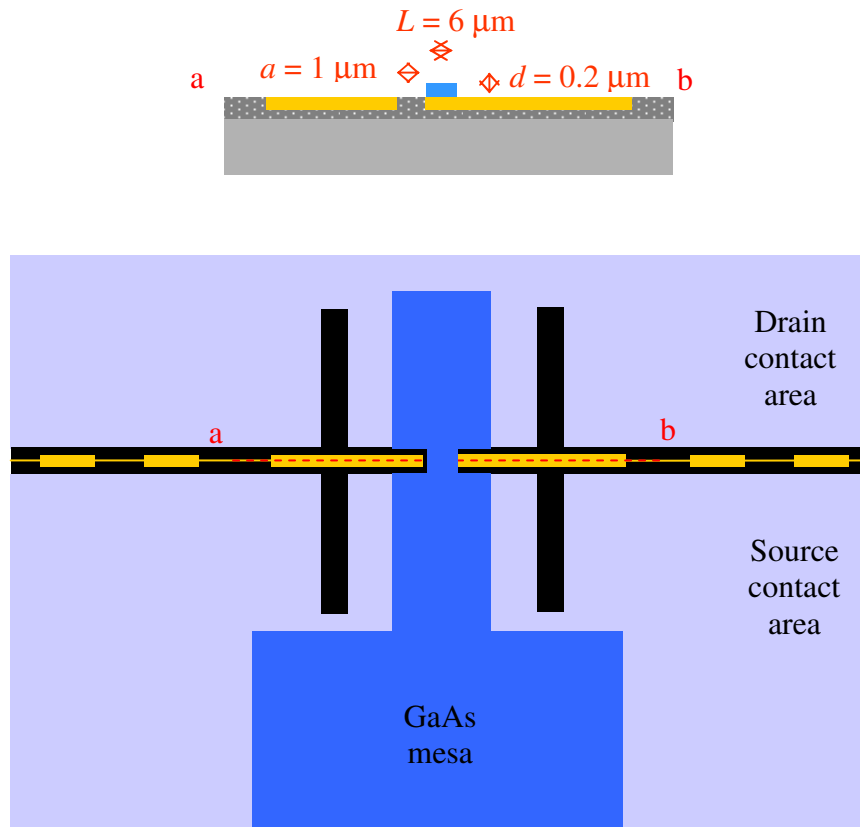


Figure A.7 Mesa formation step.

During the mesa formation etch, all the necessary electrodes are exposed for the following electrical measurements.

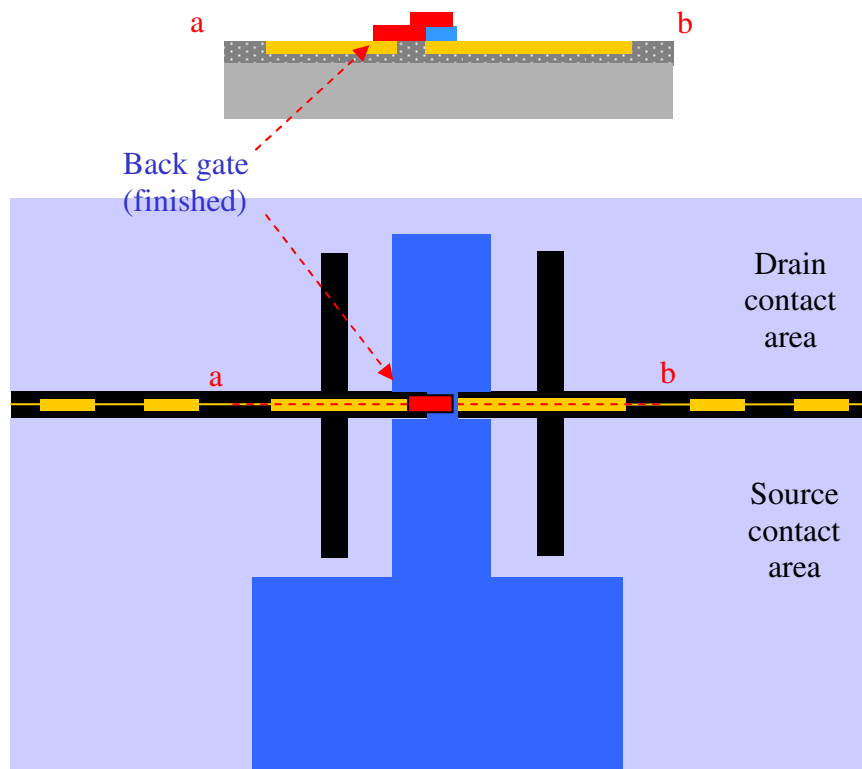


Figure A.8 Back gate metallization step.

Appendix B Imaginary

Number: i or j ?

This appendix clarifies the use of the imaginary number j in this work. As Frank Hegmann mentioned in his talk at IRMMW 2008, this creates “hell of confusion.” Even J.D. Jackson uses an exclamation mark to address this problem, on page 266 of Ref. [39].

Bottom line is that i and j are exactly the same number (see Fig. B.1):

$$i = j \text{ and } i^2 = j^2 = -1. \tag{b.1}$$

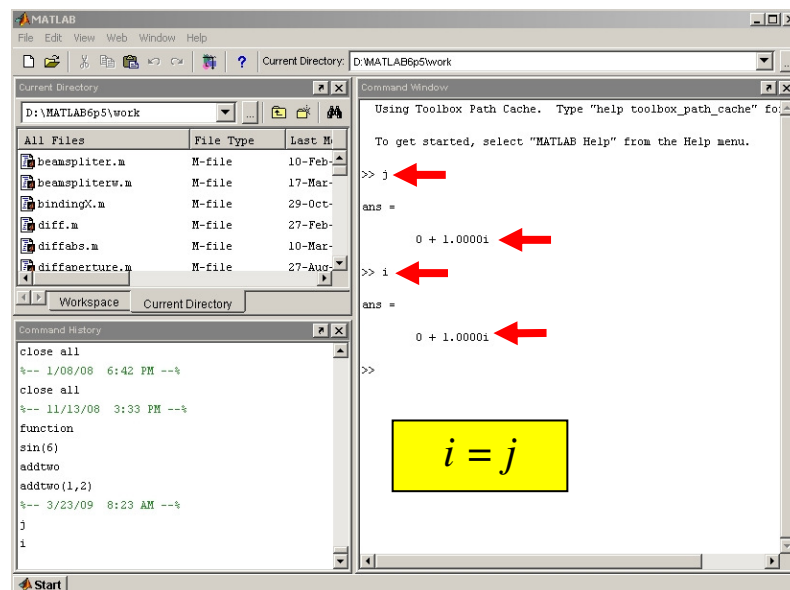


Figure B.1 Matlab showing the equality $i = j$.

It is a matter of choice whether to use i or j , since they represent exactly the same complex number. However, there are subtle differences associated with the use of i and j in various literature. In essence, the “Scientists” group uses i with a choice of phasor $e^{-i\omega t + ikx}$, whereas the “Engineers” group uses j with a choice of phasor $e^{j\omega t - jkx}$. Remembering the equality $i = j$, the choices imply that the calculus of each group are conjugated. i and j can be considered as reminders for the choice of phasor.

The first, “Scientist” group (Ashcroft and Mermin – *Solid State Physics*, Jackson J.D. - *Classical Electrodynamics 3rd ed.*, Boyd – *Nonlinear Optics*) chooses to use i and $e^{-i\omega t + ikx}$. The Maxwell’s equations and various complex physical quantities appear as followings:

$$e^{-i\omega t + ikx} : \text{phasor}, \quad (\text{b.2})$$

$$\nabla \times E = -\frac{\partial B}{\partial t} = i\omega B : \text{Faraday's law}, \quad (\text{b.3})$$

$$\nabla \times H = J + \frac{\partial D}{\partial t} = -i\omega D + J = -i\omega(\epsilon + i\frac{\sigma}{\omega})E : \text{Ampere's law}, \quad (\text{b.4})$$

$$\nabla \cdot D = \rho : \text{Coulomb's law}, \quad (\text{b.5})$$

$$\nabla \cdot B = 0 : \text{No magnetic monopole}, \quad (\text{b.6})$$

$$\sigma = \sigma_1 + i \sigma_2 : \text{electrical conductivity}, \quad (\text{b.7})$$

$$\epsilon = \epsilon_1 + i \epsilon_2 : \text{dielectric constant}, \quad (\text{b.8})$$

$$n = n_1 + i n_2 : \text{index of refraction}, \quad (\text{b.9})$$

$$Z = R - i\omega L - 1/i\omega C : \text{impedance}. \quad (\text{b.10})$$

Note the phase angles of σ , ϵ , and n are measured *counterclockwise* from the $+x$ axis, as familiar to the most Physics majors. However, much unfamiliar, the phase angle of Z is measured *clockwise*, in order to represent the inductive reactance $X_L = -i\omega L$ on the upper half of the complex plane, and the capacitive reactance $X_C = -1/i\omega C$ on the lower half of the complex plane. In this way, scientists give the same interpretation to the imaginary part of impedance as engineers (see Example 1 at the end of this appendix).

The second, “Engineers” group (Brophy – *Basic Electronics for Scientist 5th ed.*, David M. Pozar – *Microwave Engineering 2nd ed.*), uses j and $e^{j\omega t - jkx}$. The Maxwell’s equations and various complex physical quantities appear as followings:

$$e^{j\omega t - jkx} : \text{phasor}, \quad (\text{b.11})$$

$$\nabla \times E = -\frac{\partial B}{\partial t} = -j\omega B : \text{Faraday's law}, \quad (\text{b.12})$$

$$\nabla \times H = J + \frac{\partial D}{\partial t} = j\omega D + J = j\omega(\epsilon - j\frac{\sigma}{\omega})E : \text{Ampere's law}, \quad (\text{b.13})$$

$$\nabla \cdot D = \rho : \text{Coulomb's law}, \quad (\text{b.14})$$

$$\nabla \cdot B = 0 : \text{No magnetic monopole}, \quad (\text{b.15})$$

$$\sigma = \sigma_1 - j\sigma_2 : \text{electrical conductivity}, \quad (\text{b.16})$$

$$\epsilon = \epsilon_1 - j\epsilon_2 : \text{dielectric constant}, \quad (\text{b.17})$$

$$n = n_1 - jn_2 : \text{index of refraction}, \quad (\text{b.18})$$

$$Z = R + j\omega L + 1/j\omega C : \text{impedance}. \quad (\text{b.19})$$

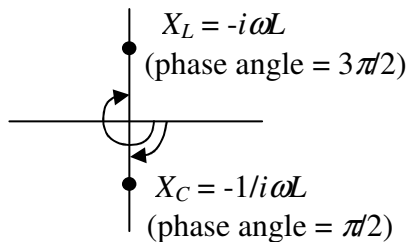
Note the phase angles of σ , ϵ , and n are measured *clockwise* from the $+x$ axis, whereas the phase angle of Z is measured *counterclockwise*, as familiar to (most of?) the Engineering majors. Since Z is measured counterclockwise in Engineers world, the inductive reactance $X_L = j\omega L$ appears on the upper half of the complex plane, the capacitive reactance $X_C = 1/j\omega C$ appears on the lower half of the complex plane (see Example 1 at the end of this appendix). Note also that eqs.(b.2~10) and eqs.(b.11~19) are complex conjugates of each others.

There was one exception found: Yariv - *Optical Electronics in Modern Communications 5th ed.* uses $e^{i\omega t - ikx}$.

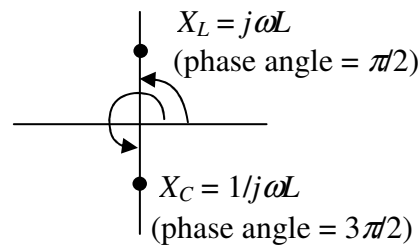
In conclusion, in order to refer to the same physical properties across various literature, we must always clearly know *which phasor* is being used, and *how a phase angle is measured* for the particular physical quantity being used. If a quantity defined by “Scientists” needs to be used by “Engineers,” complex conjugate of the quantity must be taken, and i should be changed with j , or vice versa.

Example 1. Inductive and capacitive reactances on a complex plane:

“Scientists”

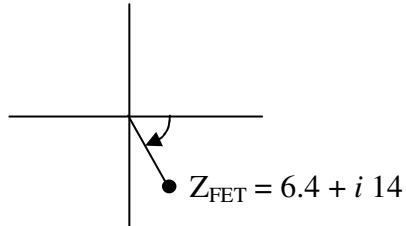


“Engineers”

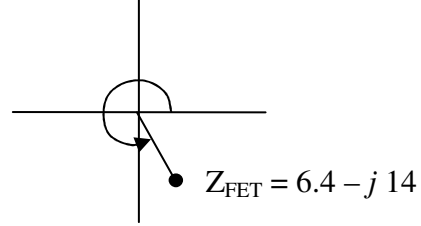


Example 2. $Z_{FET} = 6.4 - j14 \leftrightarrow Z_{FET} = 6.4 + i14$ at 1 THz in Figure 2.7:

“Scientists”



“Engineers”



Note that $6.4 - j14 \neq 6.4 + i14$, but $6.4 - j14 \leftrightarrow 6.4 + i14$, because of the equality $i = j$ (eq.(b.1)).

Example 3. Drude model electrical conductivity:

$$\sigma_{el}(\omega) = \frac{\sigma_0}{1 - i\omega\tau} \overset{\text{Complex Conjugate}}{\leftrightarrow} \sigma_{el}(\omega) = \frac{\sigma_0}{1 + j\omega\tau}. \quad (\text{b.20})$$

Example 4. Dielectric constant – electrical conductivity relation:

$$\epsilon(\omega) = i \frac{\sigma(\omega)}{\omega} \overset{\text{Complex Conjugate}}{\leftrightarrow} \epsilon(\omega) = \frac{\sigma(\omega)}{j\omega}. \quad (\text{b.21})$$

Example 4. Demonstration of physical equivalence:

$$\begin{aligned}
 n_1 + in_2 &= \sqrt{\mathcal{E}_1 + i\mathcal{E}_2} \\
 n_1^2 - n_2^2 + i2n_1n_2 &= \mathcal{E}_1 + i\mathcal{E}_2 \\
 \text{Scientists: } \mathcal{E}_1 &= n_1^2 - n_2^2 \\
 \mathcal{E}_2 &= 2n_1n_2
 \end{aligned} \tag{b.22}$$

vs.

$$\begin{aligned}
 n_1 - jn_2 &= \sqrt{\mathcal{E}_1 - j\mathcal{E}_2} \\
 n_1^2 - n_2^2 - j2n_1n_2 &= \mathcal{E}_1 - j\mathcal{E}_2 \\
 \text{Engineers: } \mathcal{E}_1 &= n_1^2 - n_2^2 \\
 \mathcal{E}_2 &= 2n_1n_2
 \end{aligned} \tag{b.23}$$

Throughout this work, I used j in order to be able to communicate with an antenna engineer.

After all, if all the calculus is equivalent (complex conjugates to each other), and therefore, has no obvious benefit of using one convention than the other, why cause seemingly unnecessary confusion by using both of them? I was not able to find a reference that answers this question. Here is my unofficial answer: It seems to be a historical reason that scientists favor $e^{-i\alpha}$, whereas engineers favor $e^{j\alpha}$, for the time dependent phasor. i might have been reserved for an electrical current when engineers first tried to introduce a phasor. So, i was switched with j . And they also may have wanted to erase the minus sign in the phasor, since it generates minus signs whenever time-differentiated. It might have started this way.

Appendix C Impedance

Matching

This appendix has detailed derivation for the impedance matching condition [45]. As shown in Fig. C.1, a voltage source with a fixed voltage V , and a fixed input impedance Z_A is assumed. We find Z_T which gives maximum power delivered to Z_T .

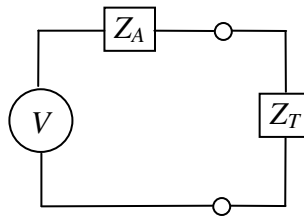


Figure C.1 equivalent circuit of the detector. V is the fixed voltage source, Z_A is the fixed antenna input impedance, and Z_T is the impedance of the transistor.

Z_A is the input impedance of the antenna system seen by the load impedance Z_T .

$$Z_A = R_A + j X_A \quad (\text{c.1})$$

$$Z_T = R_T + j X_T \quad (\text{c.2})$$

Current I and voltage V_T applied to Z_T are given by

$$I = \frac{V}{Z_T + Z_A}, \quad (\text{c.3})$$

$$V_T = V \frac{Z_T}{Z_T + Z_A} \quad (\text{c.4})$$

Power dissipated by Z_T is given by

$$\begin{aligned} P_T &= \frac{1}{2} \text{Re}(V_T I^*) = \frac{1}{2} \text{Re} \left(V \frac{Z_T}{Z_T + Z_A} \left(\frac{V}{Z_T + Z_A} \right)^* \right) \\ &= \frac{1}{2} \frac{|V|^2}{|Z_T + Z_A|^2} \text{Re}(Z_T) \\ &= \frac{1}{2} \frac{|V|^2}{|Z_T + Z_A|^2} R_T \\ &= \frac{1}{2} \frac{|V|^2}{(R_T + R_A)^2 + (X_T + X_A)^2} R_T \end{aligned} \quad (\text{c.5})$$

On the other hand, power dissipated by Z_A is given by

$$P_A = \frac{1}{2} \frac{|V|^2}{(R_T + R_A)^2 + (X_T + X_A)^2} R_A \quad (\text{c.6})$$

Now, taking first partial derivatives of P_T with respect to real (R_T) and imaginary (X_T) parts of the load impedance Z_T , and set them equal to zeros, we find conditions that maximize P_T .

$$\begin{aligned} \frac{\partial P_T}{\partial R_T} &= \frac{1}{2} \frac{|V|^2}{(R_T + R_A)^2 + (X_T + X_A)^2} - \frac{1}{2} \frac{|V|^2 \cdot R_T \cdot 2(R_T + R_A)}{\left((R_T + R_A)^2 + (X_T + X_A)^2 \right)^2} \\ &= \frac{1}{2} \frac{|V|^2}{\left((R_T + R_A)^2 + (X_T + X_A)^2 \right)^2} \cdot \left((R_T + R_A)^2 + (X_T + X_A)^2 - R_T \cdot 2(R_T + R_A) \right) \\ &= \frac{1}{2} \frac{|V|^2}{\left((R_T + R_A)^2 + (X_T + X_A)^2 \right)^2} \cdot \left(R_T^2 - R_A^2 + (X_T + X_A)^2 \right) = 0 \end{aligned} \quad (\text{c.7})$$

and

$$\frac{\partial P_T}{\partial X_T} = -\frac{1}{2} \frac{|V|^2}{\left((R_T + R_A)^2 + (X_T + X_A)^2\right)^2} \cdot R_T \cdot 2(X_T + X_A) = 0. \quad (\text{c.8})$$

Therefore we obtain the conditions for maximum power delivery to the load:

$$R_T = R_A, \text{ and} \quad (\text{c.9})$$

$$X_T = -X_A. \quad (\text{c.10})$$

or equivalently,

$$Z_T = Z_A^* \quad (\text{c.11})$$

Second derivatives give positive values with the condition $Z_T = Z_A^*$.

Therefore (c.11) gives the condition for maximum power delivery to the load.

Note the condition (c.11) also gives non-zero power dissipation by the input impedance of the antenna system. In fact, with the condition (c.11), the power dissipated by the input impedance of the antenna system (c.5) and the power dissipated by the load (c.6) are equal.

$$P_T = P_A \quad (\text{c.12})$$

Therefore, the maximum power delivered to the load is half of the total power that is coupled into the antenna-load system.

Appendix D Mathematica Code

This appendix has the Mathematica code in Section 5.1.5

```

j = i; (* j is engineer's complex, accompanied by the use of phasor e^(jwt-jkx) *)
fmin = 0.1;
fmax = 10;
m = 0.063*9.109*10-31; (* effective mass of conduction band electrons *)
e = 1.602*10-19;
τ = 0.361*10-12;
ε0 = 8.854*10-12;
εDC = 12.9*ε0;
n140GHz = (2*π*0.14*1012)2 (m*εDC)/e2
n240GHz = (2*π*0.24*1012)2 (m*εDC)/e2
n600GHz = (2*π*0.6*1012)2 (m*εDC)/e2
n1000GHz = (2*π*1*1012)2 (m*εDC)/e2
1.9762 * 1020
5.80761 * 1020
3.62976 * 1021
1.00827 * 1022
n3D[VD_,VG_] = 0.2*(8*1022-n600GHz)*(Erf[10*(VG-VD)]+1)/2)+1*1020;
Plot[{n3D[-0.1,VG],n3D[0,VG],n3D[0.2,VG]},{VG,-0.5,0.5}, AxesLabel→{"VG","n (m-3)"},
PlotStyle→{Red,Blue,Black}];
Plot[n3D[0,VG]},{VG,-0.5,0.5}, AxesLabel→{"VG","n (m-3)"}];
Plot[{n3D[VD,-0.1],n3D[VD,0],n3D[VD,0.2]},{VD,-0.5,0.5}, AxesLabel→{"VD","n (m-3)"},
PlotStyle→{Red,Blue,Black}];
ContourPlot[n3D[VD,VG]},{VD,-1,1.5},{VG,-0.5,0.3}];
n3D[-0.2,0]
n3D[-0.15,0]
n3D[-0.05,0]
n3D[0.03,0]
1.53383 * 1022
1.51152 * 1022
1.17121 * 1022
5.22729 * 1021
Dn3D[VD_,VG_]=D[n3D[VD,VG],VG];
Plot[Dn3D[0,VG]},{VG,-0.5,0.5}, PlotRange→{0,1*1023}, AxesLabel→{"VD","dn/dV (m-3V-1)"}];
DensityPlot[Dn3D[VD,VG]},{VD,-1,1.5},{VG,-0.5,0.3}, PlotPoints→100, Mesh→False,
PlotRange→{0,1*1023}}];
ω0[VD_,VG_] =  $\sqrt{\frac{n_{3D}[VD,VG]*e^2}{\epsilon_{DC}*m}}$ ; (* plasma angular frequency of CB electrons *)
Plot3D[ω0[VD,VG]/(2π)},{VD,-1,1.5},{VG,-0.5,0.3}, PlotPoints→100, Mesh→False,
PlotRange→Automatic, ViewPoint→{0,0,5}];
FindRoot[ω0[0,VG]/(2π*109) 140,{VG,-1,1}]
FindRoot[ω0[0,VG]/(2π*109) 240,{VG,-1,1}]
FindRoot[ω0[0,VG]/(2π*109) 600,{VG,-1,1}]
FindRoot[ω0[0,VG]/(2π*109) 1000,{VG,-1,1}]
{VG -0.176054}
{VG -0.131489}
{VG -0.0519897}
{VG 0.0279291}
mobility[VD_,VG_,fTHz_] := (j*(2*π*fTHz*1012)*e/m)/(Subscript[ω, 0][VD,VG]2-
(2*π*fTHz*1012)2+j*(2*π*fTHz*1012)/τ);

```

```

x[VD_,VG_,fTHz_]:= -mobility[VD,VG,fTHz]/(-j*(2*π*fTHz*1012));
(* AC Drude conductivity, contribution from free conduction band electrons *)
Plot[{Re[mobility[0,VG,1]], Im[mobility[0,VG,1]],Abs[mobility[0,VG,1]]},{VG,-
0.5,0.5}, PlotStyle→{Blue,Black, Red}, AxesLabel→{"VG","mobility (m2/Vs)"}];
Plot[{Re[x[0,VG,1]], Im[x[0,VG,1]],Abs[x[0,VG,1]]},{VG,-0.5,0.5},
PlotStyle→{Blue,Black, Red}, AxesLabel→{"VG","x, displacement (m)"}];
(* σ = σr - j σi, σi >0 inductive, σi <0 capacitive, engineers measure phase angle of
σ clockwise. *)

Plot[{Re[mobility[0,VG,0.14]],
Re[mobility[0,VG,0.24]],Re[mobility[0,VG,0.6]],Re[mobility[0,VG,1]]},{VG,-0.5,0.5},
PlotStyle→{Black,Red, Green,Blue}, AxesLabel→{"VG","Re[mobility]"}];

Plot[{Im[mobility[0,VG,0.14]],
Im[mobility[0,VG,0.24]],Im[mobility[0,VG,0.6]],Im[mobility[0,VG,1]]},{VG,-0.5,0.5},
PlotStyle→{Black,Red, Green,Blue}, AxesLabel→{"VG","Im[mobility]"}];

Plot[{Abs[mobility[0,VG,0.14]],
Abs[mobility[0,VG,0.24]],Abs[mobility[0,VG,0.6]],Abs[mobility[0,VG,1]]},{VG,-
0.5,0.5}, PlotStyle→{Red,Green, Blue,Black}, AxesLabel→{"VG","Abs[mobility]"}];

Current[VD_,VG_,fTHz_] = ((e *τ)/εDC)*Re[mobility[VD,VG,fTHz]]*Dn3D[VD,VG]*(0.04*10-6)/
(0.2*10-6);
Plot[{Current[0,VG,0.14],
Current[0,VG,0.24],Current[0,VG,0.6],Current[0,VG,1]}},{VG,-0.5,0.5},
PlotRange→{0,10},PlotStyle→{Black,Red, Green,Blue}, AxesLabel→{"VG","current
responsivity (A/W)"}];

DensityPlot[Current[VD,VG,1],{VD,-1,1.5},{VG,-0.5,0.3}, PlotPoints→100, Mesh→False,
PlotRange→{0,8}];
DensityPlot[Current[VD,VG,0.6],{VD,-1,1.5},{VG,-0.5,0.3}, PlotPoints→100,
Mesh→False, PlotRange→{0,8}];
DensityPlot[Current[VD,VG,0.24],{VD,-1,1.5},{VG,-0.5,0.3}, PlotPoints→100,
Mesh→False, PlotRange→{0,2}];
DensityPlot[Current[VD,VG,0.14],{VD,-1,1.5},{VG,-0.5,0.3}, PlotPoints→100,
Mesh→False, PlotRange→{0,1}];

Plot[Re[mobility[VD,0,0.001]],{VD,-0.5,0.5},AxesLabel→{"VD","mobility (m2/Vs)"}];
Plot[Current[VD,0,0.001],{VD,-
0.5,0.5},PlotRange→{0,0.0002},AxesLabel→{"VD","current responsivity (A/W)"}];

Plot[Re[mobility[0,VG,0.001]],{VG,-0.5,0.5}, AxesLabel→{"VG","mobility (m2/Vs)"}];
Plot[Current[0,VG,0.001]*103,{VG,-0.5,0.5}, PlotRange→{0,0.3},
AxesLabel→{"VG","current responsivity (mA/W)"}];

```

Appendix E 1D-Poisson Code

This appendix has the 1DPoisson script that was used in this work. The simulator is provided by Greg Snider, and “solves the one-dimensional Poisson and Schrodinger equations self-consistently” [63].

```
surface Schottky v1
GaAs t=2000 Nd=8e16
substrate Schottky v1

v1 0.00
schrodingerstart=10
schrodingerstop=2000
temp=300K
dy=10
```

The target was to achieve approximately 400Å thick, $1 \times 10^{16} \text{ cm}^{-3}$ uniform charge sheet at the channel center.

Appendix F Matlab Code

This part of appendix has the Matlab code that was mentioned in Section 5.1.6.

```
clear all;
close all;

[Xtemp,Ytemp]=meshgrid([-0.5:0.05:0.55],[-5:1:204]); % 1DPoisson delta_VG = 0.05
Volt
[VG,Y]=meshgrid([-0.5:0.01:0.55],[-5:1:204]); % new delta_VG = 0.01 Volt

Ztemp(:,:)=Ytemp;
Ztemp2(:,:)=Ytemp;
Ec(:,:)=Y;
Ev(:,:)=Y;
E(:,:)=Y;
Ef(:,:)=Y;
n_noninterp=Ytemp;
n(:,:)=Y;
n2(:,:)=Y;
p(:,:)=Y;
dndv(:,:)=Y;
Ec(:,:)=NaN;
Ev(:,:)=NaN;
E(:,:)=NaN;
Ef(:,:)=NaN;
n(:,:)=NaN;
n2(:,:)=0;
p(:,:)=NaN;
dndv(:,:)=NaN;

M(:,:,1) = dlmread('bias=-0.5, n=1e17.out','\t',[1 1 210 6]);
M(:,:,2) = dlmread('bias=-0.45, n=1e17.out','\t',[1 1 210 6]);
M(:,:,3) = dlmread('bias=-0.4, n=1e17.out','\t',[1 1 210 6]);
M(:,:,4) = dlmread('bias=-0.35, n=1e17.out','\t',[1 1 210 6]);
M(:,:,5) = dlmread('bias=-0.3, n=1e17.out','\t',[1 1 210 6]);
M(:,:,6) = dlmread('bias=-0.25, n=1e17.out','\t',[1 1 210 6]);
M(:,:,7) = dlmread('bias=-0.2, n=1e17.out','\t',[1 1 210 6]);
M(:,:,8) = dlmread('bias=-0.15, n=1e17.out','\t',[1 1 210 6]);
M(:,:,9) = dlmread('bias=-0.1, n=1e17.out','\t',[1 1 210 6]);
M(:,:,10) = dlmread('bias=-0.05, n=1e17.out','\t',[1 1 210 6]);
M(:,:,11) = dlmread('bias=0, n=1e17.out','\t',[1 1 210 6]);
M(:,:,12) = dlmread('bias=0.05, n=1e17.out','\t',[1 1 210 6]);
M(:,:,13) = dlmread('bias=0.1, n=1e17.out','\t',[1 1 210 6]);
M(:,:,14) = dlmread('bias=0.15, n=1e17.out','\t',[1 1 210 6]);
M(:,:,15) = dlmread('bias=0.2, n=1e17.out','\t',[1 1 210 6]);
M(:,:,16) = dlmread('bias=0.25, n=1e17.out','\t',[1 1 210 6]);
M(:,:,17) = dlmread('bias=0.3, n=1e17.out','\t',[1 1 210 6]);
M(:,:,18) = dlmread('bias=0.35, n=1e17.out','\t',[1 1 210 6]);
M(:,:,19) = dlmread('bias=0.4, n=1e17.out','\t',[1 1 210 6]);
M(:,:,20) = dlmread('bias=0.45, n=1e17.out','\t',[1 1 210 6]);
M(:,:,21) = dlmread('bias=0.5, n=1e17.out','\t',[1 1 210 6]);
M(:,:,22) = dlmread('bias=0.55, n=1e17.out','\t',[1 1 210 6]);
%M(:,:,23) = dlmread('bias=0.6, n=1e17.out','\t',[1 1 210 6]);
% dlmread -> zero-based so that R=0 and C=0 specifies the first value in the file.

hl = figure;
```

Initializing variables.

Reading one-dimensional Poisson simulation results. (dV = 0.05 V).

```

hold on;
for k2=1:22,
    Ztemp(:,k2)=M(:,1,k2);
    h1 = plot(Ytemp(:,1),Ztemp(:,k2),'.b');
end
Ec=interp2(Xtemp,Ytemp,Ztemp,VG,Y,'linear'); % conduction band
for k2=1:106,
    h1 = plot(Y(:,1),Ec(:,k2),'.b');
end
for k2=1:22,
    Ztemp(:,k2)=M(:,2,k2);
    h1 = plot(Ytemp(:,1),Ztemp(:,k2),'.r');
end
Ev=interp2(Xtemp,Ytemp,Ztemp,VG,Y,'linear'); % valence band
for k2=1:106,
    h1 = plot(Y(:,1),Ev(:,k2),'.r');
end

for k2=1:22,
    Ztemp(:,k2)=M(:,4,k2);
    h1 = plot(Ytemp(:,2),Ztemp(:,k2),'.g');
end
Ef=interp2(Xtemp,Ytemp,Ztemp,VG,Y,'linear'); % Fermi level
for k2=1:106,
    h1 = plot(Y(:,1),Ef(:,k2),'.g');
end
xlabel('Y (nm)');
ylabel('energy (eV)');

h2 = figure;
hold on;
for k2=1:22,
    n_noninterp(:,k2)=M(:,5,k2);
    h2 = plot(Y(:,1),n_noninterp(:,k2),'.k');
end
Ztemp=interp2(Xtemp,Ytemp,n_noninterp,VG,Y,'spline'); % electron density
Ztemp2=interp2(Xtemp,Ytemp,n_noninterp,VG,Y,'linear'); % electron density
for k1=1:210,
    for k2=1:106,
        if (Ztemp(k1,k2) > 1e11)
            n(k1,k2)=Ztemp(k1,k2);
        else
            n(k1,k2)=Ztemp2(k1,k2);
        end
    end
end

for k2=1:106,
    h2 = plot(Y(:,1),n(:,k2),'.b');
end

for k1=86:126,
    N(k1-85,:)=n(k1,:);
end

for k2=1:106,
    mn(k2)=mean(N(:,k2));
end

for k1=86:126,
    n2(k1,:)=mn;
end

for k2=1:106,
    h2 = plot(Y(:,1),n2(:,k2),'.r');
end
xlabel('Y (nm)');

```

*Interpolating IDPoisson data
($dV = 0.05 \text{ V} \rightarrow 0.01 \text{ V}$).*

*Interpolating IDPoisson data
($dV = 0.05 \text{ V} \rightarrow 0.01 \text{ V}$):
spline for $n > 1e11 \text{ cm}^{-3}$,
linear for $n < 1e11 \text{ cm}^{-3}$.*

*Average electron density
(Channel center approximation).*

```

ylabel('electron density (cm^{-3})');

% mean plasma frequency at the channel center
fp = 1/(2*pi)*sqrt(mn*1e6*(1.602e-19)^2/(12.9*8.854e-12*0.063*9.109e-31));

% plasma frequency (not averaged)
fplasma = real(1/(2*pi)*sqrt(n*1e6*(1.602e-19)^2/(12.9*8.854e-12*0.063*9.109e-31)));

% FET mutual transconductance gm = dI/dV (I = drain current, V = gate voltage)
% FET channel charge density modulation dndv = dn/dV, dV = 0.01 volt

dv = 0.01;
dndv(:,1)=0;
for k1=2:106,
    dndv(:,k1)=(n(:,k1)-n(:,k1-1))/dv;
end

gamma = 1/0.361e-12; % energy relaxation rate

% electron drift velocity for 1 THz, 600 GHz, 240 GHz, and 140 GHz
% in fact this is mobility, since the Electric field is dropped out. v = mu*E
v1000 = -j*1e12*1.602e-19/(2*pi*0.063*9.109e-31)/(fplasma.^2-
(1e12)^2+j*gamma*1e12/(2*pi));
v600 = -j*0.6e12*1.602e-19/(2*pi*0.063*9.109e-31)/(fplasma.^2-
(0.6e12)^2+j*gamma*0.6e12/(2*pi));
v240 = -j*0.24e12*1.602e-19/(2*pi*0.063*9.109e-31)/(fplasma.^2-
(0.24e12)^2+j*gamma*0.24e12/(2*pi));
v140 = -j*0.14e12*1.602e-19/(2*pi*0.063*9.109e-31)/(fplasma.^2-
(0.14e12)^2+j*gamma*0.14e12/(2*pi));

% signal for 1 THz, 600 GHz, 240 GHz, and 140 GHz
% signal is the rectified current density (A/m^2-W)
% dn/dV unit conversion from cm^{-3}V^{-1} to m^{-3}V^{-1}

alpha = 1; % power coupling efficiency. 100% assumed.
al = 1e-6; % field enhancement factor, al = 1 micrometer assumed.
d = 0.2e-6; % MBE layer thickness.

signal1000 = alpha * 1.602e-19 * dndv*1e6 .* real(v1000) / (12.9*8.854e-12* gamma
*d);
signal600 = alpha * 1.602e-19 * dndv*1e6 .* real(v600) / (12.9*8.854e-12* gamma
*d);
signal240 = alpha * 1.602e-19 * dndv*1e6 .* real(v240) / (12.9*8.854e-12* gamma
*d);
signal140 = alpha * 1.602e-19 * dndv*1e6 .* real(v140) / (12.9*8.854e-12* gamma
*d);

% integrated signal is the rectified current responsivity (Ampere/Watt)

W = 3.3e-6; % width of channel 3.3 micrometer.
dY = 1e-9; % 10 Anstrom = 1e-7 cm

for k1=1:106,
    IntegSig1000(k1)=sum(signal1000(:,k1))* dY;
    IntegSig600(k1)=sum(signal600(:,k1))* dY;
    IntegSig240(k1)=sum(signal240(:,k1))* dY;
    IntegSig140(k1)=sum(signal140(:,k1))* dY;
end

figure;
hl=surf(VG,Y,n);
colorbar;
colormap jet;
shading interp;

```

*Electron density modulation
(self-mixing envelope).*

*Electron
mobility
(eq.(5.1.5.8)).*

Rectified current density (eq.(5.1.5.15)).

*Responsivity
(eq.(5.1.5.16)).*

*Electron density false-
color 3D plot (Fig. 5.17).*

```

%view(2);
%axis ([-1 1.5 -0.5 0.6]);
view([-70, 70]);
axis([-0.7 0.6 -50 250 0 7e16]);
xlabel('V_{G} (Volt)');
ylabel('Y (nm)');
zlabel('electron density (cm^{-3})');
% set(h1, 'FaceLighting', 'phong', 'FaceColor', 'interp', ...
% 'AmbientStrength', 0.5)
% light('Position', [1 0 0], 'Style', 'infinite');

figure;
h2=surf(VG, Y, fplasma);
colorbar;
colormap jet;
shading interp;
% view(2);
% axis ([-1 1.5 -0.5 0.3]);
view([-70, 70]);
axis([-0.7 0.6 -50 250 0 3e12]);
xlabel('V_{G} (Volt)');
ylabel('Y (nm)');
zlabel('plasma frequency (Hz)');

figure;
h3=plot(VG(1,:), n(10,:), 'o-b');
hold on;
h3=plot(VG(1,:), n(52,:), 'o-g');
h3=plot(VG(1,:), n(105,:), 'o-r');
h3=plot(VG(1,:), mn, 'o-k');
xlabel('V_{G} (Volt)');
ylabel('electron density(cm^{-3})');
axis([-0.65 0.65 0 7e16]);
legend('near the gate', 'off center', 'channel center', 'channel center average');

figure;
h4=plot(VG(1,:), fplasma(10,:), 'o-b');
hold on;
h4=plot(VG(1,:), fplasma(52,:), 'o-g');
h4=plot(VG(1,:), fplasma(105,:), 'o-r');
xlabel('V_{G} (Volt)');
ylabel('Plasma Frequency (Hz)');
axis([-0.65 0.65 0 2.7e12]);
legend('near the gate', 'off center', 'channel center');

figure;
h5=surf(VG, Y, dndv);
colorbar;
colormap jet;
shading interp;
% view(2);
% axis ([-1 1.5 -0.5 0.3]);
view([-70, 70]);
axis([-0.7 0.6 -50 250 0 10e17]);
xlabel('V_{G} (Volt)');
ylabel('Y (nm)');
zlabel('dn/dV (cm^{-3}V^{-1})');

figure;
h6=plot(VG(1,:), dndv(10,:), 'o-b');
hold on;
h6=plot(VG(1,:), dndv(52,:), 'o-g');
h6=plot(VG(1,:), dndv(105,:), 'o-r');
xlabel('V_{G} (Volt)');
ylabel('dn/dV (cm^{-3}V^{-1})');
axis([-0.65 0.65 0 5e17]);
legend('near the gate', 'off center', 'channel center');

figure;
h11=plot(Y(:,17), [n(:,101), n2(:,101)], 'b');

```

Plasma frequency false-color 3D plot.

Electron density modulation (self-mixing envelope) false-color 3D plot (Fig 5.18).

```

hold on;
h11=plot(Y(:,17), [n(:,91), n2(:,91)], 'g');
h11=plot(Y(:,17), [n(:,81), n2(:,81)], 'r');
h11=plot(Y(:,17), [n(:,71), n2(:,71)], 'c');
h11=plot(Y(:,17), [n(:,61), n2(:,61)], 'm');
h11=plot(Y(:,17), [n(:,51), n2(:,51)], 'k');
h11=plot(Y(:,17), [n(:,41), n2(:,41)], 'b');
h11=plot(Y(:,17), [n(:,31), n2(:,31)], 'g');
% h11=plot(Y(:,17), [n(:,21), n2(:,21)], 'r');
% h11=plot(Y(:,17), [n(:,11), n2(:,11)], 'c');
% h11=plot(Y(:,17), [n(:,1), n2(:,1)], 'm');
legend('0.5 V', 'approx. for 0.5 V', '0.4 V', 'approx. for 0.4 V', '0.3 V', 'approx. for 0.3 V', '0.2 V', 'approx. for 0.2 V', '0.1 V', 'approx. for 0.1 V', '0 V', 'approx. for 0 V', '-0.1 V', 'approx. for -0.1 V', '-0.2 V', 'approx. for -0.2 V');
xlabel('Y (nm)');
ylabel('electron density (cm^{-3})');
axis ([0 200 0 7e16]);

```

*Electron density plot
(Fig 1.8).*

```

figure;
h13=surfc(VG,Y,real(v1000));
colorbar;
colormap jet;
shading interp;
view(2);
axis ([-0.5 0.3 0 200]);
xlabel('V_{G} (Volt)');
ylabel('Y (nm)');
zlabel('electron mobility (m^2/Vs)');
title('electron mobility for 1 THz (m^2/Vs)');

```

*Electron mobility false-color 3D plot for 1 THz
(Fig. 5.19 and eq.(5.1.5.8)).*

```

figure;
h14=surfc(VG,Y,real(v600));
colorbar;
colormap jet;
shading interp;
xlabel('V_{G} (Volt)');
ylabel('Y (nm)');
zlabel('electron mobility (m^2/Vs)');
title('electron mobility for 0.6 THz (m^2/Vs)');

```

*Electron mobility,
0.6 THz.*

```

figure;
h15=surfc(VG,Y,real(v240));
colorbar;
colormap jet;
shading interp;
xlabel('V_{G} (Volt)');
ylabel('Y (nm)');
zlabel('electron mobility (m^2/Vs)');
title('electron mobility for 0.24 THz (m^2/Vs)');

```

*Electron mobility,
0.24 THz.*

```

figure;
h16=surfc(VG,Y,real(v140));
colorbar;
colormap jet;
shading interp;
xlabel('V_{G} (Volt)');
ylabel('Y (nm)');
zlabel('electron mobility (m^2/Vs)');
title('electron mobility for for 0.14 THz');

```

*Electron mobility,
0.14 THz.*

```

figure;
h17=plot(VG(1,:),v1000(105,:), 'o-b');
hold on;
h17=plot(VG(1,:),v600(105,:), 'o-g');
h17=plot(VG(1,:),v240(105,:), 'o-r');
h17=plot(VG(1,:),v140(105,:), 'o-k');
xlabel('V_{G} (Volt)');
ylabel('electron mobility at the channel center (m^2/Vs)');
axis([-0.6 0.6 -0.1 1.1]);

```

```
legend('1 THz','600 GHz','240 GHz','140 GHz');
```

```
figure;
h18=surf(VG,Y,signal1000);
colorbar;
colormap jet;
shading interp;
view(2);
axis ([-0.5 0.5 0 200]);
xlabel('V_{G} (Volt)');
ylabel('Y (nm)');
zlabel('signal (A/Wm^2)');
title('Rectified current density for 1 THz (100% power coupling efficiency
assumed)');
```

*Rectified current density
false-color 3D plot for 1 THz
(Fig. 5.20 and eq.(5.1.5.9)).*

```
figure;
h19=surfc(VG,Y,signal600);
colorbar;
colormap jet;
shading interp;
view(2);
axis ([-0.5 0.5 0 200]);
xlabel('V_{G} (Volt)');
ylabel('Y (nm)');
zlabel('signal (A/Wm^2)');
title('Rectified current density for 0.6 THz (100% power coupling efficiency
assumed)');
```

*Rectified current density,
0.6 THz.*

```
figure;
h20=surfc(VG,Y,signal240);
colorbar;
colormap jet;
shading interp;
view(2);
axis ([-0.5 0.5 0 200]);
xlabel('V_{G} (Volt)');
ylabel('Y (nm)');
zlabel('signal (A/Wm^2)');
title('Rectified current density for 0.24 THz (100% power coupling efficiency
assumed)');
```

*Rectified current density,
0.24 THz.*

```
figure;
h21=surfc(VG,Y,signal140);
colorbar;
colormap jet;
shading interp;
view(2);
axis ([-0.5 0.5 0 200]);
xlabel('V_{G} (Volt)');
ylabel('Y (nm)');
zlabel('signal (A/Wm^2)');
title('Rectified current density for 0.14 THz (100% power coupling efficiency
assumed)');
```

*Rectified current density,
0.14 THz.*

```
figure;
h22=plot(VG(1,:),IntegSig1000,'o-b');
hold on;
h22=plot(VG(1,:),IntegSig600,'o-g');
h22=plot(VG(1,:),IntegSig240,'o-r');
h22=plot(VG(1,:),IntegSig140,'o-k');
xlabel('V_{G} (Volt)');
ylabel('Signal (A/W)');
title('Rectified Current (A/W) (100% power coupling efficiency assumed)');
%axis([-0.65 0.65 0 3e17]);
legend('1 THz','600 GHz','240 GHz','140 GHz');
```

*Responsivity plot
(Fig. 5.21 and eq.(5.1.5.10)).*

Appendix G HFSS

HFSS is a finite element method 3D electromagnetic simulation software by Ansoft corporation. HFSS is also an abbreviation for high frequency structure simulator. There are three different ways to solve the Maxwell's equations for an electromagnetic structure: finite element method (FEM), finite difference time doimain (FDTD), and method of moments (MoM).

Method	FEM	FDTD	MoM
Equations to solve	Partial differential equations	Partial differential equations	Integral equations
Grid method	Adaptively refines 3D tetrahedral spatial grid, size varies.	Rectangular 3D spatial grid, same size	2D grids on boundary surfaces
Required memory scaling with N	$O(N^2)$	$O(N)$	$O(N^2)$
Good for		Highly inhomogeneous structures (e.g., photonic crystals)	Planar structures, small surface / volume ratio
Not good for	Highly inhomogeneous structures		Structures with a large surface / volume ratio

Figure G.1 Review of three different methods for electromagnetic simulations. N = number of grid elements.

See Section 7.1 of Ref. [64], Section 1.4 of Ref. [65], or elsewhere, for the pros and cons of the different methods. Fig. G.1 is my attempt to summarize them.

G.a Example: 240 GHz EPR Cavity

A 240 GHz microwave cavity for an electron paramagnetic resonance (EPR) experiment was simulated with HFSS. The first task is to draw an electromagnetic structure with the CAD tools. Fig. G.2 shows the popup windows which set a Gaussian input beam.

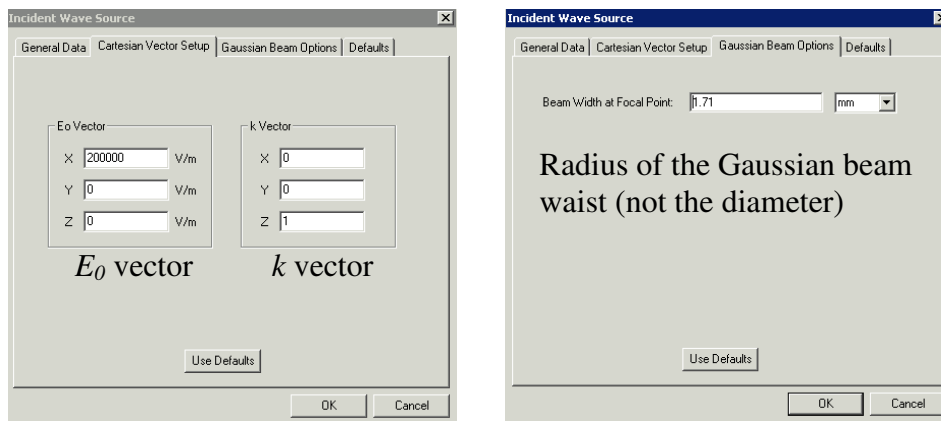


Figure G.2 Setting a Gaussian input beam.

When the simulation is run, an initial tetrahedral mesh (or grid) is randomly seeded (created). PDE is solved at each tetrahedron, and the energy contained in each tetrahedron is calculated. As the simulation iterates, the mesh is refined, and the energies from the latest two passes (or iterations) are compared. The mesh is

refined until the energy difference “Delta Magnitude Energy” is less than a specified quantity, or when the maximum number of iteration is reached. Fig. G.3 shows the mesh grid after 8 iterations. The grid is opaque, so only the outermost grid lines are shown.

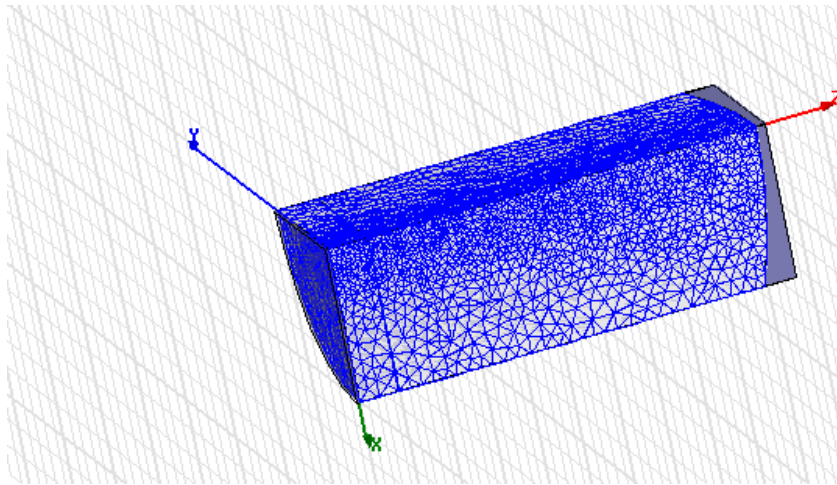


Figure G.3 Automatically generated mesh grid.

Due to the cylindrical symmetry of the cavity, a quarter of the cavity was simulated with the x - z and y - z planes set as symmetry planes. See Fig. G.4 for the user interface when the simulation is being run. Fig. G.5 shows a popup window for monitoring the solution data. On the “convergence” tab, the maximum (among the values from all the tetrahedra) of the “Delta Magnitude Energy” for each pass can be seen. The solution data *may* be trusted if “Max Delta Mag Energy” is converged to a value smaller than 0.05. If converged to a value larger than 0.05, or not converged, use or disposal of the solution is up to user’s discretion.

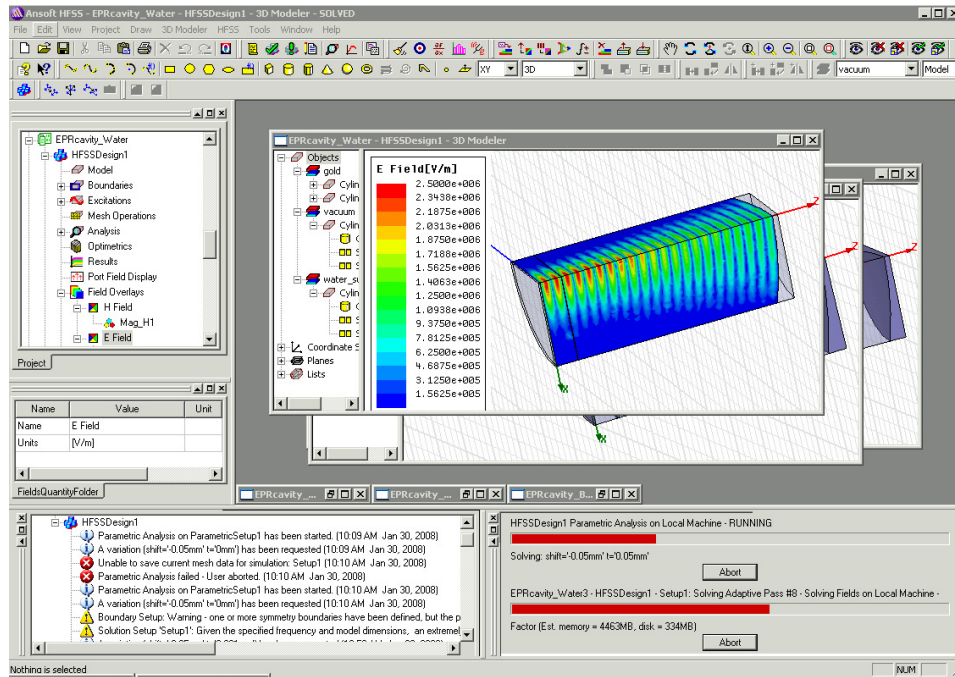


Figure G.4 User interface of HFSS.

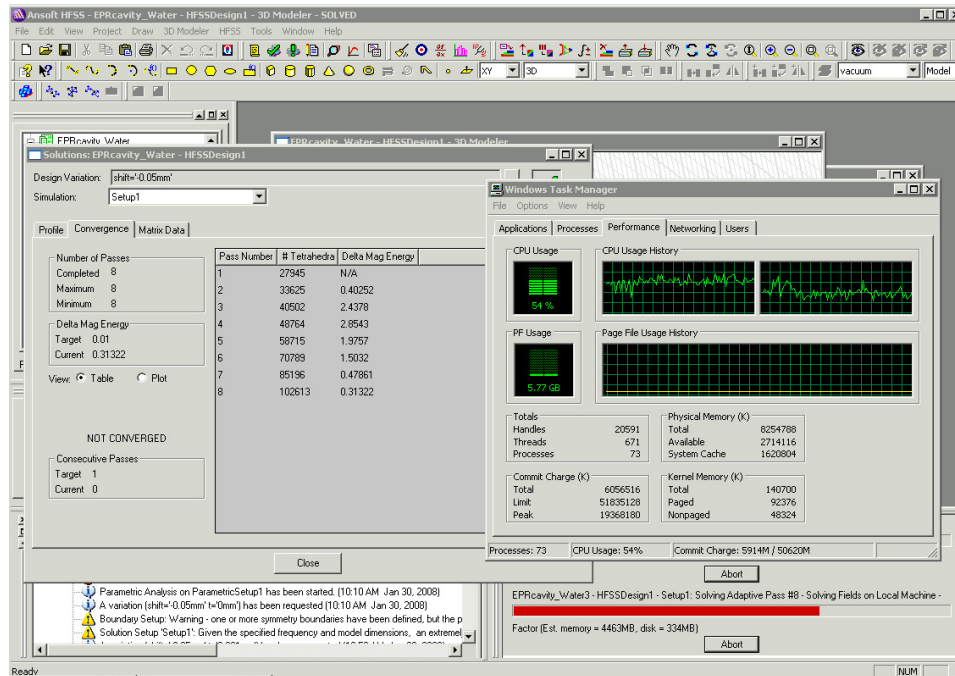


Figure G.5 Convergence of the solution gives credibility.

Although the Gaussian beam excitation in Fig. G.2 was easier to understand, it was difficult to track the effect of the various tuning (cavity length tuning, etc). “Waveport” excitation mode provides S-parameters for easy monitoring of the tuning effect (see Fig. G.6), and therefore, were used for the following study.

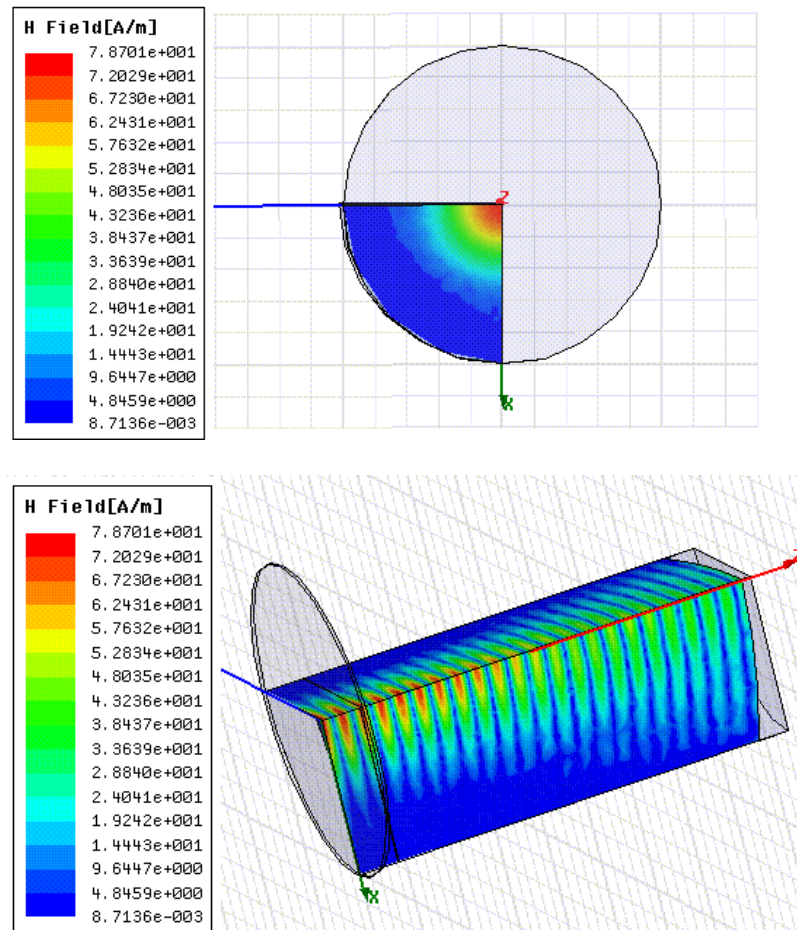


Figure G.6 “Waveport” excitation is used to calculate S-parameter.

Fig. G.7 shows the magnitude of the returning wave as the cavity length is detuned. The maximum point corresponds to the best cavity length for the resonance.

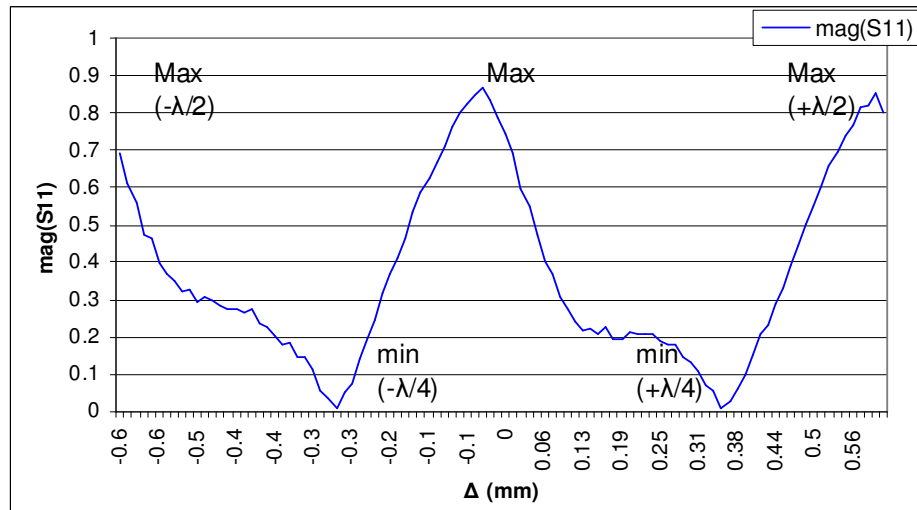


Figure G.7 Scanning cavity length detuning Δ .

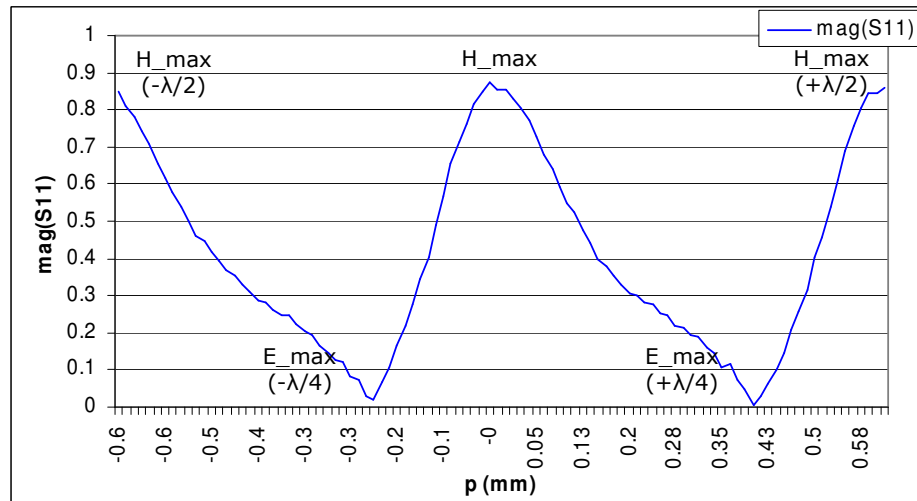


Figure G.8 Scanning water layer position p .

In an EPR experiment, an aqueous solution sample layer will be placed at the H-field maximum. Fig. G.8 shows the simulation results with the position of the water layer scanned. As desired, the water absorption is minimal with the water layer placed at the H-field maximum.

Finally, the ideal sample should be as thick as possible, so that largest EPR signal can be obtained. In Fig. G.9, the water thickness is increased. The field inside the cavity did not decrease significantly until the thickness of 40 ~ 60 μm .

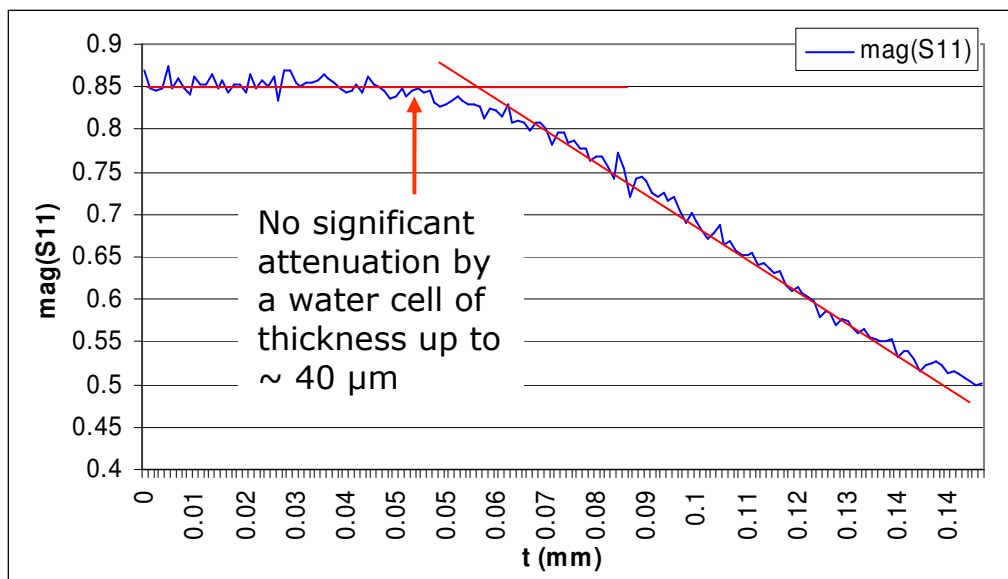


Figure G.9 Scanning water layer thickness t . Water layer thickness up to 40 μm is okay.

Through this simulation study, cavity length, sample position and thickness for 240 GHz EPR experiments were obtained.

BIBLIOGRAPHY

1. SURA. *Chart of the Electromagnetic Spectrum*. Available from: <http://www.sura.org>.
2. Liu, H.B., et al., *Detection and identification of explosive RDX by THz diffuse reflection spectroscopy*. Optics Express, 2006. **14**(1): p. 415-423.
3. Murrill, S.R., et al., *Terahertz imaging system performance model for concealed-weapon identification*. Applied Optics, 2008. **47**(9): p. 1286-1297.
4. Madaras, E.I., et al., *APPLICATION OF TERAHERTZ RADIATION TO THE DETECTION OF CORROSION UNDER THE SHUTTLE'S THERMAL PROTECTION SYSTEM*. AIP Conference Proceedings, 2008. **975**: p. 421-428.
5. ESA. *Plank Satellite*. 2009; Available from: http://www.esa.int/esaSC/SEM9WJ0XDYD_0_spk.html.
6. Rothman, L.S., et al., *The HITRAN 2008 molecular spectroscopic database*. Journal of Quantitative Spectroscopy & Radiative Transfer, 2009. **110**(9-10): p. 533-572.
7. Xu, J., K.W. Plaxco, and S.J. Allen, *Probing the collective vibrational dynamics of a protein in liquid water by terahertz absorption spectroscopy*. Protein Science, 2006. **15**(5): p. 1175-1181.
8. Markelz, A.G., et al., *Protein dynamical transition in terahertz dielectric response*. Chemical Physics Letters, 2007. **442**(4-6): p. 413-417.
9. Siegel, P.H., *Terahertz technology*. Ieee Transactions on Microwave Theory and Techniques, 2002. **50**(3): p. 910-928.
10. Takahashi, S., et al., *Pulsed EPR spectrometer with injection-locked UCSB free-electron laser*. Infrared Physics & Technology, 2008. **51**(5): p. 426-428.
11. Siegel, P.H., *Terahertz technology in biology and medicine*. Ieee Transactions on Microwave Theory and Techniques, 2004. **52**(10): p. 2438-2447.
12. Taylor, Z.D., et al., *Reflective terahertz imaging of porcine skin burns*. Optics Letters, 2008. **33**(11): p. 1258-1260.
13. Taday, P.F., *Applications of terahertz spectroscopy to pharmaceutical sciences*. Philosophical Transactions of the Royal Society of London Series a-Mathematical Physical and Engineering Sciences, 2004. **362**(1815): p. 351-363.

14. Banerjee, D., et al., *Diagnosing water content in paper by terahertz radiation*. Optics Express, 2008. **16**(12): p. 9060-9066.
15. Intel. *i7-975 processor has clock speed of 3.33 GHz*. Available from: <http://www.intel.com/Consumer/Learn/Desktop/corei7-extreme-detail.htm#proc-num>.
16. Rodwell, M., et al., *High speed InP-based heterojunction bipolar transistors*. Compound Semiconductors 2001, 2002(170): p. 21-26.
17. M. S. Sherwin, C.C., B. Serapiglia, Y. Dora, J. B. Williams, K. Maranowski, A. C. Gossard, W. R. McGrath. *Tunable Antenna-coupled Intersubband Terahertz (TACIT) Mixers: The Quantum Limit Without the Quantum Liquid*. in *Far-IR Sub-mm and mm Detector Technology Workshop*. 2002. Monterey, CA.
18. Cates, C.L., et al., *A concept for a tunable antenna-coupled intersubband terahertz (TACIT) detector*. Physica E, 1998. **2**(1-4): p. 463-467.
19. Serapiglia, G.B., et al. *Ultrafast tunable antenna-coupled quantum-well THz detectors operating above 100K*. in *Infrared and Millimeter Waves and 13th International Conference on Terahertz Electronics, 2005. IRMMW-THz 2005. The Joint 30th International Conference on*. 2005.
20. Schneider, H. and H.C. Liu, *Quantum well infrared photodetectors physics and applications*. 2007, Springer: Berlin ; New York. p. xvi, 248 p.
21. Woolard, D.L., W.R. Loerop, and M. Shur, *Terahertz sensing technology*. Selected topics in electronics and systems v. 30. 2003, River Edge, NJ: World Scientific Pub.
22. Crowe, J.L.H.a.T.W. *Responsivity and Noise Measurements of Zero-Bias Schottky Diode Detectors*. in *18th International Symposium Space Terahertz Technology*. 2007. Pasadena, CA.
23. Tauk, R., et al., *Plasma wave detection of terahertz radiation by silicon field effects transistors: Responsivity and noise equivalent power*. Applied Physics Letters, 2006. **89**(25): p. 253511-1.
24. Krekels, H.G., B. Schiek, and E. Menzel. *Power Detector with GaAs Field Effect Transistors*. in *European Microwave Conference, 1992. 22nd*. 1992.
25. Pfeiffer, U. *A CMOS Focal-Plane Array for Terahertz Imaging*. in *33rd International Conference on Infrared, Millimeter, and Terahertz Waves*. 2008. Caltech, Pasadena, CA.
26. Lisauskas, A., et al., *Rational design of high-responsivity detectors of terahertz radiation based on distributed self-mixing in silicon field-effect transistors*. Journal of Applied Physics, 2009. **105**(11): p. 114511.

27. Lisauskas, A., et al., *Terahertz imaging with GaAs field-effect transistors*. Electronics Letters, 2008. **44**(6): p. 408-409.
28. Dooley, D. *Measuring THz Radiation...choose a Pyroelectric Detector or Golay Cell?* Application Note 1011 Rev. A **5/25/09**; Available from: <http://www.spectrumdetector.com/pdf/applicationNotes/1011.pdf>.
29. Ganichev, S.D., et al., *Subnanosecond ellipticity detector for laser radiation*. Applied Physics Letters, 2007. **91**(9): p. 091101-1.
30. Kim, S., et al., *Room temperature terahertz detection based on bulk plasmons in antenna-coupled GaAs field effect transistors*. Applied Physics Letters, 2008. **92**(25): p. 253508-1.
31. Karasik, B.S. and A.I. Elantiev, *Noise temperature limit of a superconducting hot-electron bolometer mixer*. Applied Physics Letters, 1996. **68**(6): p. 853-855.
32. Kohn, W., *Cyclotron Resonance and De Haas-Van Alphen Oscillations of an Interacting Electron Gas*. Physical Review, 1961. **123**(4): p. 1242-&.
33. Halperin, B.I., *Possible States for a Three-Dimensional Electron Gas in a Strong Magnetic Field*. Japanese Journal of Applied Physics, 1987. **26**(Supplement 26-3-3): p. 1913-1919.
34. Karrai, K., et al., *Magnetoplasma Effects in a Quasi-3-Dimensional Electron-Gas*. Physical Review B, 1989. **39**(2): p. 1426-1429.
35. Brey, L., N.F. Johnson, and B.I. Halperin, *Optical and Magneto-Optical Absorption in Parabolic Quantum Wells*. Physical Review B, 1989. **40**(15): p. 10647-10649.
36. Karrai, K., et al., *Collective Cyclotron-Resonance in a Quasi-3-Dimensional Electron-Gas*. Physical Review B, 1989. **40**(17): p. 12020-12023.
37. Wixforth, A., et al., *Dimensional Resonances in Wide Parabolic Quantum-Wells*. Physical Review B, 1991. **43**(12): p. 10000-10003.
38. Dempsey, J. and B.I. Halperin, *Tilted-Field Magneto-optical Absorption in an Imperfect Parabolic Quantum-Well*. Physical Review B, 1992. **45**(7): p. 3902-3905.
39. Jackson, J.D., *Classical electrodynamics*. 3rd ed. 1999, New York: Wiley. xxi, 808 p.
40. Yuh, E.L., et al., *Effects of nonlocal response and level quantization on electronic excitations of a bimetallic jellium film in an Al_xGa_{1-x}As heterostructure*. Physical Review B, 1996. **54**(16): p. 11467-11478.

41. BYU. *Metal-Semiconductor Junction Depletion Layer Width Calculator*. Available from: <http://www.ee.byu.edu/cleanroom/ohmic-schottky.phtml>.
42. Seeger, K., *Semiconductor physics : an introduction*. 9th ed ed. Advanced texts in physics, 2004, Berlin ; New York: Springer. x, 537 p.
43. Focardi, P., W.R. McGrath, and A. Neto, *Design guidelines for terahertz mixers and detectors*. Ieee Transactions on Microwave Theory and Techniques, 2005. **53**(5): p. 1653-1661.
44. Gatesman, A.J., et al., *An anti-reflection coating for silicon optics at terahertz frequencies*. Ieee Microwave and Guided Wave Letters, 2000. **10**(7): p. 264-266.
45. Pozar, D.M., *Microwave engineering*. 3rd ed ed. 2005, Hoboken, NJ: J. Wiley. xvii, 700 p.
46. EPOTEK. *Technical Data Sheet of EPO-TEK 353ND epoxy resin and hardner*. Available from: www.epotek.com/SSCDocs/datasheets/353ND.PDF.
47. Stillman, G.E., C.M. Wolfe, and J.O. Dimmock, *Hall Coefficient Factor for Polar Mode Scattering in N-Type GaAs*. Journal of Physics and Chemistry of Solids, 1970. **31**(6): p. 1199-&.
48. Blakemore, J.S., *Semiconducting and Other Major Properties of Gallium-Arsenide*. Journal of Applied Physics, 1982. **53**(10): p. R123-R181.
49. Sze, S.M., *Physics of semiconductor devices*. 2nd ed ed. 1981, New York: Wiley. xii, 868 p.
50. Richards, P.L., *Bolometers for Infrared and Millimeter Waves*. Journal of Applied Physics, 1994. **76**(1): p. 1-24.
51. Mather, J.C., *Bolometer Noise - Non-Equilibrium Theory*. Applied Optics, 1982. **21**(6): p. 1125-1129.
52. Weckwerth, M.V., et al., *Epoxy bond and stop-etch (EBASE) technique enabling backside processing of (Al)GaAs heterostructures*. Superlattices and Microstructures, 1996. **20**(4): p. 561-567.
53. Shin, J., *Substrate Removed Gallium Arsenide/Aluminium Gallium Arsenide Optical Modulators*, in *Materials*, University of California: Santa Barbara.
54. Van Rudd, J. and D.M. Mittleman, *Influence of substrate-lens design in terahertz time-domain spectroscopy*. Journal of the Optical Society of America B-Optical Physics, 2002. **19**(2): p. 319-329.
55. Yariv, A., *Optical electronics in modern communications*. 5th ed. 1997, New York ; Oxford, [England]: Oxford University Press. xviii, 744 p.

56. Doty, M.F., et al., *Verification of polarization selection rules and implementation of selective coherent manipulations of hydrogenic transitions in n-GaAs*. Physical Review B, 2005. **71**(20): p. 201201.
57. Dyakonov, M.I. and M.S. Shur, *Plasma wave electronics: Novel terahertz devices using two dimensional electron fluid*. Ieee Transactions on Electron Devices, 1996. **43**(10): p. 1640-1645.
58. Knap, W., et al., *Plasma wave detection of sub-terahertz and terahertz radiation by silicon field-effect transistors*. Applied Physics Letters, 2004. **85**(4): p. 675-677.
59. NEC. *NE722S01 ADS model*. Available from: http://www.necel.com/microwave/en/parameter/low_gaashj_dp.html#designer.
60. Dobrzanski, L. and Z. Wolosiak, *On the origin of low frequency noise in GaAs metal-semiconductor field-effect transistors*. Journal of Applied Physics, 2000. **87**(1): p. 517-521.
61. Lee, J.L., Y.T. Kim, and J.Y. Lee, *Microstructural evidence on direct contact of Au/Ge/Ni/Au ohmic metals to InGaAs channel in pseudomorphic high electron mobility transistor with undoped cap layer*. Applied Physics Letters, 1998. **73**(12): p. 1670-1672.
62. Iliadis, A., *Barrier Height Reduction in Au-Ge Schottky Contacts to N-Type Gaas*. Journal of Vacuum Science & Technology B, 1987. **5**(5): p. 1340-1345.
63. Snider, G. *1D Poisson*. Available from: <http://www.nd.edu/~gsnider/>.
64. CRCnetBASE (Online service) and L.C. Godara, *Handbook of antennas in wireless communications*. 2002, CRC Press: Boca Raton, Fla. p. 1 v. (various pagings).
65. Taflove, A. and S.C. Hagness, *Computational electrodynamics : the finite-difference time-domain method*. 3rd ed. 2005, Boston: Artech House. xxii, 1006 p.